

## Polarimeter to Unify the Corona and Heliosphere (PUNCH)

Craig E. DeForest<sup>1</sup> · Sarah E. Gibson<sup>2</sup> ·  
Ronnie Killough<sup>1</sup> · Nick R. Waltham<sup>3</sup> ·  
Matt N. Beasley<sup>1</sup> · Robin C. Colaninno<sup>4</sup> ·  
Glenn T. Laurent<sup>1</sup> · Daniel B. Seaton<sup>1</sup> ·  
J. Marcus Hughes<sup>1</sup> · Madhulika  
Guhathakurta<sup>5</sup> · Nicholeen M. Viall<sup>6</sup> ·  
Raphael Attié<sup>7</sup> · Dipankar Banerjee<sup>8</sup> ·  
Luke Barnard<sup>9</sup> · Doug A. Biesecker<sup>10</sup> ·  
Mario M. Bisi<sup>3</sup> · Volker Bothmer<sup>11</sup> ·  
Antonina Brody<sup>1</sup> · Joan Burkepile<sup>2</sup> ·  
Iver H. Cairns<sup>12</sup> · Jennifer L. Campbell<sup>1</sup> ·  
Traci R. Case<sup>1</sup> · Amir Caspi<sup>1</sup> · David  
Cheney<sup>5</sup> · Rohit Chhiber<sup>13</sup> · Matthew J.  
Clapp<sup>3</sup> · Steven R. Cranmer<sup>14</sup> · Jackie A.  
Davies<sup>3</sup> · Curt A. de Koning<sup>15</sup> · Mihir I.  
Desai<sup>1</sup> · Heather A. Elliott<sup>1</sup> · Samaiyah  
Farid<sup>2</sup> · Bea Gallardo-Lacourt<sup>16</sup> · Chris  
Gilly<sup>1</sup> · Caden Gobat<sup>1</sup> · Mary H.  
Hanson<sup>14</sup> · Richard A. Harrison<sup>3</sup> ·  
Donald M. Hassler<sup>1</sup> · Chase Henley<sup>1</sup> ·  
Alan M. Henry<sup>1</sup> · Russell A. Howard<sup>17</sup> ·  
Bernard V. Jackson<sup>18</sup> · Samuel Jones<sup>19</sup> ·  
Don Kolinski<sup>2</sup> · Derek A. Lamb<sup>1</sup> · Florine  
Lehtinen<sup>1</sup> · Chris Lowder<sup>1</sup> · Anna  
Malanushenko<sup>2</sup> · William H.  
Matthaeus<sup>13</sup> · David J. McComas<sup>20</sup> ·  
Jacob McGee<sup>1</sup> · Huw Morgan<sup>21</sup> · Divya  
Oberoi<sup>22</sup> · Dusan Odstrcil<sup>7</sup> · Chris  
Parmenter<sup>3</sup> · Ritesh Patel<sup>1</sup> · Francesco  
Pecora<sup>13</sup> · Steve Persyn<sup>1</sup> · Victor J.  
Pizzo<sup>10</sup> · Simon P. Plunkett<sup>5</sup> · Elena  
Provornikova<sup>17</sup> · Nour Eddine Raouafi<sup>17</sup> ·  
Jillian A. Redfern<sup>1</sup> · Alexis P.  
Rouillard<sup>23</sup> · Kelly D. Smith<sup>1</sup> · Keith B.  
Smith<sup>1</sup> · Zachary S. Talpas<sup>1</sup> · S. James  
Tappin<sup>3</sup> · Arnaud Thernisien<sup>4</sup> ·  
Barbara J. Thompson<sup>6</sup> · Samuel  
Van Kooten<sup>1</sup> · Kevin J. Walsh<sup>1</sup> ·  
David F. Webb<sup>24</sup> · William L. Wells<sup>1</sup> ·

---

Matthew J. West<sup>25</sup>  · Zachary Wiens<sup>1</sup> · Yan  
Yang<sup>13</sup> · Andrei Zhukov<sup>26</sup> 

© The author(s) ••••

---

✉ C.E. DeForest  
[deforest@boulder.swri.edu](mailto:deforest@boulder.swri.edu)

S.E. Gibson  
[sgibson@ucar.edu](mailto:sgibson@ucar.edu)

R.L. Killough  
[rkillough@swri.org](mailto:rkillough@swri.org)

<sup>1</sup> Southwest Research Institute, 1050 Walnut Street Suite 300, Boulder, CO 80302 U.S.A.

<sup>2</sup> National Center for Atmospheric Research / High Altitude Observatory, Boulder, CO, U.S.A.

<sup>3</sup> United Kingdom Research & Innovation / Science & Technology Facilities Council / Rutherford Appleton Laboratory, Harwell Campus, Oxfordshire, U.K.

<sup>4</sup> Naval Research Laboratory, Washington, DC, U.S.A.

<sup>5</sup> NASA Headquarters, Washington, DC, U.S.A.

<sup>6</sup> NASA Goddard Space Flight Center, Greenbelt, MD, U.S.A.

<sup>7</sup> George Mason University, Innovation Park, VA, U.S.A.

<sup>8</sup> Indian Institute of Astrophysics, Bangalore, India

<sup>9</sup> University of Reading, Reading, U.K.

<sup>10</sup> NOAA Space Weather Prediction Center, Boulder, CO, U.S.A.

<sup>11</sup> University of Göttingen, Germany

<sup>12</sup> University of Sydney, Australia

<sup>13</sup> University of Delaware, Newark, DE, U.S.A.

<sup>14</sup> University of Colorado, Boulder, CO, U.S.A.

<sup>15</sup> Cooperative Institute for Research in Environmental Sciences, Boulder, CO, U.S.A.

<sup>16</sup> Catholic University of America, Washington, DC, U.S.A.

<sup>17</sup> Johns Hopkins University Applied Physics Laboratory, Columbia, MD, U.S.A.

<sup>18</sup> University of California, San Diego, CA, U.S.A.

<sup>19</sup> Stellar Solutions Inc., Los Altos, CA, U.S.A.

<sup>20</sup> Princeton University, Princeton, NJ, U.S.A.

<sup>21</sup> University of Aberystwyth, U.K.

## Abstract

The Polarimeter to Unify the Corona and Heliosphere (PUNCH) mission is a NASA Small Explorer to determine the cross-scale processes that unify the solar corona and heliosphere. PUNCH has two science objectives: (1) understand how coronal structures become the ambient solar wind, and (2) understand the dynamic evolution of transient structures, such as coronal mass ejections, in the young solar wind. To address these objectives, PUNCH uses a constellation of four small spacecraft in Sun-synchronous low Earth orbit, to collect linearly polarized images of the K corona and young solar wind. The four spacecraft each carry one visible-light imager in a 1+3 configuration: a single Narrow Field Imager solar coronagraph captures images of the outer corona at all position angles, and at solar elongations from  $1.5^\circ$  ( $6 R_\odot$ ) to  $8^\circ$  ( $32 R_\odot$ ); and three separate Wide Field Imager heliospheric imagers together capture views of the entire inner solar system, at solar elongations from  $3^\circ$  ( $12 R_\odot$ ) to  $45^\circ$  ( $180 R_\odot$ ) from the Sun. PUNCH images include linear-polarization data, to enable inferring the three-dimensional structure of visible features without stereoscopy. The instruments are matched in wavelength passband, support overlapping instantaneous fields of view, and are operated synchronously, to act as a single “virtual instrument” with a  $90^\circ$  wide field of view, centered on the Sun. PUNCH launched in March of 2025 and began science operations in June of 2025. PUNCH has an open data policy with no proprietary period, and PUNCH Science Team Meetings are open to all.

**Keywords:** Comets; Corona; Coronal Mass Ejections; Instrumentation and Data Management; Polarization; Solar Wind; Turbulence; Velocity Fields

*Look deep into nature, and then you will understand everything better. – A. Einstein*

---

<sup>22</sup> National Center for Radio Astrophysics, India

<sup>23</sup> Institut de Recherche en Astrophysique et Planétologie, Toulouse, France

<sup>24</sup> Boston College, Boston, MA, U.S.A.

<sup>25</sup> European Space Agency, Noordwijk, Netherlands

<sup>26</sup> Royal Observatory of Belgium, Brussels, Belgium

## 1. Introduction

The Polarimeter to UNify the Corona and Heliosphere (PUNCH) mission is a NASA Small Explorer to determine the cross-scale processes that unify the solar corona and heliosphere. PUNCH has two science objectives: (1) to understand how coronal structures become the ambient solar wind, and (2) to understand the dynamic evolution of transient structures, such as coronal mass ejections, in the young solar wind.

The two PUNCH science objectives are encapsulated in three science questions each, rendered in Figure 1. They are:

1. Understand how coronal structures become the ambient solar wind.
  - a) How does the young solar wind flow and evolve on global scales?
  - b) Where and how do mesoscale structures and turbulence form in the solar wind?
  - c) What are the evolving physical properties of the Alfvén surface?
2. Understand the dynamic evolution of transient structures in the solar wind.
  - a) How do coronal mass ejections (CMEs) propagate and evolve in the solar wind, in three dimensions?
  - b) How do quasi-stationary stream interaction regions (SIRs) form and evolve?
  - c) How do shocks form and interact with the solar wind across spatial scales?

These objectives are addressed with deep-field, polarimetric image sequences of the “K corona”, consisting of sunlight that is Thomson-scattered by electrons in the coronal and solar wind plasma. Four separate Observatories, each comprising a small spacecraft and a single visible-light imager, orbit the Earth in a Sun-synchronous twilight (6am/6pm) 650 km orbit, maintain widely spaced orbital phases, and act as a single “virtual coronagraph” with a 90° field of view, to record the entire inner solar system at solar elongation angles between 1.5° and 45°.

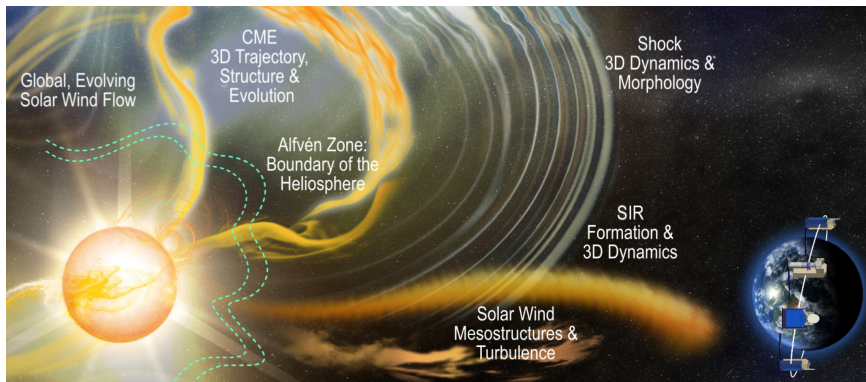


**Figure 1.** Artist's rendering shows the six major PUNCH scientific topics, each addressed by a science question. These are organized into two major science objectives (understanding the ambient and the dynamic solar wind) in support of a single science goal: to determine the cross-scale processes that unite the solar corona and heliosphere.

PUNCH exists within the context of constantly improving solar and heliospheric studies. Historically, solar physics and heliospheric physics have been separate disciplines, divided by the technologies used to study each portion of the Sun-heliosphere system. The solar corona has been studied primarily by remote sensing, for example with visible light scattered by free electrons (Thomson 1903) to form the K corona (e.g., Billings 1966) although many other remote-sensing technologies also apply. Remote sensing generally provides morphology and large scale macrophysics, with some indirect insight into unresolvable microphysics. Contrariwise, the solar wind has been studied primarily by in-situ sampling of the material in interplanetary space (Neugebauer and Snyder 1966); these technologies yield detailed diagnosis of plasma conditions at a single moving point in the plasma, with indirect insight into large-scale macrophysics.

Joint studies of the solar corona and solar wind have generally required spanning the two radically different experimental disciplines, but have borne fruit in connecting the Sun and near-Earth environments (Zirker 1977; Sheeley *et al.* 1985; Domingo, Fleck, and Poland 1995). ESA's Solar Orbiter mission (Müller *et al.* 2020) carries a hybrid instrument suite specifically designed to enable joint remote/in-situ studies of solar wind features and streams, by associating particular remotely sensed coronal features with the plasma detected in-situ by the spacecraft. Recently, the Parker Solar Probe (Fox *et al.* 2016) has carried in-situ sampling devices into the outer reaches of the solar corona itself (Kasper *et al.* 2021), allowing direct measurement of the microphysics in the outer corona with simultaneous remote sensing of the relevant large-scale structures surrounding the system under study.

Multiple instruments, including the Coriolis Solar Mass Ejection Imager (Coriolis/SMEI; Eyles *et al.* 2003), the Solar-Terrestrial Relations Observatory's Sun-Earth Connection Coronal and Heliospheric Investigation (STEREO/SECCHI; Howard *et al.* 2008), the Solar Orbiter Heliospheric Imager (SOLO/SOLOHI; Howard *et al.* 2020), and the Parker Solar Probe Wide-field Imager for Solar Probe (PSP/WISPR; Vourlidas *et al.* 2016), have been built to image large and bright features in the solar wind. With the advent of imaging from off the Sun-Earth line, via STEREO/SECCHI, direct, quantitative, simultaneous imaging and in-situ studies of Earth-bound events became possible (e.g., Davies *et al.* 2009; DeForest, Howard, and McComas 2013), and the presence of multiple deep-space missions with intersecting fields of view and on-board in-situ instruments has greatly increased the number of such studies. PUNCH brings routine global imaging of the solar wind and its structures into the mix of available observations, explicitly enabling a unified treatment of the corona and solar wind as a single system.

PUNCH polarimetry is designed to allow location of features in three dimensions (3D) from a single vantage point: both mesoscale solar wind structure (e.g., Viall, DeForest, and Kepko 2021) and coronal mass ejections (de Koning, Pizzo, and Biesecker 2009; Mierla *et al.* 2009; DeForest, de Koning, and Elliott 2017). This is possible because the K corona consists of sunlight that is Thomson scattered by free electrons. Thomson scattering polarizes the outbound beam according to the scattering angle (Billings 1966; Tappin and Howard 2009; DeForest, Howard, and Tappin 2013). Each coronal feature is therefore polarized

to a degree that depends on its three-dimensional location. The basic theory has been known for decades, but was only reduced to practice once image quality and analysis methods improved enough to reveal the polarimetric signal with sufficient fidelity (Mierla *et al.* 2010; DeForest, de Koning, and Elliott 2017). Many authors have more recently developed the theory and demonstrated the practice, as reviewed by Gibson *et al.* (2025). PUNCH is specifically designed to measure the 3D trajectory and structure of small ejecta, CMEs, and large solar-wind features such as stream interaction regions (SIRs).

PUNCH launched into space at 2025 March 12 03:10 UTC (2025 March 11 20:10 PDT) from Vandenberg Space Force Base. The four  $\sim 50$  kg smallsat Observatories deployed jointly into Sun-synchronous low Earth orbit above the day/night terminator line. The Observatories dispersed over 120 days into a “1+3” constellation comprising a single NFI Observatory and, separately, the three WFIIs mutually separated by  $120^\circ$  in orbital anomaly<sup>1</sup>. A single Observatory (designated “PUNCH-NFI00” or “NFI-0”) has a “Narrow Field Imager” (NFI, or PUNCH/NFI) coronagraph (Colaninno *et al.* 2025) that images the K corona at all position angles  $\alpha$ , at elongations  $\varepsilon$  from  $1.5^\circ$  ( $6 R_\odot$ )<sup>2</sup> to  $8^\circ$  ( $32 R_\odot$ ) from the Sun. The remaining three Observatories (designated “PUNCH-WFI01” etc. or “WFI-1” etc.) each have a single “Wide Field Imager” (PUNCH/WFI) heliospheric imager (Laurent *et al.* 2025) with an approximately  $40^\circ$  square field of view, to image a portion of the sky with  $\varepsilon$  ranging from  $3^\circ$  to  $45^\circ$  ( $12 R_\odot$  to  $180 R_\odot$ ). Three WFIIs are needed to ensure sufficient coverage of the outer field of view. The instruments are operated synchronously and have matched passbands, to form a single “virtual instrument” that can produce one full polarimetric image sequence each 4 minutes, throughout the 2-year nominal mission. Figure 2 shows how the individual instrument FOVs fit together to form the overall PUNCH FOV. Every imager’s FOV overlaps with the FOV of each of the other three, to ensure cross-calibration and seamless merging of the final data. Photometric sensitivity varies across the FOV but is finer than 1% of the expected Thomson scattering brightness from CME fronts, out to  $45^\circ$  from the Sun.

An additional instrument, the Student Thermal Energetic Activity Monitor (STEAM; Hanson 2025), rides on PUNCH-NFI00 and was designed to report the time-dependent soft X-ray spectrum of the Sun, to probe the physics of coronal heating and solar flares. STEAM is physically on board PUNCH-NFI00, but is disabled due to an anomaly discovered during Observatory integration and testing, in late 2024.

The following sections are overviews of: the science motivation for PUNCH (Section 2), observing requirements that are driven by the science (Section 3),

<sup>1</sup>Readers are reminded that orbital “anomaly” is an angular parameter that indicates the position of a body in a Keplerian orbit. Variants are “true anomaly”, measured relative to the prime focus of the orbital ellipse; “eccentric anomaly”, measured relative to the center of the orbital ellipse; and “mean anomaly”, a temporal phase angle relative to the orbital period. For a circular orbit such the PUNCH nominal orbit, all three variants have the same value.

<sup>2</sup>PUNCH uses “ $R_\odot$ ” to denote exactly  $0.25^\circ$  on the celestial sphere. In project documents, “ $r_\odot$ ” refers to the solar radius of  $6.96 \times 10^8$  m.

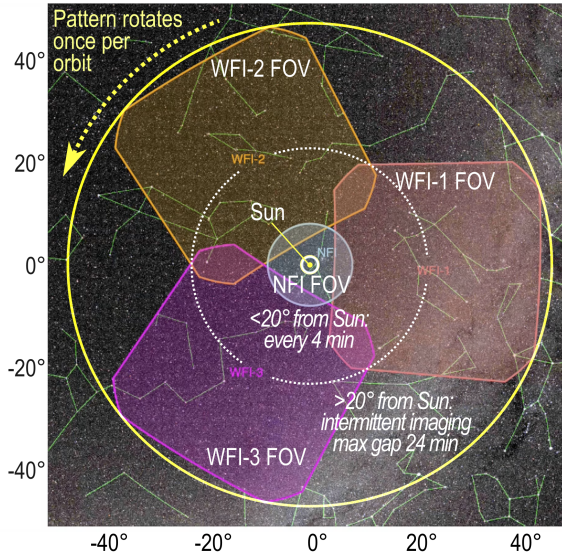


**Figure 2.** Four PUNCH spacecraft view a  $90^\circ$  wide field of view on the celestial sphere, centered on the Sun. One Narrow Field Imager (NFI) captures the outer solar corona to an elongation of  $32 R_\odot$ . Three Wide Field Imagers (WFIs) together capture a trefoil instantaneous field of view (IFOV) on the sky. The trefoil figure rotates once per orbit, capturing the complete field of view (FOV; yellow circle) approximately once every 30 minutes. The fields of view overlap at elongations below  $80 R_\odot$ , providing 4 minute cadence in the inner part of the FOV.

the PUNCH overall mission design (Section 4), the instruments (Section 5), the primary science data products (Section 6), and the expected impact of PUNCH on topics outside the primary science (Section 7), followed by a brief conclusion (Section 8). Details of each major topic are further expanded in relevant articles in this Topical Collection, cited in each section. Appendix A contains a suggested nomenclature, adopted throughout the PUNCH project, for the various angles and quantities needed for PUNCH data analysis. Appendix B provides the basic theory of 3-D imaging via polarization.

## 2. PUNCH Science

Bridging the measurement gap between solar physics and heliospheric physics is critical to understanding the Sun and heliosphere as a single system, and to understanding the origin and nature of Earth-impacting structures in the solar wind. These structures range from small-scale inhomogeneities in the solar corona and solar wind to large-scale features such as coronal mass ejections (CMEs), stream interaction regions (SIRs)<sup>3</sup>, and associated interplanetary

<sup>3</sup>We use ‘stream interaction region’ (SIR) rather than “corotating interaction region” (CIR), because SIR is the more general term. CIRs are a subset of SIRs that persist for at least a solar rotation (Pizzo 1978).

shocks. Although these features’ ultimate source is the solar corona, both evolution and interactions occur en route to Earth, and substructures may form and change via plasma instabilities or turbulence. The plasma encompassing the outer corona and inner heliosphere before significant interplanetary processing (the “young solar wind”) is a fundamental missing piece of the Sun-Earth connection.

Despite decades of study (e.g., Neugebauer and Snyder 1966; Hundhausen 1972; Lopez 1987; Marsch and Tu 1993; Sheeley *et al.* 1997a; Zurbuchen *et al.* 1998; Bruno *et al.* 2001; Borovsky 2008; Suess *et al.* 2009; Cranmer, Gibson, and Riley 2017; Viall and Borovsky 2020; Viall, DeForest, and Kepko 2021), quantitative insight into the origins of solar-wind structure and variability has been limited by a lack of direct observations. As a result, scientific studies have remained heavily reliant on modeling to connect the remotely observed corona with heliospheric in-situ data (Odstrcil and Pizzo 2009; Provornikova *et al.* 2024). PUNCH is specifically designed to fill in this gap by imaging the evolving plasma with sufficient resolution and sensitivity to address the PUNCH science objectives, described in the subsections below.

## 2.1. Science Objective 1: The Ambient Solar Wind

The solar wind fills and defines the heliosphere (Parker 1958; Hundhausen 1972). Even in its ambient state, it is highly variable in both time and space. Ejecta, waves, and turbulence form a fluctuating background that is sensitive to local physical characteristics, yet also preserves information about the Sun. Streams of fast wind intersperse with slower flows, and the domain boundaries separating these streams evolve in response to coronal changes and to solar-wind hydrodynamic and magnetohydrodynamic (MHD) instabilities. Variations also occur in boundaries between physical regimes, e.g., the  $\beta = 1$  and Alfvén surfaces. The region between the middle corona (West *et al.* 2023) and Earth undergoes variability on all observable scales. PUNCH is designed to exploit this variability to measure flow itself (Section 2.1.1), the onset of large-scale turbulence (Section 2.1.2), and the important, but largely-unexplored, Alfvén surface (or zone) (Section 2.1.3).

### 2.1.1. Science Topic 1A: Solar Wind Flow

The Ulysses mission (McComas, Gosling, and Skoug 2000; von Steiger *et al.* 2000; McComas *et al.* 2002) revolutionized understanding of the heliosphere when its measurements revealed the solar wind’s latitudinal structure. Being an in-situ mission, Ulysses sampled only a single narrow locus along each orbit, and required years to do so. In contrast, imagers reveal instantaneous global structure. Many authors have analyzed solar wind acceleration in the low corona (e.g., Sheeley *et al.* 1997a; Wang *et al.* 2000). Deep-field imaging of the mid to outer corona (DeForest *et al.* 2016, 2018) reveals faint moving structures and inhomogeneities in the outer corona at all latitudes and solar wind speeds (Figure 3), demonstrating the feasibility of tracing solar wind flow and its variability throughout the transition from coronal flow into the separated regime of

the young solar wind. These measurements are necessary to constrain current incomplete understanding of solar wind acceleration flow, (e.g., Cranmer and Winebarger 2019).

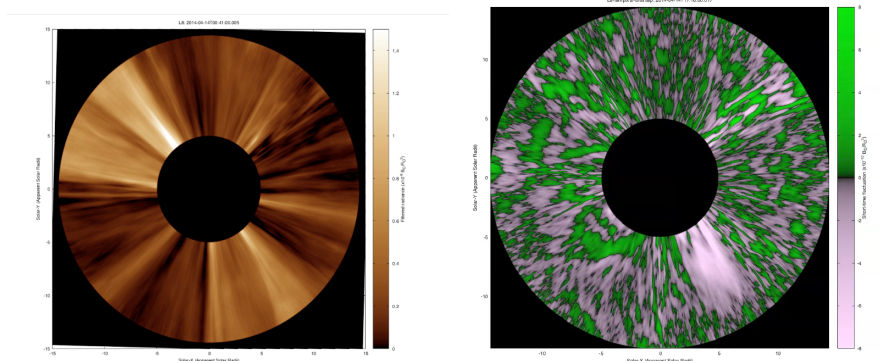


**Figure 3.** STEREO COR2 white light coronagraph observations from a deep-field campaign (DeForest *et al.* 2018), with 72 hours of long exposures at 5-minute cadence, reveal outer coronal structure. Left image has had smooth background and stars removed, showing the outer corona dominated by fine “woodgrain” structure. Outflow is visible everywhere because of small moving features, and further processing (right image) shows a riotous torrent of blobs and variable streams, tracing flow of the young solar wind.

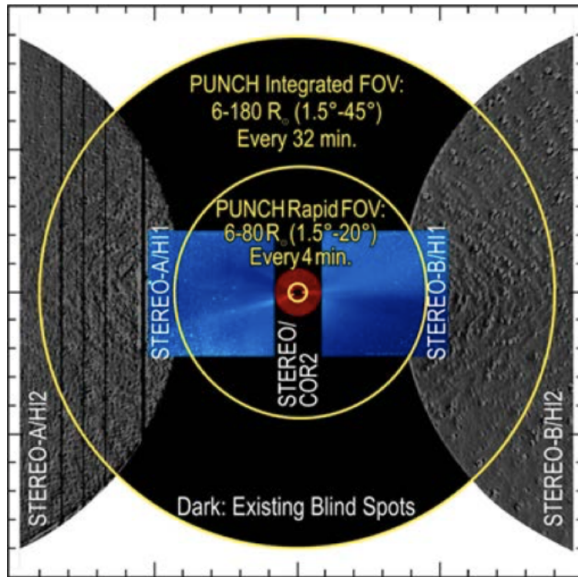


**Figure 4.** PUNCH eliminates observational gaps between coronal and heliospheric imagers and at the poles, continuously observing the young solar wind with a global field of view (FOV). Shown are STEREO COR2 and HI FOVs, within the full PUNCH FOV.

PUNCH’s global field of view (Figure 4) enables continuous tracing of inhomogeneities over all latitudes via deep-field images 10 to 30 times more sensitive than previous coronagraph/heliospheric images and collected every few minutes.

Velocity maps are extracted through flow tracking techniques including routine correlation tracking of these inhomogeneities (Attié *et al.* 2025).

These observations enable analysis of solar wind acceleration from the outer corona to the inner heliosphere, the changing boundaries between fast and slow solar wind, and the global conditions through which transient structures propagate. They also provide observational ground truth for comparison with theoretical and simulation predictions of evolving global flow, validating and/or falsifying models of solar wind acceleration.

### 2.1.2. Science Topic 1B: Mesostructures and Turbulence

The solar wind near Earth is dominated by fluctuations of unknown origin. Mesoscale structures (those between the small-scale kinetic regime and large structures like coronal mass ejections or stream interaction regions) may form mainly from solar wind turbulence (Elliott *et al.* 2010; Matthaeus and Velli 2011; DeForest *et al.* 2015), from solar-wind release (Sheeley *et al.* 1997a, 2009; Borovsky 2008; Rouillard *et al.* 2010; Viall *et al.* 2010; Neugebauer 2012; Hardwick *et al.* 2013; Kepko *et al.* 2016), or from a combination of both processes. The dichotomy of mechanisms, and open questions surrounding these mesostructures,<sup>4</sup> were recently reviewed by Viall, DeForest, and Kepko (2021). Mesostructures are small in heliospheric imagers, but large compared to Earth’s magnetosphere; they are therefore important daily drivers of geospace dynamics and space weather (e.g., Viall, Kepko, and Spence 2009; Di Matteo *et al.* 2022; Kurien *et al.* 2024).

The characteristics and formation locations of mesostructures are important constraints on models of solar-wind origin and acceleration. In particular, they distinguish models that invoke steady flow along the edges of coronal holes (Suess *et al.* 1998; Vásquez, van Ballegooijen, and Raymond 2003; Wang *et al.* 2007) from those that are intrinsically intermittent through interchange reconnection or multiple ejections of small plasmoids (Suess, Wang, and Wu 1996; Fisk *et al.* 2003; Endeve, Holzer, and Leer 2004; Rappazzo *et al.* 2005; Chen *et al.* 2009; Antiochos *et al.* 2011; Uritsky *et al.* 2021; Raouafi *et al.* 2023).

Some mesostructures are present in the outer corona and visible in Thomson-scattered light. Two classes of mesoscale density features in the solar wind have been identified out to 0.3 AU; “puffs” (including quasiperiodic density features) that originate in the corona (Viall *et al.* 2010; Viall and Vourlidas 2015), and “flocculae,” that become apparent at distances between 0.1 and 0.3 AU (DeForest *et al.* 2016). Both kinds of variability are faintly discernible with STEREO/SECCHI, but in-situ observations (Viall, Kepko, and Spence 2008; Kepko, Viall, and DiMatteo 2024) suggest a zoo of similar mesostructure at scales just below the sensitivity limit of that suite. The location and distribution of such features probes the  $\beta = 1$  surface, where the Sun’s magnetic field becomes too weak to stabilize flows against hydrodynamic instabilities in the solar wind.

<sup>4</sup>The term “microstructure” has been used since at least the 1990s by the solar imaging community (Sheeley *et al.* 1997b). We use “mesostructures” instead, because the “micro-” prefix, used in the context of solar wind science, implies plasma kinetic scales – which are much smaller than the resolution of current imagers including PUNCH.

Evolution of solar wind mesostructures is also a strong probe into the development of large-scale turbulence in the young solar wind. Turbulence may be the key to solving the “solar-wind heating problem,” that the solar wind does not cool as expected from adiabatic expansion. For example, at 1 AU the temperatures are 100 times higher than expected from adiabatic propagation alone. It has been proposed that kinetic energy, entrained in large-scale turbulence, cascades downward to kinetic scales in the solar wind, heating it via plasma dissipative effects (Coleman 1968; Leamon *et al.* 1998). In-situ measurements have revealed a turbulent cascade with a well-established inertial range at 1 AU (Marsch and Tu 1993; Goldstein and Roberts 1999). Coronal observations suggest the existence of turbulence there as well (Coles and Harmon 1989; Chae, Schühle, and Lemaire 1998; Kohl *et al.* 2006; Tomczyk and McIntosh 2009; Liu *et al.* 2014; Cranmer 2020), but how and where a turbulent cascade develops remains unclear (Zank and Matthaeus 1992; Chhiber *et al.* 2018). Analysis of images from STEREO/HI-1 (DeForest *et al.* 2016) has shown that the visible radial structures (“striae”) of the solar corona break up via currently unresolved processes at apparent distances between  $10^\circ$  and  $20^\circ$  ( $40 R_\odot$  to  $80 R_\odot$ ) from the Sun. The striae exhibit small lateral motions and spectral evolution, seen close to the HI-1 noise floor, that may indicate the development of a turbulent cascade (Figure 5).

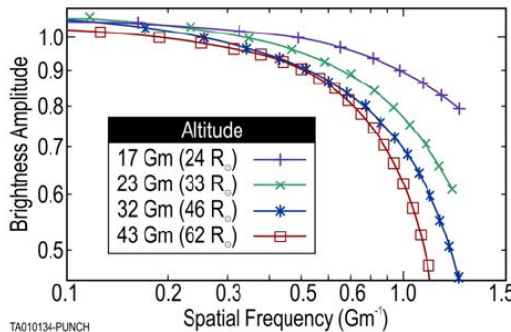


**Figure 5.** PUNCH is designed to reveal the development of turbulence in the solar wind. Observations of white-light brightness from STEREO/SECCHI reveal spectral steepening with altitude, suggesting onset of turbulence. With 10 times higher sensitivity, PUNCH is designed to resolve the hinted inertial range at spatial frequencies up to  $5 \text{ Gm}^{-1}$  (200 Mm scale) and to altitudes of 150 Gm.

By identifying small faint features, including puffs and perturbations of coronal striae, and locating them in 3D through polarization analysis (Appendix B), PUNCH is intended to explore the origin of solar-wind variability (intermittence of the solar source, unstable propagation dynamics, or a combination of the two) and observe the possible development of an inertial range of turbulent scales in the young solar wind. A wide range of mesostructures can be tracked as they form, evolve, and propagate into the heliosphere, determining their relationship to each other and to the hypothesized turbulent evolution of the solar wind. Recent studies with Parker Solar Probe have shown that the turbulent characteristics of the young solar wind within and just above the corona itself, i.e. at

solar elongation angles of roughly 10-40  $R_{\odot}$  from Earth, are quite different from those higher in the inner heliosphere (e.g., Zhao *et al.* 2022; Zank *et al.* 2022; Bandyopadhyay *et al.* 2022). By separating variation in time from variation in space, PUNCH extends these analyses to probe the onset, development, and potential isotropization of a turbulent cascade in the young solar wind.

Analyzing turbulence with image data gives rise to unique challenges of interpretation, arising from the line-of-sight integration and the angular (rather than Cartesian) sampling of those lines of sight (e.g., DeForest *et al.* 2016, their Appendix A). Pecora *et al.* (2024) discuss at some length the nuances of interpreting PUNCH data to analyze turbulence in the corona and solar wind. Wang *et al.* (2024) cover analysis of the possible energy-bearing  $f^{-1}$  spectrum of density fluctuations in the corona.

### 2.1.3. Science Topic 1C: The Alfvén Surface

The coronal plasma is in a state of constant expansion into interplanetary space, where it forms the solar wind. The boundary where the radial flow speed exceeds the fast-mode magnetosonic wave speed is a critical surface beyond which information cannot propagate back down to the Sun, at least in the form of MHD waves (Weber and Davis 1967; Hundhausen 1972). This “Alfvén surface”, so called because the relevant fast-mode speed is the Alfvén speed, is a natural outer limit of the corona itself, marking a natural border between the extended solar corona and the disconnected solar wind. It is the true source surface of the interplanetary magnetic field, and its shape and location are strong discriminators among solar wind acceleration models. It also plays a role in stellar rotational spin-down (Garraffo, Drake, and Cohen 2015), which is relevant to the Sun’s past and future evolution (Metcalfe, Egeland, and van Saders 2016).

Models (e.g., Cranmer, van Ballegooijen, and Edgar 2007; Verdini, Velli, and Buchlin 2009; Zhao and Hoeksema 2010; Goelzer, Schwadron, and Smith 2014; Tasnim and Cairns 2016) place the location of the Alfvén surface between about 10 and 30  $R_{\odot}$ , with a complexity that evolves and changes with the solar magnetic cycle. Fourier filtering of images has revealed the existence of inbound features out to about 15  $R_{\odot}$  (DeForest, Howard, and McComas 2014), but there remain difficulties matching the observed speeds and accelerations with solar wind models (Verdini, Velli, and Buchlin 2009; Tenerani, Velli, and DeForest 2016). It may be the case that these inflowing parcels are associated with nonlinear MHD structures such as shocks, jets, or shear instabilities (Cranmer, DeForest, and Gibson 2021), complementing expected outflowing parcels from reconnection in the outer corona and heliosphere (Gosling *et al.* 2005; Khabarova *et al.* 2016).

In addition, the results of the STEREO deep-field campaign (Figure 3) suggest that density inhomogeneities may be so great as to disrupt a well-formed Alfvén surface. In particular, electron density may vary by up to a factor of 10 on the smallest resolved outer coronal scales of a few tens of Mm (see also Raymond *et al.* 2014), affecting the speed of MHD waves (slower in dense regions; faster in evacuated regions). For this reason, it may be more appropriate to think in terms

of a fractal or frothy Alfvén zone, with profound implications for the nature of the interplanetary magnetic field boundary (Chhiber *et al.* 2022).

Recent in-situ studies with Parker Solar Probe have explicitly identified coronal regions where inbound waves are present, and have therefore identified the Alfvén surface and loci within it (Kasper *et al.* 2021; Ran *et al.* 2024; Huang *et al.* 2024). Although these in-situ measurements are groundbreaking and extremely important, they cannot in principle determine the global structure of the surface.

PUNCH studies the location of the Alfvén zone through analysis to separate inbound and outbound features in the solar wind, and determine the region above which inbound motions cease. Across time, the shape, complexity, and evolution of this zone, and the Alfvén speed itself, are determined through direct measurement of feature motions. Although particular moving features may be due to bulk motion of mesostructures or to waves (Tenerani, Velli, and DeForest 2016), in either case the Alfvén speed of the surrounding medium limits the relative speed of the bulk flow and the visible feature (Cranmer, DeForest, and Gibson 2021), enabling PUNCH’s visual-tracking approach to identifying the Alfvén surface (or zone). PUNCH science on this topic is described in more detail by Cranmer *et al.* (2023).

## 2.2. Science Objective 2: The Dynamic Solar Wind

The impact of large, dynamic structures such as coronal mass ejections (CMEs), stream interaction regions (SIRs), and shocks on the solar wind and geospace is well documented (e.g., Schwenn 2006; Pulkkinen 2007). A deeper understanding of the physical processes controlling these space-weather drivers holds the key to improvements in predictive capability. However, tracking, monitoring, and diagnosing even the most basic physical properties of transients (speed, density, morphology) has remained limited and challenging. This motivates PUNCH’s improvements in resolution, FOV, and photometry, and also its polarimetric capabilities, which can improve predictions of CME and SIR location and arrival time (Howard *et al.* 2013). 3-D localization using polarimetry improves on unpolarized stereoscopy alone, by eliminating multiple-viewing-angle confusion effects. Large-scale structures may be located in several ways: constraint of kinematic envelope models (Howard *et al.* 2013), direct analytic location of substructures (DeForest, de Koning, and Elliott 2017) and kinematically constrained tomographic inversion (Jackson *et al.* 2006; Bisi *et al.* 2008; Jackson *et al.* 2011; Morgan 2015), as well as forward modeling (e.g., Talpeanu *et al.* 2020).

### 2.2.1. Science Topic 2A: Coronal Mass Ejections

Coronal mass ejections (CMEs) are the largest perturbations of the solar wind, and the source of the strongest space weather events at Earth. They have been objects of study since the 1970s. However, many aspects of CME physics, particularly how they propagate and evolve through the solar wind medium, have not been well constrained by measurement. Earlier imagers could track only the largest or brightest components of CME structure beyond  $20 R_\odot$ , yielding

limited information about how CME sub-structures interact with each other or with the solar wind, despite a handful of joint tracking/in-situ studies of particular events (e.g., Howard and DeForest 2012a; DeForest, Howard, and McComas 2013; Palmerio *et al.* 2024). PUNCH is designed to enable analysis of not only bulk CME bodies, including the front trajectory and possible bulk deflection, but also the interior features that may be remnants of the source structure in the lower corona.

The structure and orientation of CME magnetic fields at the Earth largely determine space-weather impact, representing a central challenge for heliophysics. Current understanding of CME magnetic structure is based on in-situ sampling (Gosling *et al.* 1987; Lepping, Jones, and Burlaga 1990), in combination with near-Sun measurements of CMEs (Dere *et al.* 1999) and their precursors (Gibson 2015). These observations generally support a model of CMEs as magnetic flux ropes (Vourlidas *et al.* 2013). However, CME magnetic structures are known to change in the solar wind due to distortion (Howard and DeForest 2012b), deflection and rotation (Isavnin, Vourlidas, and Kilpua 2014), CME-CME interactions (Gopalswamy *et al.* 2001), and magnetic reconnection/erosion (Gosling *et al.* 2005; Ruffenach *et al.* 2015). Assuming the axis of the CME flux rope can be obtained through model or bulk 3D measurement, its chirality follows from the direction of circulation about the axis (DeForest, de Koning, and Elliott 2017).

PUNCH science on the topic of CME propagation and evolution is described in more detail, including a thorough review of recent work, by Malanushenko *et al.* (2025).

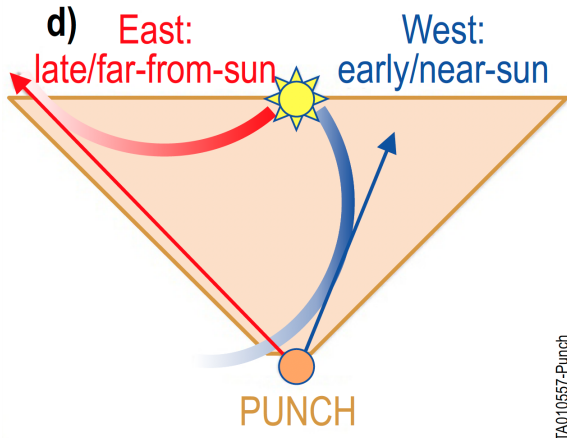


**Figure 6.** PUNCH observes both early and late manifestations of SIRs, enabling analysis of their birth and evolution.

### 2.2.2. Science Topic 2B: Stream Interaction Regions

Stream interaction regions occur at the interface between radial fast and slow solar-wind streams whose sources rotate with the Sun (Smith and Wolfe 1976;

Pizzo 1978, 1980, 1982). Although CMEs are the focus of much current space-weather related work, the quasi-stationary SIRs (including their long-lived subset, co-rotating interaction regions or CIRs), are also a significant source of space weather, particularly in the Earth’s radiation belts (Miyoshi and Kataoka 2005).

Prior to STEREO/HI, SIR research mainly depended on radio interplanetary scintillation (IPS) observations (Breen *et al.* 1998; Bisi *et al.* 2010; Dorrian *et al.* 2010) or used in-situ measurements that typically sample a single track through the feature (Tappin, Hewish, and Gapper 1984; Pizzo and Gosling 1994; Möbius *et al.* 2002; Bucik *et al.* 2009). From the wide-angle view on SIRs provided by heliospheric imagers, we now know SIRs manifest very differently depending on whether one observes from ahead looking east, or from behind looking west (Wood *et al.* 2010). In particular, the east view observes the advancing SIR structure along its developed part, far from the Sun, while the west view observes along a much closer, earlier phase of evolution during the short interval as the SIR sweeps past (Figure 6).

In addition to differences expected from simple geometry (Sheeley *et al.* 2008; Tappin and Howard 2009) we see other distinctions between the two views such as several ray-like features that appear to run into the SIR in the East view (Rouillard *et al.* 2010; Williams *et al.* 2011; Conlon *et al.* 2015). Meanwhile, the west view of the SIR structure (Sheeley *et al.* 2008; Rouillard *et al.* 2009, 2010) exhibits distortions and wavelike transients that are mostly short-lived and difficult to track far from the Sun. These are the likely signatures of the early formation of the SIR at the solar-wind regime interface, but their relationship with the later-forming portion of the SIR, the solar wind, and embedded mesoscale structures remains unknown.

PUNCH’s high spatial and temporal resolution, polarimetry, and wide FOV encompassing both eastward and westward directed views are designed to enable a 3D understanding of interplanetary SIR fronts and to track evolution of developing turbulence and other substructure in the fronts themselves, to better understand these sparsely-studied, yet very large, elements of the inner heliosphere. The mesoscale structure within SIRs, that PUNCH will image and track, is of particular importance in understanding the space weather impact of SIRs on geospace (e.g., Kilpua *et al.* 2015; Turner *et al.* 2019; Kepko and Viall 2019; Katsavrias *et al.* 2025).

PUNCH science on this topic is described in more detail by de Koning *et al.* (2025).

### 2.2.3. Science Topic 2C: Shocks

The basic geometric theory of interplanetary shocks is well established (Hundhausen 1985), but large-scale shock structure is rarely simple. Shock morphology depends on the surrounding medium (Odstrcil and Pizzo 2009; Tappin and Simnett 1997). Many shocks and CME sheaths appear to have an asymmetric structure (Pizzo *et al.* 2011; Feng *et al.* 2012). Further, some shocks appear to form on the CME flanks rather than, as expected, at its nose where density pileup is greatest (Ontiveros and Vourlidas 2009; Wood *et al.* 2009; Wood, Howard, and Socker 2010).

Changes in hydrodynamic shock behavior from turbulence are well documented by aerodynamics studies (Ribner 1953; Crighton and Leppington 1969) and laboratory experiments (Plotkin and George 1972; Williams and Howe 1973; Ribner 1986). Magnetohydrodynamic shock-turbulence interactions are just as strong (Zank *et al.* 2003) and turbulence significantly strengthens shock magnetic fields (Giacalone and Jokipii 2007). Simulations suggest that CMEs are strongly affected by turbulent instabilities across their shocks (Odstrcil *et al.* 2011), and some in-situ shock measurements suggest a corrugated shape (Szabo and Lepping 1995; Kasper *et al.* 2005) indicating their turbulent instability or fluctuations associated with solar-wind variability may be distorting shock fronts. Such shock corrugations may be responsible for the acceleration of solar energetic particles (SEPs) and type II radio bursts, but are currently not resolvable (Cairns *et al.* 2003; Knock *et al.* 2003).

Prior generations of coronagraphs and heliospheric imagers have been used to explore shocks, as well as the interaction of CMEs with each other and with other large-scale structures such as SIRs (Lugaz *et al.* 2012; Liu *et al.* 2012; Temmer *et al.* 2012; Harrison *et al.* 2012; Möstl *et al.* 2012; Wood *et al.* 2012). 3D analyses using the Solar Mass Ejection Imager (SMEI) data (Jackson *et al.* 2009, 2011) show that shocks appear “spotty,” reminiscent of expectations for turbulent instabilities. However, such studies have been severely hampered by limitations associated with instrument sensitivity and motion blur.

PUNCH is intended to observe the spatial irregularities and brightness variations of solar-wind CME interactions on scales 10 to 30 times below the scale of the structures’ gross envelope. This should provide a cross-scale picture of shock formation and shock turbulence interactions, and CME/SIR interactions, allowing the exploration of solar-wind variability on interplanetary shock behavior. The PUNCH science topic of shock physics is described in more detail by Dayeh *et al.* (2025).

### 3. Science Requirements

Engineering requirements are central to development of any mission, because large projects in general and space missions in particular represent trades between capability and cost. Because the process to develop mission-level requirements is not as familiar in the scientific literature as reporting of the resulting instrument performance, we describe here both the PUNCH top-level observing requirements and an overview of the methodology used to develop them.

Each topic in Section 2 levies specific scientific observing requirements on the PUNCH mission: aspects of observation that are needed to resolve the corresponding science question. These requirements, such as spatial/angular resolution and photometric sensitivity, are specific to each topic and were derived from review of the scientific literature at the start of mission definition. Distilling these scientific requirements into testable engineering requirements meant establishing a complete minimum set of mission parameters to constrain, rendering all the individual constraints on those parameters into a form that is directly comparable across questions, and identifying a notional set of “Baseline

Science Requirements” (BSRs) that would satisfy all of the science questions. These requirements became the mission definition. We executed the full derivation process twice, using two different criteria. We developed the BSRs using best-estimate observing requirements to fully address each particular scientific question, with an identified analysis path to closure of the question. We also developed a separate set of “Threshold Science Requirements” (TSRs) based on best-estimate observing requirements to significantly advance each scientific question. The BSRs were used by the instrument and engineering teams to derive a series of lower level requirements which, in turn, drove each aspect of the mission design. The TSRs provided understanding of how flexible each requirement might be, enabling development trades or compromises in case they were needed.

Developing mission top-level requirements itself requires compromise between three motivations: first, the desire to fully constrain the capability of a new instrument suite, which determines the minimum set of requirements; second, the need for each requirement to fully verifiable during development, which forces each requirement to refer to testable properties of the mission (without reference to the science target); third, the need for requirements to be feasible, which forces simple structure and requirements that can be analyzed and tested straightforwardly.

PUNCH science is broad enough that several requirements were challenging to specify. The needed image resolution varies across the field of view and is therefore specified at two representative solar elongations. Observing cadence varies for different targets and drives overall mission design, so the requirement is more complex to avoid overspecification. Photometric sensitivity is coupled to image resolution, and therefore required a novel formulation. These nuances are more fully described in the subsections below.

Table 1 lists the seven BSR requirements; their rationales are in the sections below.

### 3.1. Field of View and Duration

The PUNCH overall field of view (FOV) is required to subtend a minimum of  $270^\circ$  in position angle around the Sun. This angle ensures that, regardless of orientation, the field covers both polar and equatorial regions of the Sun. The mission achieves  $360^\circ$  coverage in the typical case, although lunar interference was calculated, pre-flight, to “wash out” up to  $45^\circ$  of position angle for a few days each month.

PUNCH images are required to extend inward to below  $8 R_\odot$  (solar elongation  $\varepsilon \leq 2^\circ$ ), to capture coronal dynamics below the pre-flight best estimated altitude of the Alfvén zone; this altitude is driven by all three of the Objective 1 topics. The field extends outward to  $45^\circ$  to track CMEs well out into the heliosphere and identify internal evolution and/or possible deflection.

The mission duration is set by the need to observe ten well-presented large CMEs over the course of the mission lifetime (Section 2.2.1). Based on a launch into the active phases of the solar cycle, existing counts in the CaCTUS catalog (Robbrecht, Berghmans, and Van der Linden 2009), and a selection factor of

**Table 1.** The seven PUNCH Baseline Science Mission Requirements (BSRs) define the observing characteristics of the mission, and drive the engineering requirements structure. Each requirement is explained in the corresponding section below. Requirements 3, 4, and 6 are specified at two separate representative elongation angles  $\varepsilon$ . Some BSRs were fully verified in-flight before article submission; they are marked in *italics*.

Title	Requirement	Performance design/ <i>measured</i>	Driver (topic)	Section
1: FOV position angle $\alpha$	$\geq 270^\circ$	$360^\circ$	all	3.1
2: FOV elongation $\varepsilon$	$2^\circ - 40^\circ$	$1.5^\circ - 45^\circ$	2A	3.1
3: Angular Resolution	$\varepsilon = 3.75^\circ: \leq 3'$ $\varepsilon = 20^\circ: \leq 5'$	$1.4'$ $1.8'$	1B 2C	3.4
4: Photometric Sensitivity ( $\times 10^{-17} B_\odot: 1^\circ$ , 4 min)	$\varepsilon = 3.75^\circ: \leq 320$ $\varepsilon = 20^\circ: \leq 10$	200 3	1B	3.2
5: Observing Cadence	Per Table 2	<i>Exceeds</i>	all	3.4
6: Polarimetric Sensitivity ( $\times 10^{-17} B_\odot: 1^\circ$ , 4 min)	$\varepsilon = 3.75^\circ: \leq 640$ $\varepsilon = 20^\circ: \leq 20$	300 5	1B 2A	3.3
7: Mission Duration	>15 months	24 months	2A	3.1

**Table 2.** PUNCH cadence requirements vary with elongation angle  $\varepsilon$  across the field of view, based on each science question.

FOV	$\varepsilon$ range	Requirement	Performance	Driver
Inner	$2.5^\circ - 30^\circ$	Image pairs: $\leq 8$ min. cadence; $\leq 24$ min. gap between pairs	4 min. cadence, $< 16$ min. gaps	1A,2C
Middle	$5^\circ - 27.5^\circ$	20 min. cadence	4-12 min.	1C,2B
Outer	$2^\circ - 40^\circ$	40 min. cadence	4-30 min.	1B,2A

2.5% to account for CME size, presentation, direction of propagation, overlap, and lunar interference, we estimated 0.025 well-presented, well separated, front-side “PUNCH large CME events” per day, driving a mission duration requirement of 15 months and (with margin) the overall mission design duration of 24 months.

### 3.2. Photometry

PUNCH photometric sensitivity is specified in “normalized  $B_\odot$ ” units, defined below. “Sensitivity” refers to the instrument’s ability to distinguish a feature of the specified radiance (SI units:  $W m^{-2} sr^{-1}$ ) against the measurement noise floor. Radiance is specified in units of  $B_\odot$ , the mean solar photospheric radiance ( $2 \times 10^7 W m^{-2} sr^{-1}$ ), because the Sun itself illuminates the corona and solar wind (e.g., Billings 1966; Howard and DeForest 2012b) and these units are

therefore both convenient and closely related to the optical depth of observed solar wind features.

Noise level (and therefore photometric sensitivity) in the PUNCH data is independent of the signal under study, because the main signal-dependent element of photometric noise (photon shot noise from the Thomson-scattered K coronal signal itself) is small compared to other sources. Significant contributors to the PUNCH photometric noise are photon shot noise from the F coronal background and starfield, read noise from the camera, and (in the far field) residual errors in the background model used to remove the starfield from the data (Section 6); all of these elements are fully or approximately independent of the signal from the solar wind, and we therefore treat them as a fixed “noise floor” against which the desired signal is compared to derive a signal-to-noise ratio (SNR). For specification, we consider sensitivity as bare detection, i.e. SNR=1 in the target feature.

Specifying a radiance sensitivity relevant to all the science topics is problematic because, even in PUNCH’s signal-independent noise regime, photometric uncertainty depends on the apparent size and required time resolution for each feature under study. In particular, the number of independent samples of the noise field is proportional to the solid angle (total number of pixels) occupied by a feature and to the length of time used to accumulate an image for analysis. These samples all add in quadrature so that in a feature of size  $\Omega_f$ , observed for a time  $t_{obs}$ , the noise  $N_f$  in the average brightness (radiance) of a feature scales as:

$$N_f = N_0 \sqrt{\Omega_0 t_0 / \Omega_f t_{obs}} \quad (1)$$

compared to a reference feature of apparent size  $\Omega_0$  with a photometric noise level of  $N_0$  in the same data set, observed for a reference interval  $t_0$ . In other words, given two different-sized features with similar brightness and background noise field, the larger feature will yield less average-brightness noise because its radiance is averaged across more pixels; and, likewise, averaging over more time will yield less noise, because the inferred overall radiance is an average over more exposures. Moreover, because  $\Omega_f \propto \zeta_f^2$  for similarly shaped features with linear image-plane scale  $\zeta_f$ , Equation 1 reduces to:

$$N_f = N_0 \frac{\zeta_0}{\zeta_f} \sqrt{\frac{t_0}{t_{obs}}} \quad (2)$$

where  $N_0$ ,  $t_0$ , and  $\zeta_0$  are constants of the observation (i.e. independent of the feature under study), and we use the greek  $\zeta$  to remind ourselves that image-plane scale is a measure of angle, not distance.

For convenience, we choose  $\zeta_0$  as  $1^\circ$  of apparent size ( $\Omega_0 = 1 \text{ deg}^2$ ), and normalize photometric sensitivity to that spatial scale; and likewise specify  $t_0$  as four minutes, to match the punch observing cadence described in Section 4.1 below, and normalize photometric sensitivity to that temporal scale. Using these normalized radiance units allows comparison between the sensitivities required for the six science topics, independently of the spatial and temporal resolution required for each.

Figure 7 shows the interplay between driving resolution and photometric requirements, prior instruments, and classes of feature in the corona and young solar wind. Loci of constant  $N_0$  form diagonal lines on that plot, reflecting the result (illustrated in Equation 2) that radiance sensitivity varies with spatial scale.

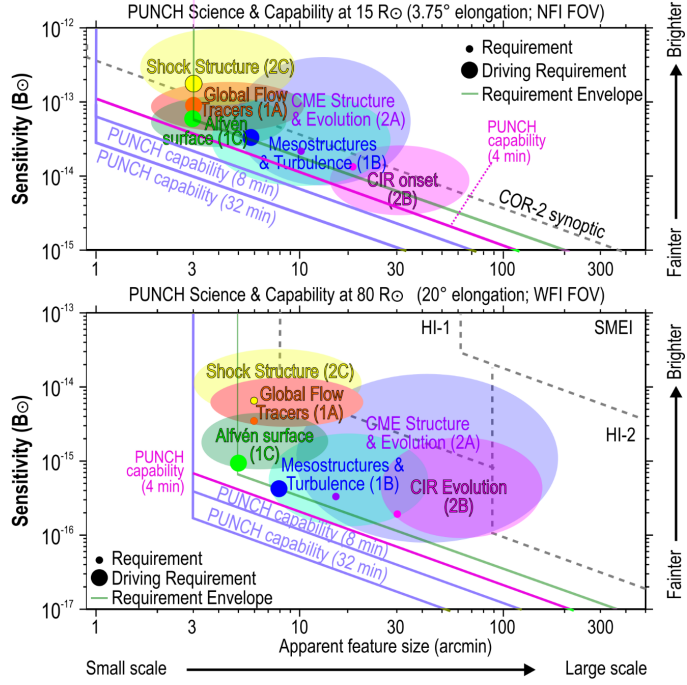


**Figure 7.** PUNCH resolution and sensitivity requirements are driven by the individual science topics, and are plotted relative both to known structures and existing instrument capability. Ovals represent particular science topics; green solid line represents driving requirements; dashed lines show the observing envelopes of prior missions. Diagonal sensitivity lines mark constant values of  $N_0$  and reflect the dependence of photometry spatial scale. In both the corona (TOP) and young solar wind (BOTTOM), topic 1C drives the resolution requirement and topic 1B drives the sensitivity requirement. Averaging PUNCH 4-minute-cadence images across time yields higher sensitivity as shown by the “8-min” and “32-min” lines at the bottom of each plot.

### 3.3. Polarization

Polarization sensitivity is driven by the need to resolve 3D locations of ejecta and CMEs (Sections 2.1.2 and 2.2.1). The basic theory of 3D imaging through polarimetry is in Appendix B. Crude linearization of the relationship between the polarization ratio  $pB/B$  and scattering angle  $\chi$  (Appendix B) yields a slope  $\Delta\chi/\Delta(pB/B)$  of roughly  $0.6^\circ$  per percent polarization, over most relevant values of  $\chi$ . This ratio connects precision of 3D spatial position to polarimetric precision for PUNCH observations. PUNCH’s polarimetric requirements are specified as photometric requirements on both  $B$  and the excess polarized brightness  $pB$ ,

based on the known brightness of target structures and the required precision of 3D location.

The relationship between photometry of individual camera images through a polarizing filter, and polarimetry using multiple images through a trio of such filters, is nontrivial but tractable via algebraic analysis. DeForest, Seaton, and West (2022) recently revisited that relationship via derivation from basic polarization physics. As a rule of thumb: noise levels in PUNCH unpolarized  $B$  data products (derived from triplets of images through polarizing filters) scale approximately as would those in sums of unpolarized exposures; while noise levels in  $pB$  data products from PUNCH are worse by a factor of at most  $\sqrt{3}$ , compared to the corresponding  $B$  data product.

### 3.4. Spatial and Temporal Resolution

Studying the interplay of turbulent and injected features (Section 2.1.2) drives PUNCH’s spatial resolution in the inner field. The size scale of Sheeley blobs (Sheeley *et al.* 1997b) observed with SOHO/LASCO is roughly  $10'$ ; determining whether there is significant substructure requires 3x over-resolution of the known features (DeForest 2007), leading to the requirement of  $3'$ . Studying shock evolution (Section 2.2.3) drives spatial resolution in the outer field, based on preliminary simulations showing possible shock “crinkling” via the Rayleigh-Taylor instability.

The temporal resolution requirement is different in different parts of the PUNCH field of view. The fundamental cadence is driven by flow tracking and shock front analysis (Sections 2.1.1 and 2.2.3) in the inner portion of the field of view. An 8 minute requirement derives from the need to avoid the “mistaken identity problem” (DeForest *et al.* 2007) in feature tracking, in which feature identity can erroneously shift from one visible feature to another if the observing cadence is too sparse. In the outer portion of the field of view, 40 minutes is required for coherent tracking of CMEs across the inner solar system.

PUNCH operates at a fundamental cadence of 4 minutes, providing margin against the 8 minute requirement, and in its nominal configuration the mission achieves 4 minute cadence at all elongations from the inner edge of the FOV to approximately  $20^\circ$  from the Sun (marked in Figure 2).

## 4. PUNCH Mission Design

The PUNCH mission design was set by physical constraints on dynamic range and data rate. Two separate instrument types (the NFI and WFI, described in Section 5, are required to capture the seven orders of magnitude in dynamic range across the field of view (Figure 10). An initial cost trade showed that over a two-year mission, ground station contacts would drive cost for a deep-space probe, and proved too expensive for a Small Explorer program. Operating from LEO reduced ground costs significantly, but also led to obstruction of the field by the Earth itself. Fortunately, the ready availability of commercial subsystems reduced the cost of a spacecraft enough that a four-spacecraft constellation

could be built and operated within NASA’s Small Explorer cost cap. PUNCH is therefore a “1+3” constellation, with one major instrument mounted on each of four interchangeable spacecraft, and an instrument complement comprising one NFI and three WFIs. The flight assets thus comprise four Observatories, each integrating a spacecraft and an instrument. We chose to fly NFI on its own spacecraft, rather than co-hosting it with a WFI, to maximize the cost benefit of uniform spacecraft design across the entire constellation.

#### 4.1. Orbit, launch sequence, and concept of operations

PUNCH launched into in circular low Earth orbit, initially 650km altitude (in the ionosphere topside F-region), in a Sun-synchronous configuration with 6am time of ascending node and 97.9° inclination. This orbit was chosen to ensure that the missions were always close to the ideal observing geometry relative to Sun and Earth.

The spacecraft coordinate system is defined such that  $+X$  (roll axis) is normal to the solar panels at the front of the spacecraft,  $+Z$  (yaw axis) is normal to the instrument deck, and  $+Y$  (pitch axis) forms a right-handed coordinate system. During science operations, each spacecraft maintains  $+X$  pointing at the Sun (via uplinked solar ephemeris), and rolls so that the zenith is close to the XZ plane.

PUNCH collects primary data on a 4 minute cadence, broken into 8-minute observing windows. During each observing window, all four spacecraft roll to place  $+Z$  ahead of the local zenith, then hold fixed Sun-pointing with inertial (celestial) roll constraint, while acquiring image data for approximately seven minutes. The acquisition times are synchronized to within  $\pm 1$  second across the constellation, and each camera acquires photons with an acquisition duty cycle above 50% (Figure 8). At 650 km altitude, the terrestrial horizon dip is 24.8°. The orbital period at the start of the mission is 98 minutes, gradually decreasing to 94.5 minutes shortly before re-entry. Therefore, over a single 8 minute observing window all four spacecraft traverse 29.4° of orbital anomaly, gradually increasing to 30.4° over the orbital lifetime of the mission. This pointing sequence maintains the Earth’s horizon a minimum of 9.5° below (-Z) the spacecraft XY plane at all times, compared to a requirement of 4° for WFI. This allows stray light control for WFI and passive cooling of the camera for all four instruments. All operations are scheduled around this regular, constellation-wide, sequence of 8-minute observing windows and the 4-minute regular cadence of data acquisition.

The observing sequence is diagrammed in Figure 8, which highlights the repetitive nature of the observations. Each polarized image sequence occupies approximately 3 minutes and comprises three image acquisition cycles through three polarizing filters oriented 60° apart in angle. In normal operations, each 8-minute observing window contains two such sequences, punctuated at the start by a pause to roll the spacecraft and at the center by a single clear (unpolarized) exposure from the instrument. Thus each observatory acquires seven images per 8-minute observing window.

The four-minute cadence of PUNCH observation, twice the required rate described in Table 2, was driven by the need to mitigate the “high altitude aurora”

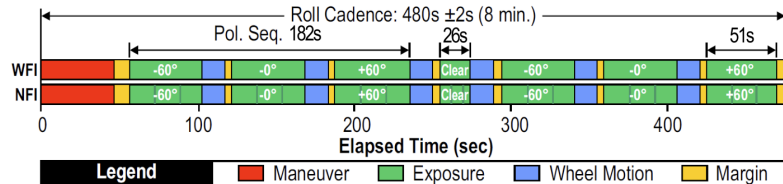


**Figure 8.** PUNCH observing sequence timeline begins each 8-minute observing window with a roll maneuver, then holds pointing for two three-exposure polarized image sequences and one clear (unpolarized) exposure. The polarized sequences form a uniform, 4-minute cadence data set. The observing sequence is repeated for the entire science mission, aside from minimal interruptions for calibration and maneuvering.

seen by the SMEI heliospheric imager (Eyles *et al.* 2003) above 800km altitude (Mizuno *et al.* 2005). The high altitude aurora is interesting in its own right but impacted SMEI’s solar wind imaging. Collecting a full polarized sequence every four minutes provides resilience against the aurora, because of the parallax from PUNCH’s orbital motion: if a particular camera frame is affected by the high-altitude aurora, the frame four minutes earlier or later is unlikely to be affected by the same feature in the same image location. The 8-minute clear sequence was chosen both as a backup for ease of post-processing and to double-check the analysis of the polarized sequences.

The approximately 30° roll sequence permits sky imaging even during lunar phases in which the Moon passes through the WFI field of view: even if certain WFI exposure frames are washed out by moonlight, frames from adjacent roll intervals are unaffected as the Moon is below the baffle plane. NFI sees the Moon during the new-Moon phase, but based on experience with earlier LEO coronagraphs (e.g., Solwind Sheeley *et al.* 1980) the NFI data were predicted to not be strongly affected; and “first light” imagery from 2025 May indeed shows that the new Moon does not impact NFI observations.

The 4-minute cadence sequence is planned to continue for the entire mission, interrupted at long intervals by calibration exposure sequences or orbital-trim maneuvers. Ground communications are via low-gain antenna and do not interrupt science. Orbital trim maneuvers, comprising a slew to rotate the -Z face to the prograde or retrograde direction, a few-second rocket thrust event, and a slew back to nominal science mode, are each fully contained within a single 8-minute observing window, to minimize impact to the overall observing cadence.

The four spacecraft launched together on a single Falcon 9 rocket, and spring-deployed at approximately 1 m/s from the launch vehicle. WFI-2 deployed in the forward orbital direction, NFI-0 in the reverse orbital direction, WFI-3 60° from the forward orbital direction, and WFI-1 60° from the reverse orbital direction. This caused the positions to spread gradually over the first 120 days of operation which were also used for spacecraft and instrument commissioning. A small rocket motor on each Observatory provides a few m/s of  $\Delta v$  both to arrest the relative orbital drift and to maintain the three WFI Observatories approximately 120° apart in orbit.

All four observatories compress and cache image data and then downlink stored images during ground passes. The three WFI observatories execute ap-

proximately one ground pass per day, and the NFI observatory executes approximately six ground passes per day.

#### 4.2. Spacecraft design

The PUNCH spacecraft are designed to be as similar as possible, with interchangeable mounting structures and electrical interfaces to support the lone prime-mission instrument on the top (+Z face) of each. The spacecraft body is a “bathtub” design with interior walls, fabricated from a single block of aluminum. The interior volume is closed out by a +Z deck lid that accommodates support brackets to mount the instrument. The -Z surface holds a Motorized Light Band (MLB) separation system used to interface each spacecraft to the launch vehicle.

Command and data handling (C&DH) are via a SwRI-supplied C&DH box built around a Centaur single-board computer, with ancillary cards for power handling, analog control, and digital control. The C&DH system manages spacecraft sequencing, regulation, and fault handling. It issues commands to commercially procured spacecraft subsystems and operates the instrument directly. The C&DH system collates and manages separate telemetry streams for engineering/housekeeping data and for science. These are coded, buffered, and transmitted as separate virtual channels, using the standard Consultative Committee for Space Data Systems (CCSDS) format.

Telemetry, commanding, and tracking are via a dual-band two-way radio, built by Tethers Unlimited Inc., that offers S-band uplink and both S-band and X-band downlink via low-gain antennas on the top and bottom decks of the spacecraft. The S-band link offers 5 Mbps data rate to the ground; the X-band link offers just under 25 Mbps. The receivers are programmed to respond to spacecraft-unique idle codes transmitted from the ground, affording specificity of contact even during the early phases of the mission when the four spacecraft were close together. The S-band is used for commanding and for engineering telemetry; and the X-band is used for downlink of science data. For resilience, either band can be used to downlink any type of data from the spacecraft. The X-band radio on board NFI-0 suffered a failure in observatory-level integrated thermal vacuum testing, and NFI-0 is therefore operated solely with S-band downlink, at an average rate of roughly one ground pass every four hours. The radios were intended to be used simultaneously, but a common manufacturing flaw in the radio units limits usage to one transmitter at a time.

The attitude determination and control system (ADCS) is an XACT unit made by Blue Canyon Technologies. The XACT uses twin star trackers for fine-pointing attitude determination in celestial coordinates (right ascension and declination). In nominal science operations, sun-pointing is achieved by directly commanding absolute celestial pointing minute to minute, using the solar ephemeris. This strategy permits continuous observation even during the inevitable “eclipse season” in which each spacecraft passes through Earth’s shadow once per orbit, near the unfavorable solstice. Each spacecraft does carry Sun sensors, which are used to ensure sun-pointing and spacecraft safety in off-nominal modes. XACT also uses a magnetometer and digital geomagnetic model to constrain solar roll angle when in coarse sun-pointing mode. The

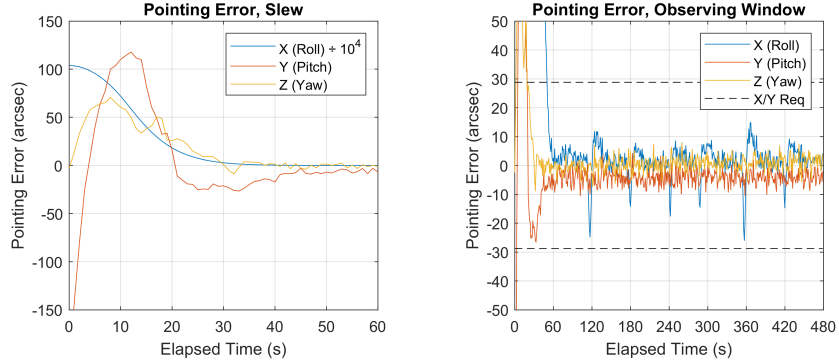


**Figure 9.** The PUNCH ADCS (Blue Canyon XACT) system exceeds performance requirements for slew recovery, filter wheel rotation recovery, and stability during camera exposures. Left:  $30^\circ$  roll slew and recovery. Right: performance during a typical 8-minute observing window. Polarizing filter wheel rotations, and the seven standard observing-sequence exposures (Fig. 8), are visible starting 60s into the 8-minute window.

ADCS operates its control loop on a 5 Hz cadence, maintains 16 arcsecond ( $3\sigma$ ) stability in fine pointing mode, uses quad reaction wheels, and manages its own angular momentum continuously via magnetic torque rods mounted in the spacecraft interior. It also includes a GPS receiver which is used to synchronize the on-board clocks across the constellation and (on the ground) to generate refined ephemerides and pass predictions for each spacecraft. The slew rate is sufficient to execute a  $30^\circ$  roll, and recover stability, in under 60 seconds. Stability requirement during exposures is  $\pm 30''$  in pitch (about the spacecraft Y axis) and yaw (about the spacecraft Z axis), and  $\pm 300''$  in roll (about the X axis, which is approximately aligned with the spacecraft-Sun line). On-orbit performance exceeds requirements for settling time after slews and after filter wheel rotations, and for stability between spacecraft and mechanism moves. Performance of WFI-1 during a typical 8-minute observing window is shown in Figure 9.

The propulsion system is a HYDROS unit, supplied by Tethers Unlimited, Inc., which uses water as propellant. A small water tank feeds an electrolyzer unit, which separates water into hydrogen and oxygen gases; these accumulate in twin plenums which are vented into a combustion chamber to produce rocket thrust in discrete “thrust events” that impart up to 2 cm/s of  $\Delta v$  over approximately 2 s. Each thrust event requires 1-2 ks of electrolysis time to prepare, and consumes approximately 0.5 mL of water. Electrolysis does not interfere with science data acquisition. The rocket nozzle is mounted on the -Z face of each spacecraft. Total  $\Delta v$  capability is approximately 20 m/s on each spacecraft, against a calculated requirement of 4-6 m/s, driven by estimated orbital perturbation rates from the geoid over a two-year mission.

The power system uses deployable solar arrays from Sierra Nevada Corp., together with SwRI power-management electronics incorporated into the C&DH box and a lithium battery from ABSL. Peak power trackers match the supply

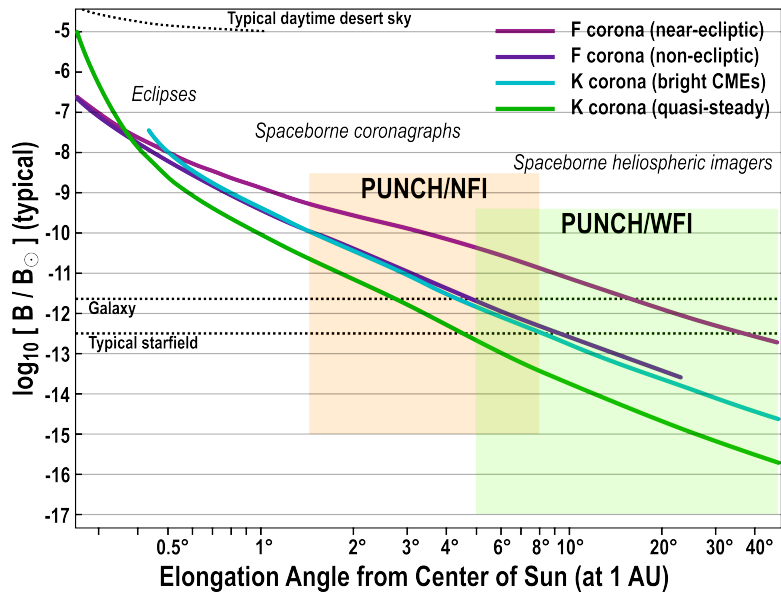


**Figure 10.** The PUNCH field of view captures an extremely broad dynamic range, spanning nearly seven orders of magnitude between the brightest F corona in the inner field and the quasi-steady K corona in the outer field. This requires two separate instrument types: a Narrow Field Imager (NFI) and a Wide Field Imager (WFI), with significant field of view overlap.

voltage of the solar arrays to the interior 28VDC bus voltage. Both switched and unswitched power buses are managed by power cards in the C&DH box.

The thermal control system is a cold-biased passive design with supplementary multi-zone digitally controlled management heaters and thermostatically switched survival heaters. Spacecraft subsystems dump heat into the body of the spacecraft. The instruments are thermally isolated from the spacecraft, and radiate their waste heat to space. The instruments include CCD cameras that are passively cooled by radiation to deep space; this takes advantage of the roll attitude program for WFI, and drives a similar roll program for NFI, both of which maintain the CCD radiator in shade on the +Z (zenith) side of the spacecraft bus.

The instruments are directly controlled by the C&DH system, via a SpaceWire interface to the camera system and electrical pulse interfaces to the instrument mechanisms. The instruments were specifically designed to be electrically identical and controlled the same way, simplifying C&DH and flight software design by reducing the functional differences between the instrument types to minor differences in on-board configuration tables.

## 5. PUNCH instruments

PUNCH operates as a single “virtual instrument” built from four individual physical instruments. The Narrow Field Imager (NFI; Section 5.1) and three Wide Field Imagers (WFIs; Section 5.2) are physically matched such that each

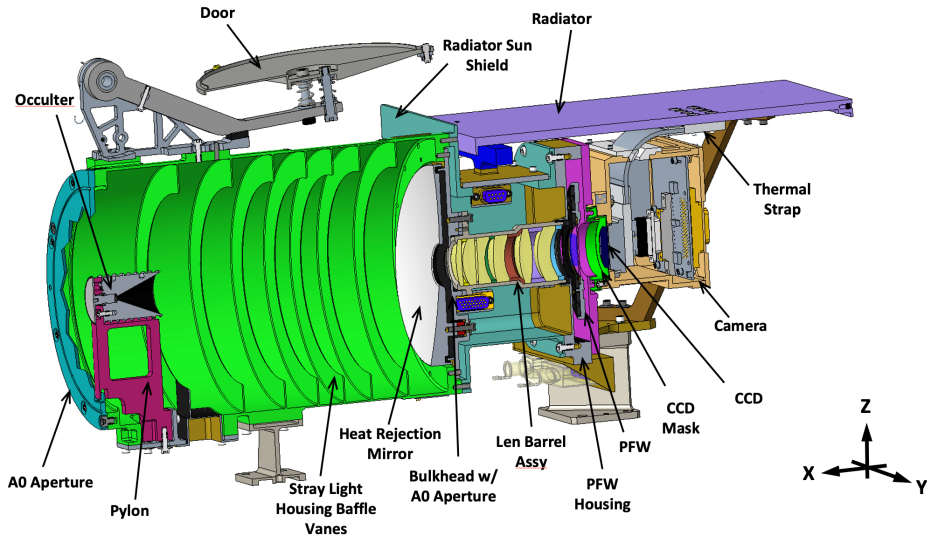


**Figure 11.** Cutaway drawing shows the structure of the PUNCH/NFI instrument and its major subsystems.

instrument's instantaneous field of view (IFOV) overlaps with each of the other three instruments' IFOVs; the wavelength passbands are matched at 450–750 nm; and the observing sequences are synchronized to make the merged science data as seamless as possible.

The two different instrument types are needed to accommodate the very wide dynamic range across the PUNCH field of view (Figure 10). The instrument types share two important common subsystems: a camera/CCD system (Section 5.3) and a polarizing filter wheel (Section 5.4). They are designed to mount interchangeably on the PUNCH spacecraft, and also share joint electronics and electrically-identical components for door actuation and thermal control.

### 5.1. Narrow Field Imager

The Narrow Field Imager (NFI) is an externally-occulted compact coronagraph design built by the U.S. Naval Research Laboratory (NRL). Figure 11. The instrument is a cutaway diagram of the instrument. Figure 12 is a photograph of the instrument undergoing stray light testing inside the SCOTCH vacuum chamber at NRL. NFI is described in detail by (Colaninno *et al.* 2025); the design is summarized here. NFI builds on a long history of coronagraph development, beginning with Lyot (1930) and extending through OSO-7 (Koomen *et al.* 1975), Skylab-ATM (MacQueen *et al.* 1974), Solwind (Sheeley *et al.* 1980), SOHO/LASCO (Brueckner *et al.* 1995), STEREO/SECCHI (Howard *et al.* 2008), and GOES/CCOR (Thernisien *et al.* 2021; Dudley *et al.* 2023).

In Figure 11, a front-end baffle assembly (green) supports an A0 aperture with a toothed outer edge that minimizes edge diffraction into the optics, and a pylon and occulter assembly that block direct sunlight from entering the optics. The occulter is

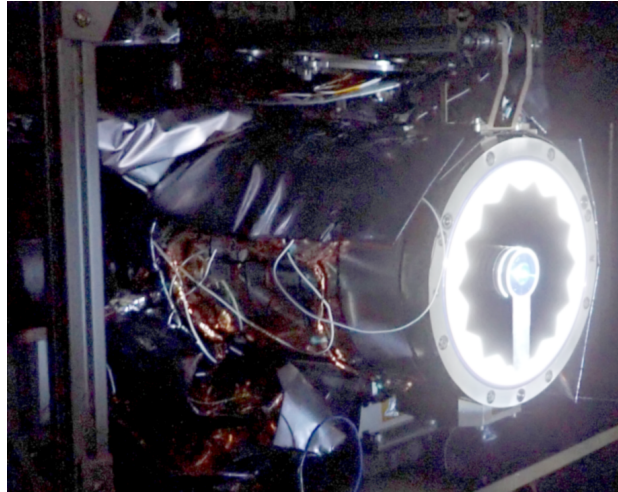


**Figure 12.** Photograph of NFI during stray light testing in NRL’s SCOTCH vacuum-testing facility shows the major front end elements diagrammed in Figure 11. The toothed aperture, single external occulter, and support pylon are brightly illuminated by a simulated solar beam; the instrument stray light housing baffle, covered in multi-layer insulation, is visible behind them. The door is open in the flight configuration at top.

a tapered-ogive<sup>5</sup> multi-disk design with a rear-facing conical light trap. The multiple disks force multiple diffraction scatter events, strongly attenuating diffracted sunlight. The conical light trap absorbs scattered light from the rear of the baffle assembly. Most sunlight entering the instrument impacts a spherical Heat Rejection Mirror (HRM) at the back of the baffle assembly, and is focused into the empty space opposite the pylon, and ejected into space. The HRM has a central hole that forms the aperture to a lens barrel assembly that focuses light through a polarizing filter wheel (Section 5.4) onto a CCD detector connected to an interface camera module, and operated by an external Camera Electronics Box (Section 5.3). The entire instrument was closed out, at launch, by a ground-resettable one-time-open door. The CCD is cooled by thermal conduction through a thermal strap to a radiator aimed at deep space. The entire instrument structure is supported on the spacecraft by a kinematic mount comprising three feet that bolt directly to the spacecraft.

PUNCH/NFI has an optical focal length of 103 mm and is operated at an aperture of  $f/4.5$ , yielding a plate scale of 0.5 arcmin per 15  $\mu\text{m}$  pixel. The field of view covers nearly all position angles  $\alpha$  around the Sun, extending across solar elongation (apparent radial) angles  $\varepsilon$  from  $6 R_\odot$  to  $33 R_\odot$  ( $1.5^\circ$ – $8.3^\circ$ ), with the diffraction “bright ring” on the occulter at exactly  $1.5^\circ$  from the Sun itself. Images acquired by the instrument are masked on-board PUNCH to  $5.7 R_\odot$  to  $32 R_\odot$ , to optimize downlink volume.

Each NFI image is acquired as a triple exposure on board PUNCH: three separate camera exposures (digitized to 16 bits) are summed on board to produce 20-bit-deep pixel values, which are further processed on-board (Section 5.3) for downlink. Each polarization sequence comprises three of these triple exposures: one summed triple exposure with the polarizing filter wheel in each of its three polarizing positions.

<sup>5</sup>Readers are reminded that an “ogive” is a figure of revolution of a circle, about a non-diameter chord of that circle; or a truncated segment of such a figure.

**Table 3.** Solar stray light requirements and values measured for NFI at three field-of-view locations, at NRL’s SCOTCH facility

Radial location	Requirement	Measured stray radiance
$6.6R_{\odot}$	$< 41 \times 10^{-11} B'_{\odot}$	$3.8 \times 10^{-11} B'_{\odot}$
$15R_{\odot}$	$< 13 \times 10^{-11} B'_{\odot}$	$5.8 \times 10^{-11} B'_{\odot}$
$27R_{\odot}$	$< 3.5 \times 10^{-11} B'_{\odot}$	$2.0 \times 10^{-11} B'_{\odot}$

During development NFI was tested for solar stray light rejection, at NRL’s Solar Coronagraph Optical Test Chamber (SCOTCH) facility (Korendyke 1993). SCOTCH is a long-tube baffled vacuum chamber with a solar simulator light source, designed to measure stray light while eliminating Rayleigh and Mie scattering from the air and dust present in a more typical laboratory environment. NFI was fully illuminated by the simulated solar beam, and light levels were measured in image data collected through the instrument itself. Solar stray light in NFI is dominated by backscatter off the HRM, which illuminates the rear of the occulter. Doubly scattered sunlight enters the optics, forming an out-of-focus image of the occulter itself, with effective radiance comparable to that of the solar F corona. This anticipated effect is removed in post processing in the science reduction pipeline, described in Section 6. Solar stray light from the simulated solar beam was measured at three radial locations; these are tabulated in Table 3. The stray light was measured with each of three polarizers in the beam, and with a clear (non-polarizing) filter. The largest of the three values is reported in Table 3. The units are given as  $B'_{\odot}$  rather than  $B_{\odot}$  to acknowledge linear scaling for the measured intensity of the simulated solar beam. NFI solar stray light meets design requirements at all locations.

During early operations, total stray light in the NFI instrument was found to be greater, and far more variable, than the solar stray light performance in Table 3. This has been attributed to variable Earthshine illuminating the interior of the baffle tube, and thereby scattering onto the rear of the occulter; the effect was not characterized during the SCOTCH testing campaign in the pre-launch phase. The additional variable stray light is up to  $5\times$  brighter than the solar stray light, though more typically  $0.2\times$  to  $2\times$  as bright; and is confined to the zone (inside of approximately  $22R_{\odot}$ ) covered by the defocused image of the occulter. The process to scrub this variable stray light from the data is the subject of a rapid development effort early in the mission; it is described in more detail by Hughes *et al.* (2025).

NFI sample data, collected during commissioning, included images of the new moon and of several bright CMEs. Example images are in Figure 13, and reveal the instrument’s high sensitivity and resolution even with preliminary data processing.

## 5.2. Wide Field Imager

The Wide Field Imager (WFI) is a corral-baffle heliospheric imager design; three were built for PUNCH at Southwest Research Institute (SwRI). Figure 14 is a diagram of WFI. Figure 15 is a photograph of one of the instruments, under development. WFI is described in detail by (Laurent *et al.* 2025); the design is summarized here. The is analogous to an externally-occulted coronagraph, in linear geometry (i.e. the baffle structure is approximately symmetric via extrusion along the spacecraft Y axis, rather than via revolution about the spacecraft X axis). Heliospheric imaging was conceived in the late 20th century using the three photometers of the spinning Helios mission (Jackson and

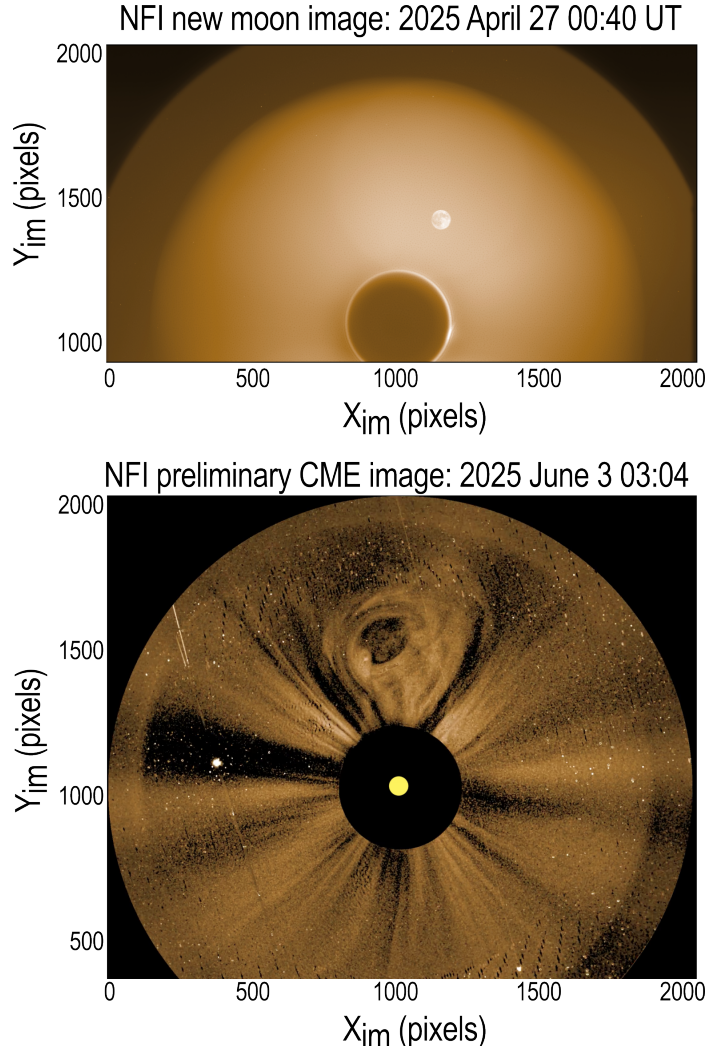


**Figure 13.** Early example images from NFI demonstrate instrument capability. Top: the new Moon first passed through the NFI FOV on 2025 April 27, providing a scale and brightness reference for the field of view. The Earth-illuminated Moon is approximately 2x brighter than the fixed +variable stray light pattern. Bottom: a northbound CME launched on 2025 June 2; preliminary data reduction shows that NFI resolved fine interior details of the CME as it passed through the outer corona.

Leinert 1985), and developed through Coriolis/SMEI (Eyles *et al.* 2003; Jackson *et al.* 2004), STEREO/HI (Howard *et al.* 2008; Eyles *et al.* 2009), SolO/SOLOHI (Howard *et al.* 2020), and PSP/WISPR (Vourlidas *et al.* 2016). The more modern designs include a full optical imaging system, a solar baffle, and a deeply vaned light trap to absorb glint; WFI is similar, with the addition of a lunar baffle near the optical aperture, to reduce flooding by moonlight.

The instrument body is a large flat corral fabricated from aluminum. The corral is surrounded by a flat lip (dark grey on  $\pm Y$  sides) that defines an instrument shadow

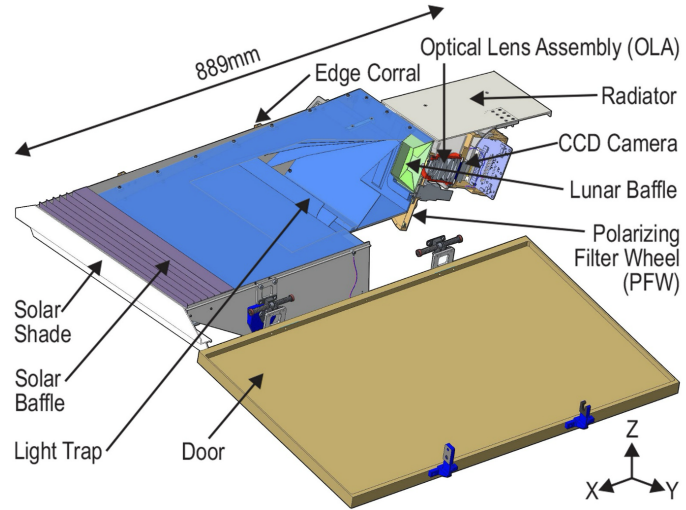


**Figure 14.** Cutaway drawing shows the structure of the PUNCH/WFI instrument and its major subsystems.

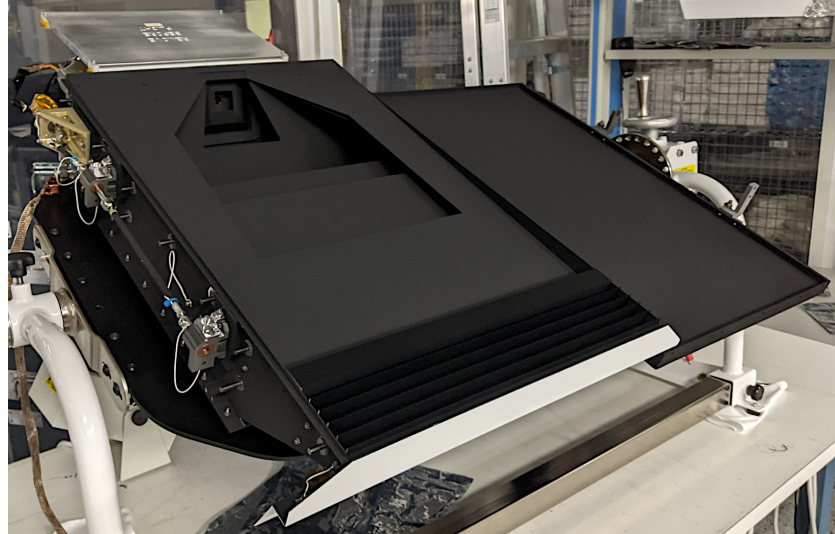


**Figure 15.** Photograph of WFI-2 during final instrument integration shows the major elements diagrammed in Figure 14. From front to back, the major features are the solar shade, coated in white thermal paint; the multi-vaned solar baffle, with its Acktar optical black coating; the deep light trap vanes, with Aeroglaze Z307 black coating; the square-geometry lunar baffle; and the optical aperture. The CCD radiator is protected by a protective shield. At left is the door release mechanism. The door is in its deployed flight configuration.

plane, hiding the Earth itself from the main baffle structure. The body supports a leading solar shade (white) that diverts the bulk of the solar beam away from the baffle and body, to avoid thermal flexure. The multi-vane solar baffle (periwinkle) intercepts sunlight that would otherwise enter the corral. It is machined from a single piece of aluminum and coated with optical black from Acktar Corporation. The baffle edges follow a cylindrical envelope that is analogous to the ogive shape of the NFI occulter, and enforce seven separate scattering events for any photon diffracted from the main beam around the baffle into the optics, following the applied scattering theory outlined by DeForest *et al.* (2025). Light that passes over the solar baffle crosses into the corral area, crossing over deep “light trap” vanes (blue) that are designed to absorb glint, moonlight, or other back-illumination of the instrument. At the rear of the light trap is a small lunar baffle (green) in square geometry. The lunar baffle is a conventional two-bounce design to reduce the field of regard, mitigating the effects of moonlight in the gibbous and full phases (when the Moon is outside the field of view but also bright enough to wash out WFI images). An aperture at the rear of the lunar baffle coincides with an external pupil of the optical design. The external pupil reduces stray light and provides room (optical “eye relief”) for a polarizing filter wheel (PFW; Section 5.4) in front of the optics. The image is projected onto a CCD (Section 5.3) and transferred to the spacecraft for processing and download.

PUNCH/WFI has an optical focal length of 35.2mm, operated at f/3.2 (11mm aperture), yielding a plate scale of 1.47 arcmin per  $15\text{ }\mu\text{m}$  pixel and an optical field of view (FOV) that is a circle truncated by the “horizon” of the solar vane. In nominal observing attitude, the Sun is on the vertical centerline of the image, below the horizon; the field of view extends along that centerline across elongation angles  $\varepsilon$  from  $20\text{ R}_\odot$  to  $180\text{ R}_\odot$  ( $5^\circ$ – $45^\circ$ ). The nominal FOV is an approximate square  $40^\circ$  on a side, truncated by a circle  $50^\circ$  in diameter, centered on the instrument boresight; the actual useful FOV is over  $55^\circ$  in diameter. Because WFI operates in linear geometry, the inner edge of the field of view may be adjusted by shifting the spacecraft attitude. To take advantage of the as-built stray light performance and field of view, all three WFIs are operated with the inner edge of the field of view close to  $12\text{ R}_\odot$  ( $3^\circ$ ) from the Sun itself. Images from WFI are masked to exclude areas below the horizon and outside the observed useful field of view, to optimize downlink volume.

WFI images are acquired in single exposures on board PUNCH: a single 51-second (polarized) or 26-second (unpolarized) image is read out at 16 bit dynamic range. Single-exposure acquisition improves signal-to-noise ratio (SNR) in the outer portion of the field of view, where image-independent camera read noise dominates the noise profile of the camera; the cost is that objects with magnitude 2.0 or less (brighter) saturate the image. There are on average 3.3 saturated objects in each WFI’s field of view throughout the mission. Accounting for bleeding artifacts, and the destreaking and PSF correction steps of the data processing pipeline (Section 6), these saturated objects invalidate an average of approximately 0.2% of the total WFI field of view from each frame. Because the instruments rotate every 8 minutes, the location of these artifacts changes rapidly so that the effect of any one artifact is minimized. The invalid pixels are marked in the calibrated data products.

One WFI was tested for solar stray light rejection, at NRL’s SCOTCH facility. A simulated solar beam was directed at the WFI baffle, as in the NFI test, and the instrument itself was used to measure the radiance of stray light; details are given by Laurent *et al.* (2025). The WFI stray light rejection performance exceeded considerably the stray light rejection performance of the SCOTCH facility, and WFI images of the SCOTCH interior were dominated by interior features rather than by instrumental stray light. Typical dark chamber-interior image points measured a local radiance near

$1 \times 10^{-11} B'_\odot$  (compared to  $B'_\odot$ , the average radiance of the simulated solar beam in the SCOTCH chamber), and differential hit-miss beam measurements afforded sensitivity as low as a few  $\times 10^{-14} B'_\odot$ ; this was not sufficiently sensitive to measure the required FOV-average solar stray light radiance attenuation of  $10^{-16} B'_\odot$  directly. Instead, we used the measured lens stray-light attenuation of  $3 \times 10^{-3}$ , a geometric factor for the apparent size of the solar vane edge “bright line” in the field of view, and differential measurement of the bright line. This yielded calculated overall solar stray light levels of a few  $\times 10^{-18} B'_\odot$ . Given the wide margin on stray light rejection, subsequent WFIIs were not end-to-end tested for stray light performance. In-flight stray light performance was found to meet requirements with wide margin, as expected.

WFI is subject to variable stray light from Earth, near both solstices and especially during the “eclipse season” surrounding the unfavorable (winter) solstice. During the eclipse season, the Earth is in front of WFI, approaching the actual instrument field of view, during passage over the north pole; and stray light increases by up to three orders of magnitude near the baffle in the corners of the image. This contaminates some images each orbit. These periods were considered during mission design and are omitted from the mission total duration count. Details are given in Laurent *et al.* (2025).

Figure 16 shows first light from the WFI-2 instrument, demonstrating low stray light performance and field of view. The limiting magnitude is roughly 11 in a single image: asteroid Iris, with magnitude 10.2, is clearly visible in the original data. The brightest object visible to WFI without saturation is Saiph ( $\kappa$  Orionis, magnitude 2.1), which registers a peak brightness of up to 65,000 digitizer counts (of 65,535 possible) when optimally aligned with the WFI-2 pixel grid.

### 5.3. Camera & onboard data handling

The focal planes are  $2048 \times 2048$  charge-coupled device (CCD) photodetector arrays, made by Teledyne E2V, with  $2048 \times 4096$  total  $15\text{-}\mu\text{m}$  square pixels. The CCDs are operated in quasi-frame-transfer mode: one  $2048 \times 2048$  block of pixels is masked with a metallic cover to form a “storage” area, and the remaining  $2048 \times 2048$  block is left bare (with anti-reflection coating) to form an “active” area. The CCDs are thinned and back-illuminated for quantum efficiency and radiation tolerance; and in operation are cooled to below  $-50$  C. During image acquisition, the CCDs are reset multiple times to clear residual charge, then allowed to accumulate photons during the exposure time. At the end of the exposure, the latent image is transferred to the storage area for slower digitization and readout. Image transfer takes 125 ms; readout requires 3 s. This mode of operation yields extremely stable exposure times, with better than  $10^{-4}$  relative precision, at the cost of requiring each image to be destreaked in post-processing. The CCDs are each operated and read out by a Camera Electronics Box (CEB) from RAL Space. The CEB digitizes the image data to 16 bit depth at a gain value of 4.9 electrons per digitizer count (320k electrons at saturation), then transfers image data over a digital link to the C&DH box for on-board processing and transfer to the ground.

The C&DH processing includes a switchable compression pipeline that enables square-root coding and lossless image compression.

Camera pixels are square-root coded for compression: the digitizer value  $P_{xy}$  of each pixel is multiplied by an integer scale factor  $\alpha$  to a total of up to 32 bits width, then the integer square root of that value,  $(\alpha P_{xy})^{0.5}$ , is recorded instead of  $P_{xy}$ . The square root operation reduces the pixel values back to 16 bit integers, which typically occupy fewer bits of actual dynamic range. The purpose of the square root operation is to match digital transition step size in the final data product, to the variable level of quantum

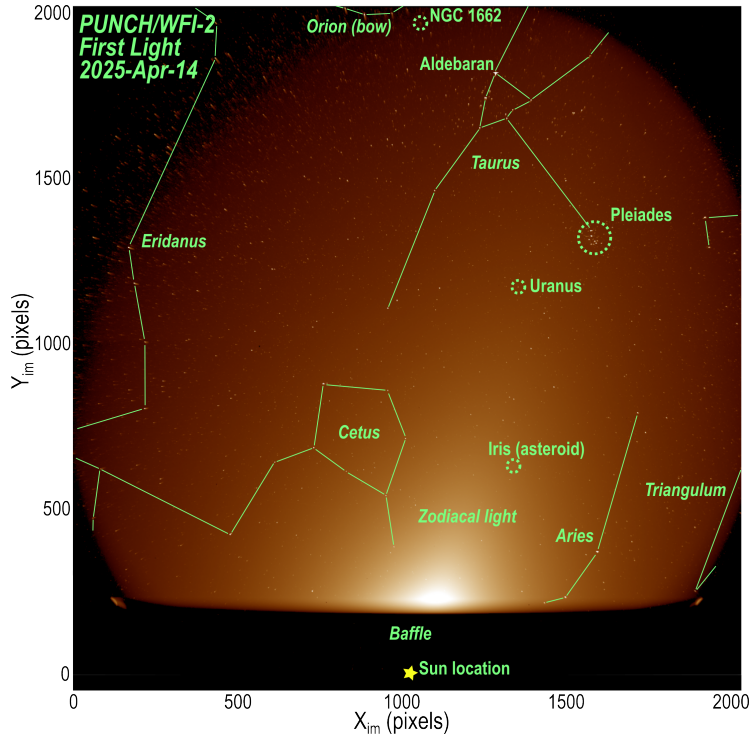


**Figure 16.** First-light image from WFI shows the very large field of view of each WFI camera, spanning over  $40^\circ$  of sky. The dominant source of brightness is the zodiacal light (extended F corona). Several relevant constellations and objects have been marked. Asteroid Iris (magnitude 10.2) is clearly visible in the data, indicating good photometric sensitivity.

shot noise across the dynamic range (DeForest *et al.* 2022). This in turn enables further compression of the remaining bits of each image, by removing useless high-entropy noise while preserving useful and lower-entropy data. In flight,  $\alpha$  was selected to be 16, or  $2^4$ . WFI images, single 16-bit-deep camera frames, thus retain only 10 bits of information (roughly 1,000 unique values) across the range of the digitizer. NFI raw images, being sums of three camera frames, begin as 18-bit integer values occupying 17.5 bits of dynamic range, and conclude with 10.75 bits of dynamic range (roughly 1700 unique values). This setting preserves a small amount of photon noise to dither photometric values, so that digital steps do not dominate the images. This dynamic-range “toeroom” (room to expand at the bottom) is at least 0.7 (RMS) digitizer counts at all brightness levels, and 1.5 (RMS) digitizer counts across most of the dynamic range. The smaller values occur for dark pixels, where the camera digitizer “pedestal” (approximately 400 counts per exposure) is significant compared to the photon signal; and the larger values occur at pixel values above roughly 2,000 counts (or 6,000 counts for NFI sums) where photon counting noise is the most important element of uncertainty in each pixel value.

After square-root coding, image values are compressed on-board with the JPEG-LS lossless image-compression algorithm, applied to values that occupy up to 16 bits of dynamic range. Non-square-rooted PUNCH raw images are observed to compress by a factor of approximately 2.7 with this algorithm. WFI images that have been square-root-coded to a depth of 10 pixels are observed to compress by a further factor of 3.5, for

an overall compression factor of 5.6. Masking out unused pixels (to avoid downlinking read noise and photon noise from those areas) improves overall compression slightly, to an overall factor of 6.0 (1.33 MB/image).

Compressed image data are stored in an on-board flash RAM unit and downlinked during ground passes.

#### 5.4. Polarizing filter wheel

Each PUNCH imager uses a polarizing filter wheel (PFW) to measure the linear polarization of light across the image plane. Each polarizing filter wheel intersects the main optical beam and has five positions, containing: three linear polarizers oriented at  $-60^\circ$ ,  $0^\circ$ , and  $+60^\circ$  relative to the instrument “horizontal” axis (aligned with spacecraft  $\pm Y$ ); a non-polarizing “clear” optical flat; and a “dark” opaque metal sheet. Three polarizers were chosen following historical usage (e.g., Howard *et al.* 2008); the nuances of the tri-polarizer formulation are described by DeForest, Seaton, and West (2022). Each filter wheel is actuated by a stepper motor, commanded directly by the C&DH electronics; its position is reported by redundant parallel resolvers and downlinked in the engineering/housekeeping telemetry channel.

The NFI filter wheel is mounted between the lens barrel assembly and the camera. The WFI filter wheel is mounted in front of the optical lens assembly, in the empty space between the leading lens and the external pupil. The position in WFI was chosen to better regulate polarization over the very wide field of view and fast optical beam. The WFI filter wheels are mounted in the reverse direction to the NFI filter wheel: NFI mounts the motor on the  $+X$  (sunward) side of the filter wheel, while WFI mounts it on the  $-X$  (camera) side of the filter wheel. This means that the polarizer positions are reversed between the two instruments, a nuance that is managed on the ground by the Science Operations Center (SOC) pipeline during data product assembly.

#### 5.5. Student Thermal Energetic Activity Module

The PUNCH/NFI spacecraft hosts a student-contributed do-no-harm class instrument, the Student Thermal Energetic Activity Module (STEAM). STEAM was conceived as a dual band X-ray full-sun spectrometer, implemented using solid state detectors and off-the-shelf electronics. The STEAM project is described by Hanson (2025). STEAM comprises two integrated solid-state X-ray spectrometers (off-the-shelf X123 units) supplied by Amptek, together with control electronics designed, assembled, and integrated by undergraduate students at the University of Colorado. STEAM was an educational success, helping provide hands-on experience for over 50 students across its five-year development program. The STEAM instrument suffered an anomaly during Observatory level thermal vacuum testing, and is permanently switched off.

### 6. Data products and Ground Pipeline

PUNCH has an open data policy: all scientific data are released to everyone simultaneously, with no restrictions on use. Scientists and others making use of the data are *requested* to acknowledge the PUNCH mission with the statement “PUNCH is a heliophysics mission to study the corona, solar wind, and space weather as an integrated system, and is part of NASA’s Explorers program (Contract 80GSFC14C0014)” and to report their usage to the Project Scientist (S.E.G.) for impact tracking.

PUNCH data are archived and distributed via NASA’s Solar Data Analysis Center (SDAC; Ireland *et al.* 2022), and may be retrieved directly from the SDAC file system or via the Virtual Solar Observatory (VSO; Hill *et al.* 2009). During mission operations, current information and links to relevant analysis software, documentation, and team contact information may be found at the PUNCH mission website “<https://punch.space.swri.edu>”.

PUNCH data products are generated in the Science Operations Center (SOC), which is described in detail by Hughes *et al.* (2025) and summarized here. Data are produced as FITS files (Wells, Greisen, and Harten 1981) in four principal processing Levels, numbered from 0 through 3. Background subtraction is the driving challenge for PUNCH data reduction, and drives precision of all levels of data reduction.

Level 0 data are direct from each spacecraft, unpacked from the downlinked CCSDS packet stream and delivered as integer files in digitizer units. Level 1 data are photometrically and astrometrically calibrated but remain associated with individual downlinked images. Level 2 data are resampled into a common coordinate system and merged across spacecraft into mosaic images, as if from a single instrument. Level 3 data are background-subtracted and ready for scientific analysis of the K corona and solar wind.

In addition to the primary numbered data levels, the SOC produces both QuickLook (“Level L”) images, in conventional display formats; and low-latency QuickPUNCH (“Level Q”) data suitable for forecasting, as FITS files. Level Q products, and the utility of PUNCH for space weather forecasting, are described in detail by Seaton *et al.* (2025).

Data products are identified by their level number, a three-character code, and a timestamp; and the PUNCH data repositories are organized as a hierarchical data structure by those identifiers in that order. In the following subsections we describe the numbered reduction levels and the principal data product codes of interest to the community.

PUNCH FITS files have more structure than simple images. FITS supports multiple header-data units (HDUs) per file. The zeroth (HDU 0) contains information about tile compression used in subsequent images in each file. The first (HDU 1) contains the image data, which may be two-dimensional or, in polarized data products, three-dimensional. The second (HDU 2) contains an uncertainty array, representing the uncertainty in the primary data product.

Detailed contents of the data and metadata, and mission-supplied analysis tools to read and manipulate them, are described by Hughes *et al.* (2025) and by the online mission documentation.

The L3 data products are designed to be the primary data used to address the science topics outlined in Section 2 and close the mission’s science objectives. However, data products at L0, L1, and L2 are also archived and distributed to support reproducibility of PUNCH data analysis, and to enable additional science (Section 7).

### 6.1. Level 0 data

PUNCH Level 0 data files are produced rapidly, typically within less than an hour of receipt at the SOC. Each data file has a two-letter code indicating the type of exposure, followed by a single digit indicating which PUNCH Observatory produced the file (Table 4). Data from the WFI Observatories are numbered 1-3, and data from PUNCH-NFI00 is numbered 4. The codes CR, PM, PZ, and PP correspond, respectively, to clear, Minus, Zero, and Plus polarizer positions (Section 5.4) and are produced by the normal science campaign. The other codes are relevant to calibration activities.

**Table 4.** PUNCH primary Level 0 & Level 1 product codes. All these codes represent  $2048 \times 2048$  pixel single image files, organized by polarizer position and Observatory.

Code	Definition
CR $n$	Clear exposure (no polarizer)
PM $n$	Linearly polarized Minus ( $-60^\circ$ ) exposure
PZ $n$	Linearly polarized Zero ( $0^\circ$ ; horizontal) exposure
PP $n$	Linearly polarized Plus ( $+60^\circ$ ) exposure
DK $n$	Dark exposure (for calibration)
PX $n$	Nonstandard or unknown PFW position (calibration or error)

Level 0 pixels have integer values from the camera digitizer and are neither calibrated nor flat-fielded in any way, so (for example) they include digitizer pedestal, exposure streaking, and all other camera and optical artifacts. They are typically square-root compressed: if the header field “ISSQRT” is boolean-true, then the values in the file represent the scaled square root of the value from the digitizer; in that case, camera pixel values  $P_{cam}(x, y)$  may be calculated by squaring each image pixel value then dividing by the header field “SCALE”. The images have fixed geometry relative to the instrument, with CCD “columns” running in the horizontal direction in each image. The cameras use dual digitizers so that two different pedestal values and gain curves apply in the top and bottom half of each image.

The images are masked on-board each spacecraft, to eliminate unused pixels outside the FOV of the camera, reducing downlink volume. NFI and all three WFIs include slightly more active pixels than required. Unused/masked pixels have value 0, which is not a possible value for a valid pixel because of the digitizer pedestal of roughly 400 counts.

Level 0 headers are assembled from engineering data and science metadata from the spacecraft. Pointing information is stored using the World Coordinate System (WCS); at this stage, it is “roughed-in” to few-pixel precision based on a priori knowledge of the instrument geometry and the spacecraft-reported pointing information. No uncertainty layer is present at Level 0.

## 6.2. Level 1 data

PUNCH Level 1 data files are also produced rapidly, within hours of receipt by the SOC. They remain organized by spacecraft, and retain the one-to-one relationship between in-space camera images and ground data products. Each data file has a two-letter code indicating the type of exposure, followed by a single digit indicating which PUNCH Observatory produced the file. The main data products use the same codes as Level 0 (Table 4).

Level 1 pixels have floating-point values that are intended to capture photometric values on the sky, but are still individual exposures from particular Observatories through particular polarizers. The Level 0 to Level 1 steps include: improved square-root decoding (DeForest *et al.* 2022); destreaking to account for quasi-frame-transfer streaks in camera operation; quartic-polynomial flat-field correction including both detector effects and optical vignetting; cosmic ray and saturated-pixel detection and removal; pointing and distortion-function correction using the starfield; and point-spread function (PSF) regularization (Hughes *et al.* 2025). The pixel values are calibrated in

$B_{\odot}$  units (using the mean photospheric radiance of  $7.58 \times 10^6 \text{ W m}^{-2} \text{ SR}^{-1}$ , adjusted to the passband of PUNCH).

Stray light in the instruments is removed at Level 1. Stray light is removed from each of the polarized (or unpolarized) channels (M,Z,P,C) separately, in four separate data streams per instrument.

Solar stray light from the instruments is quasi-stationary in the instrument reference frame (changing month to month due to eccentricity of Earth's orbit) and is removed at Level 1, using the minimum-value-over-time method with analytic correction for the statistical bias introduced by minimum-value sampling. Because of the eccentricity of Earth's orbit, the Sun's apparent size (and therefore total intensity) change slowly over the course of the year, and therefore a posteriori instrument stray light models are regenerated every few days and linearly extrapolated to the time of current data. These stray light models necessarily include quasi-stationary, circularly symmetric elements of the F and K corona, in addition to instrumental stray light.

The NFI instrument was observed during commissioning to be subject to variable stray light patterns from earthshine illuminating the interior of the instrument. The patterns are dominated by earthlight scattering off an interior tube baffle vane and illuminating the rear of the occulter. Glint from the circular rim at the rear of the occulter then enters the A1 aperture, producing large and variable stray light patterns that cannot be treated as quasi-stationary. This effect is removed on the basis of spatial structure and spatiotemporal variability, using linear transformations and sparse matrix inversion. The NFI-specific removal algorithm and module were a subject of rapid development early in the operational phase of the mission, and are detailed by Hughes *et al.* (2025).

PSF regularization is tuned to produce an absolutely uniform PSF on the celestial sphere: the target PSF in the instrument plane is set to match the measured distortion function of each instrument, so that (for example) deprojecting any given stellar neighborhood to a locally-flat projection of the celestial sphere will yield the same PSF regardless of position in the L1 image. This means that careful analysis will show slightly different PSF values across each instrument's focal plane, reflecting the optical projection of the celestial sphere onto the flat CCD.

Level 1 images are not resampled from the original camera pixels, but World Coordinate System (WCS; Calabretta and Greisen 2002) coordinates, including distortion parameters, are updated using the starfield in each image; alignment precision is under 10 arcsec RMS, well below the pixel size.

HDU2 of the L1 FITS files is populated with images containing photometric uncertainty information for the corresponding HDU1 pixels, based on a priori photon noise estimation with correction to account for subsequent steps. This uncertainty value is also propagated and updated through subsequent processing levels.

### 6.3. Level 2 data

PUNCH Level 2 data files are typically produced within 1-3 days of receipt of the first data at the SOC; this is limited by the need to accumulate all relevant data from all four spacecraft, for each output image. The data are merged across spacecraft and across polarizers, and rectified to orient projected solar north with up on the image plane. They retain the one-to-one temporal association between data product acquisition and individual data products, but lose the identity of individual camera frames or spacecraft. For example, one polarized acquisition sequence on-orbit results in twelve individual images (three from each of four spacecraft) that are merged into

a single polarized mosaic. Each data file has a three-letter code indicating the type of data product (Table 5).

The mosaics are reprojected into the Sun-centered azimuthal equidistant projection, so that radius on the image plane is proportional to the solar elongation angle  $\varepsilon$  (Appendix A.1). The mosaic pixel scale was chosen as a compromise between representing the 90° field at full resolution and the need to retain data products at a manageable size. The mosaics support a spatial resolution of approximately 3 arcmin, at a plate scale of 1.3 arcmin/pixel.

Because NFI offers higher resolution (approximately 1.5 arcmin), a separate full-resolution NFI data product is offered at  $2048 \times 2048$  resolution. NFI full-resolution L2 products are resampled into the Sun-centered gnomonic (“tangent plane”) projection often called “solar observing coordinates”, so that radius on the image plane is proportional to  $\tan(\varepsilon)$ . The difference in projection is to improve compatibility between NFI data and the legacy data from SOHO/LASCO (Brueckner *et al.* 1995), while also working in a useful standard projection for the wide PUNCH FOV. The difference between the two projections amounts to a 1-NFI-pixel offset at  $16 R_\odot$ , or up to 7 NFI pixels (two mosaic pixels) at the outer edge of the NFI field of view; this is trivial for many applications but significant for PUNCH, which must co-align starfield images to roughly 10 arcsec (RMS) to achieve starfield subtraction.

The polarized data products are typically 3-D “cubes” of size  $w \times h \times 3$ , with  $w$  being the image width,  $h$  being the image height, and the third dimension running across MZP<sup>6</sup> virtual-polarizer triplet images (Appendix A.2), while the unpolarized/clear data products are typically 2-D  $w \times h$  images. The MZP virtual polarizer angles are measured relative to the system in which solar north is up; the system is described by DeForest, Seaton, and West (2022) and developed in more detail by Patel, Seaton, and DeForest (2025).

Level 2 PUNCH data include uncertainty information in HDU 2 of the FITS file. The uncertainty layer is used both to track signal to noise ratio (SNR) and also to mark bad pixels, including cosmic ray hits, known detector defects, and objects such as the high altitude aurora and other satellites.

**Table 5.** PUNCH Level 2 data product codes

Code	Shape	Description
PTM	$4096 \times 4096 \times 3$	Polarized trefoil science mosaic (MZP)
PNN	$2048 \times 2048 \times 3$	Polarized NFI full-resolution image (MZP)
CTM	$4096 \times 4096$	Clear (no polarizer) trefoil science mosaic
CNN	$2048 \times 2048$	Clear (no polarizer) NFI full-resolution image

#### 6.4. Level 3 data

PUNCH Level 3 data files comprise scientific image files and extracted solar-wind velocity maps. The image files are background-subtracted. Latency is typically 14 days from receipt of the data by the SOC; this is limited by the need to accumulate long-baseline datasets for the background subtraction. Image products are named with a leading “P” (Polarized) or “C” (Clear). These images are produced in full-cadence and

<sup>6</sup>for Minus, Zero, Plus [60°] polarizer angle relative to a reference angle

low-noise forms. The full-cadence products are marked with either “T” (for Trefoil) or “N” (for NFI), and are produced at the full observing cadence for that type of image: 4 minutes for P types and 8 minutes for C types. Low noise products are named with “A” (for Average) and consist of 32-minute averages (across four 8-minute observing holds each). Velocity maps are produced via the delayed-autocorrelation method (Attié *et al.* 2025) and are named “VAM”.

**Table 6.** PUNCH Level 3 data product codes

Code	Shape	Description
PTM	$4096 \times 4096 \times 2$	Polarized K-only trefoil science mosaic (B, $\perp pB$ )
PNN	$2048 \times 2048 \times 2$	Polarized K-only NFI full-resolution image (B, $\perp pB$ )
PAM	$4096 \times 4096 \times 2$	Polarized K-only averaged (low-noise) mosaic (B, $\perp pB$ )
PAN	$2048 \times 2048 \times 2$	Polarized K-only averaged (low-noise) NFI image (B, $\perp pB$ )
CTM	$4096 \times 4096$	Clear (no polarizer) K-only trefoil mosaic
CNN	$2048 \times 2048$	Clear (no polarizer) K-only NFI full-resolution image
CAM	$4096 \times 4096$	Clear (no polarizer) K-only averaged (low-noise) mosaic
CAN	$2048 \times 2048$	Clear (no polarizer) K-only averaged (low-noise) NFI image
VAM	$720 \times 8$	Velocity map at 8 altitudes, derived from mosaic correlation

Figure 10 illustrates the fundamental challenge of background subtraction for all heliospheric imagers including PUNCH: the F corona (zodiacal light) and starfield dominate over the signal by 2-3 orders of magnitude in the far field. PUNCH uses the same six-step process for background subtraction as was developed for STEREO/HI (DeForest, Howard, and Tappin 2011; DeForest *et al.* 2016), with the advantage of additional lessons learned from that mission, and also the challenge of using spliced mosaic images rather than single exposures from one optical system. The process is summarized here and detailed by Hughes *et al.* (2025).

PUNCH background subtraction requires separate treatment of three steady backgrounds. They are all separated on the basis of stationarity in a particular reference frame.

The first background is steady solar stray light, which is removed at Level 1 (and described in Section 6.2). The other two are removed at Level 3.

The second background is the F corona (zodiacal light), which is quasi-stationary in the heliocentric reference frame and is removed on the basis of a running-minimum fit, corrected for variable noise level effects, in the Level 2 data. Each pixel location in the mosaic frame is fit with a running-minimum polynomial background estimator; these polynomials are conditioned to produce daily F corona models, which are interpolated to provide an F background for each data product, and subtracted in the L3 pipeline. This method makes use of the observed approximate symmetry of the heliospheric dust cloud; it is expected that any dynamic features such as a dust enhancement near Venus (e.g., Jones, Bewsher, and Brown 2017; Stenborg *et al.* 2021a) or local dust depletions (Stenborg *et al.* 2021b) will be recognizable as their dynamics follow Keplerian orbital time scales of months, rather than solar wind time scales of days, and may be removed on that basis.

The third background is the stellar background, which is stationary in the celestial reference frame. L2 data products, with the F corona removed, are resampled to celestial coordinates for an interval, nominally  $\pm 2$  weeks, around each day, and a minimum value fit is applied to produce a daily celestial background – which is then interpolated and resampled to match each L2 mosaic, then subtracted from the

data themselves. This removes stationary celestial objects, is enabled by photometric adaptive-filter resampling (DeForest 2004), and requires careful treatment of the PSF as each resampling operation slightly blurs the data. Non-stationary celestial objects include the major planets and the Moon, which are identified by pixel saturation and marked using the uncertainty layer; and comets and asteroids. Asteroids at or below 12th magnitude, of which there are roughly  $10^4$  (Bottke *et al.* 2020), are below the noise floor in a single PUNCH/WFI image and do not significantly affect PUNCH science. Considered as a long-exposure detecting telescope for asteroids or comets, PUNCH has a limiting magnitude of approximately 18 when 60 days of images are combined coherently.

The very brightest celestial objects – stars, the Moon, and bright planets – saturate the CCD and invalidate pixels both in the vicinity of the PSF-correction neighborhood around the object, and also over the locus of associated CCD charge-bleeding (which produces saturated streak artifacts along the readout direction); this affects approximately 0.02% to 0.5% of pixels in each mosaic depending on the time of year and lunar phase. The WFI exposure time is adjusted to balance between preserving the faint end of the dynamic range, and saturating the brightest objects in the sky. Therefore objects of magnitude 2.0 or brighter saturate the detector in the nominal observing sequence. There are roughly 65 celestial objects (including the Moon and the bright planets) that saturate WFI images; the star Saiph ( $\kappa$  Orionis, Orion's right knee directly “below” Betelgeuse, visual magnitude 2.09) is the brightest celestial object that does not saturate WFI clear exposures. Saturated streaks from bright objects rotate with the spacecraft and therefore do not impact any particular piece of dark sky for more than one 8-minute observing window at a time.

Following DeForest, Howard, and Tappin (2011), a final step of Fourier filtering is applied to clean the L3 data via motion filtering. The motion-filtering step for PUNCH is sufficiently broad to pass SIRs and other caustic structures that may move  $3\times$ – $5\times$  slower than solar wind itself.

PUNCH background subtraction is complicated by the fact that every image is polarized, as are all of the backgrounds: starfield, F corona, and instrumental stray light. The three polarization channels are treated with individual background processes and models (eight in all: four for the mosaics and four for the NFI full-resolution products). Using virtual polarizer channels, rather than pB or Stokes parameters, allows re-using baseline-estimation methods already adopted for unpolarized brightness images: each virtual polarizer channel represents an actual filtered radiance, from which a background may be estimated using conventional minimum-value methods. Each step of background subtraction is resolved not only in spatial coordinates (in the instrument, solar, and celestial frames), but also in polarization angle, by mathematical transformation of the virtual polarizer triplets. The method is described in detail by Hughes *et al.* (2025).

## 7. Additional science

PUNCH was specifically designed to meet the requirements in Section 3 and thereby fulfill the science described in Section 2. PUNCH observations are also suitable for addressing additional science topics in astrophysics, planetary science, and geospace science. Here we discuss the relevance of PUNCH observations to several topics unrelated to the PUNCH primary science objectives: stellar polarimetry, asteroid observations (particularly NEOs and possible vulcanoids), interplanetary dust observations, and geospace observations of high-altitude aurora.

### 7.1. Stellar polarimetric observations

As a byproduct of Level 3 background subtraction, PUNCH data include a comprehensive polarized map of the sky at all ecliptic latitudes out to  $\pm 45^\circ$  from the ecliptic, with  $< 0.1\%$  polarimetric precision. Stars are observed to be polarized (Hiltner 1949; Hall 1949) and these observations and the physics are nicely reviewed by Clarke (2009) and by Trippe (2014). The effect is troublesome for the primary PUNCH science as it requires precise polarimetric characterization of the entire visible celestial sphere. These polarimetric data contain useful information for understanding stars and the galactic magnetic field, supplementing the many important telescopic surveys that exist (e.g., Mathewson and Ford 1970; Hsu and Breger 1982; Heiles 2000; Fossati *et al.* 2007; Versteeg *et al.* 2023; Angarita *et al.* 2023).

The bulk of the stellar linear polarization signal is not due to intrinsic polarization of emitted starlight, but to aspherical grains interacting with the light as it propagates: either in interstellar space (Versteeg *et al.* 2023) or (less commonly) in local dust clouds (Poeckert, Bastien, and Landstreet 1979). The polarization of starlight by interstellar dust is interesting in part because it is a measure of the direction and strength of the interstellar magnetic field (Versteeg *et al.* 2023), and of turbulence in the interstellar medium (Angarita *et al.* 2024).

Compared to contemporary surveys, PUNCH is both more comprehensive and more limited by spatial resolution. At the nominal 3 arcmin resolution of mosaic data, crowding places the limiting apparent magnitude at roughly 14: although PUNCH can detect fainter stars photometrically, there are only roughly  $10^7$  resolution elements in the entire 9-steradian effective field of view, matching the number of magnitude 14 objects in the same field. PUNCH can therefore isolate most stars only at about magnitude 12 or brighter, although it is capable of “crowded-field polarimetry” of much fainter objects.

### 7.2. Asteroid and comet observations

Recent asteroid surveys from ground-based telescopes have identified a handful of asteroids on orbits entirely within the orbit of Earth or Venus (e.g. Bolin *et al.* (2022); Sheppard *et al.* (2022)). These are notable discoveries because the nature of these asteroids’ orbits only permit their observation from the Earth when they have a very low solar elongation, which is impossible for some telescopes or only accessible for short time windows each night for others. However, models for the population of near-Earth objects predict a sizable population of objects in this region of the solar system (Figure 17), including 5-10 as of yet undiscovered asteroids larger than 1 km (Nesvorný *et al.* 2023; Deienno *et al.* 2025).

PUNCH observes continuously in a part of the sky that is historically difficult: areas with low solar elongation. Many of the objects predicted to populate this region are always in the PUNCH FOV. The ability for PUNCH to discover, track and characterize asteroids and comets depends on the trade between its relatively small imaging aperture, its large field of view and its rapid and constant imaging cadence. There is precedent for observing asteroids and comets with SOHO and STEREO (Knight *et al.* 2010; Li and Jewitt 2013), and the larger field of view, smaller pixels and lack of on-board image stacking may permit PUNCH to be a more effective tool for characterization and for discovering new objects.

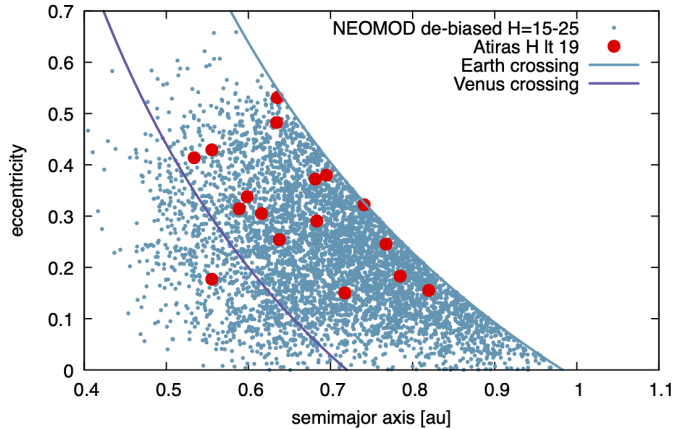


**Figure 17.** PUNCH should be able to detect many Earth-crossing or sub-Earth objects in solar orbit, as seen in this scatterplot of orbital characteristics of predicted and observed objects in the solar system. Blue points indicate objects in the predicted population, with orbits entirely within 1 AU from the Sun (NEOMOD solar system model; Deienno *et al.* 2025), which should be detectable by PUNCH. Red circles indicate known objects in this region with absolute magnitude brighter than 19. The blue line indicates orbital properties that lead to an Earth-crossing orbit, and the purple line is the same for Venus. The only red dot to the left of the Venus-crossing line is the only known asteroid whose orbit is entirely inside that of Venus (Bolin *et al.* 2022).

### 7.3. Solar system dust observations

PUNCH is well placed to make significant contributions toward understanding the zodiacal dust cloud (ZDC). Recent coronagraph observations from the STEREO and PSP missions have shown that the photospheric light scattered by the ZDC exhibits small variations that need further definition. This scattered light is referred to as the “zodiacal light” or “F corona” (Schuerman and Weinberg 1983). With its complete 360° coverage out to 45° from the Sun, PUNCH is able to measure the brightness and polarization of the F-corona with greatly increased sensitivity and coverage compared to prior observations.

Measurements of the polarization of zodiacal light are scarce for the regions observed by PUNCH. Koutchmy and Lamy (1985) reported on the status of contemporary and earlier observations of F-corona polarization. They revealed a discrepancy in contemporary observations of the high corona between  $7 R_{\odot}$  and  $15 R_{\odot}$ . No polarization measurements had ever been reported between elongations of roughly 4° and 45° although very wide angles were covered by the Teide observatory (Dumont and Sanchez 1976). No newer survey measurements have covered this missing area; the polarization profile of the inner zodiacal cloud (throughout the PUNCH field of view) remains unknown.

The orbits of the dust in the ZDC are affected by the gravitational influences exerted by the solar system planets. The center of mass of the solar system (the barycenter) is in constant motion around the Sun, varying in longitude, latitude and radius from the Sun. The barycenter’s distance variation, in particular, creates an asymmetry in the distribution of the inner ZDC, and a corresponding asymmetry in the appearance of the zodiacal light; this asymmetry has been observed (Stenborg *et al.* 2024) with the PSP/WISPR instrument. With its 360° coverage, PUNCH will be able to determine

whether any north-south asymmetry exists, and the extent and evolution of the east-west asymmetry.

Finally, with its increased sensitivity, PUNCH will likely be able to detect subtle brightness increases due to, for example, asteroids or comets entering the inner heliosphere as well the impact of interstellar dust increasing the brightness in a range of ecliptic longitudes centered at  $259^\circ$ , due to the solar system traveling through the galaxy. The range of longitudes could be as high as  $180^\circ$  (full-width), but the increase would be highest at the central longitude. Additional searches include finding the dust depletion zone, which begins at  $35 R_\odot$  and peaks at  $25 R_\odot$  (Stenborg *et al.* 2021b), or even if there are additional sublimation zones beyond  $35 R_\odot$ ; and characterizing and understanding dust depletions behind CMEs as have been seen with WISPR (Stenborg *et al.* 2023), or associated with other plasma structures such as SIRs.

#### 7.4. Aurora and airglow observations

PUNCH may contribute significantly to geospace studies through novel observations of upper atmospheric luminous phenomena, notably the aurora and airglow.

At Earth, the aurora is a persistent phenomenon, and a strong diagnostic of space weather near Earth. As energetic electrons and protons interact with the neutral atmosphere, ionization and excitation processes occur. The basic mechanism is well understood. Electrons precipitate along magnetic field lines into the ionosphere, where they collide with atmospheric particles, exciting them and releasing photons as “electron aurora” (e.g., Rees 1963). Protons also undergo charge-exchange collisions with atmospheric particles, creating excited hydrogen atoms that emit characteristic “proton aurora” (e.g., McIlwain 1960).

Most auroral emission occurs from 100 to 400 km altitude; the specific altitude serves as a proxy for the energy of precipitating particles and provides key insights into magnetosphere-ionosphere coupling (e.g., Kaila 1989). Discrete green-line aurora typically occurs below 150km, and red-line aurora produced by atomic oxygen is seen up to 400km. The Solar Mass Ejection Imager (SMEI; Eyles *et al.* 2003) serendipitously detected luminous phenomena at altitudes  $\geq 840$  km over the auroral zones and polar caps (Mizuno *et al.* 2005). To date, the SMEI result remains the only report of this “high-altitude aurora”, which has never been systematically characterized or investigated in detail. As a result, its energy source, particle population, and underlying physical mechanism are poorly understood. Informed by the SMEI result, PUNCH was designed specifically to mitigate the effects of high-altitude aurora for heliospheric imaging; but Level 1 data include hypothetical effects of high-altitude aurora and other high-altitude luminous phenomena including airglow, affording a unique opportunity to investigate these effects systematically and understand a novel and as-yet unexplored phenomenon of the magnetosphere.

Other optical emissions in the upper atmosphere, collectively known as airglow, are produced by chemical reactions between solar radiation and atmospheric constituents (e.g., Silverman 1970). Unlike aurora, airglow is continuously present and occurs at discrete wavelengths throughout the spectrum. PUNCH observes airglow emissions from a novel vantage point, offering a new probe of the morphology, potential dynamics, and altitude of the quasi-steady airglow emission.

### 8. Conclusions

PUNCH addresses large-scale and meso-scale science of the solar wind and corona, with a larger field of view and deeper sensitivity than have been possible with prior

missions. The mission builds on capabilities proven through earlier iterations of similar instruments and observing concepts; these capabilities are supported by a novel mission design that enables a science of unification, viewing the solar corona and inner heliosphere as a single unified system, within its celestial context on the sky.

The unique challenges of wide-angle heliospheric imaging drive a unified view of the mission itself, considering the post-processing pipeline as a critical element of the instrument suite. The rigor required in merging and calibrating the PUNCH images well enough to support its primary science make PUNCH a useful observatory for astronomical, planetary, and geophysical topics well beyond its primary mission science.

**Acknowledgements** PUNCH is the result of a very large scientific and technical community working together over a decade, combining outstanding talent across many fields and heroic effort through many types of adversity. The hundreds of individuals, whose dedication and willing support brought PUNCH to fruition, span four continents and dozens of institutions. PUNCH builds on the major achievements of prior missions, including PSP/WISPR, STEREO/SECCHI, Coriolis/SMEI, SOHO/LASCO, and the Helios three-channel photometer.

PUNCH owes much of its overall design and scientific concept to early efforts by T.A. Howard, whose work was instrumental in co-developing and exploiting methods for deep background-subtraction of heliospheric images; in predicting and promoting the possibility of wide-field 3-D analysis via polarization; and in helping demonstrate the feasibility of heliospheric imaging from below the Van Allen belts.

We particularly acknowledge Tele Vue Optics and remember their founder, Al Nagler (1935-2025), for designing and supplying the optics for the Wide Field Imagers, working well outside Tele Vue’s “comfort zone” of eyepiece design, and stepping up to produce a very compact, achromatic, space-qualified system with very low distortion, several important stray-light reducing features, and excellent focus over a very wide field of view. PUNCH/WFI is but one of Al Nagler’s many contributions to the astronomy, spaceflight, and scientific communities, and he is both sorely missed and fondly remembered.

We also gratefully acknowledge C. Eyles for early consultation on heliospheric imager design based on his experience with SMEI; the SwRI Internal Research program for much early support that led to the successful PUNCH proposal; J. Burch for consultation and institutional support throughout the project; and J. Andrews for invaluable advice on project management.

J.B., S.F., S.E.G., and A.M. acknowledge support of the National Center for Atmospheric Research, a major facility sponsored by the National Science Foundation under Cooperative Agreement No. 1852977. D.J.M. acknowledges support from the IMAP mission as a part of NASA’s STP mission line (80GSFC19C0027).

PUNCH is a heliophysics mission to study the corona, solar wind, and space weather as an integrated system, and is part of NASA’s Explorers program (Contract 80GSFC14C0014). ■

## Appendix

### A. Nomenclature: Geometric and Photometric Quantities

Analysis of PUNCH polarimetric wide-field images makes use of different geometry than has been typical for solar remote sensing missions; and polarimetric imaging of distributed objects requires a specialized vocabulary. In the interest of coordinating across analyses of PUNCH data, we define here a “PUNCH standard” nomenclature

**Table 7.** Glossary of PUNCH nomenclature for geometric and photometric analyses

Coordinate axes and distances	
RTN coords	Radial/Tangential/Normal coordinates (Burlaga 1984)
X axis	Direction from Sun center toward observer
Y axis	Cross product of X and solar north (projected solar west)
Z axis	Perpendicular to X and Y (projected solar north)
Plane of Sky	YZ plane
r	3-D distance from Sun center to a scattering point
$\mathbf{r}_{pos}$	2-D distance from Sun center to a line of sight, in the YZ plane
$\mathbf{r}_{obs}$	Distance from Sun center to Observer (along X axis)
s	Distance toward the observer from the Thomson surface
$\ell$	Distance from the observer, along a given line of sight
$X_{im}, Y_{im}$	Image-plane coords: $X_{im}$ horizontal, $Y_{im}$ vertical, origin: lower left
$r_{\odot}$	Actual solar radius (696,340 km)
Relevant angles	
$R_{\odot}$	Convenience unit: $0.25^{\circ}$ (approx. apparent solar radius from 1 AU)
$\varepsilon$	Elongation angle from Sun: apparent distance from Sun center
$\alpha$	Solar “azimuth” (position angle), CCW about X from Z
$\chi$	Scattering angle ( $\chi = 0$ implies no scatter)
$\chi'$	Supplement to $\chi$ (interior to the scattering triangle)
$\tau$	Complement to $\chi$ (Thomson angle as in Fig. 18)
$\xi$	Out-of-sky-plane angle ( $\xi = \varepsilon + \tau$ )
$\psi$	Complement to $\xi$ (forms scattering triangle, with $\chi'$ and $\varepsilon$ )
Photometric quantities	
$B_{\odot}$	Mean solar photospheric radiance (units of $\text{W m}^{-2} \text{sr}^{-2}$ )
$I_{\odot}$	Total solar intensity (units of $\text{W m}^{-2}$ )
$I$	Stokes parameter (total intensity or radiance; clarify when used)
$Q$	Stokes linear-polarization parameter (vert. - horiz.)
$U$	Stokes linear-polarization parameter (diagonal)
$tB$	“total brightness”: Stokes $I$ radiance (also $B$ , deprecated)
$B_R, B_T$	Radiance through a radially or tangentially oriented polarizer
$B_M, B_Z, B_P$	Radiance through a polarizer at $-60^{\circ}$ , $0^{\circ}$ , or $+60^{\circ}$ orientation
$B_C$	Radiance through no polarizer (“clear”); similar to $tB$
$pB$	“tangential polarized brightness”: $B_T - B_R$ (also ${}^{\perp}pB$ )
$pB'$	“alt polarized brightness”: Stokes-like parameter, conjugate to $pB$
$L$	total linear polarized brightness $\sqrt{Q^2 + U^2}$ (also ${}^{\circ}pB$ )
$p$	“Degree of [tangential linear] polarization” ( $pB/tB$ )
$PR$	“Polarization ratio” $B_R/B_T = (1 - p)/(1 + p)$

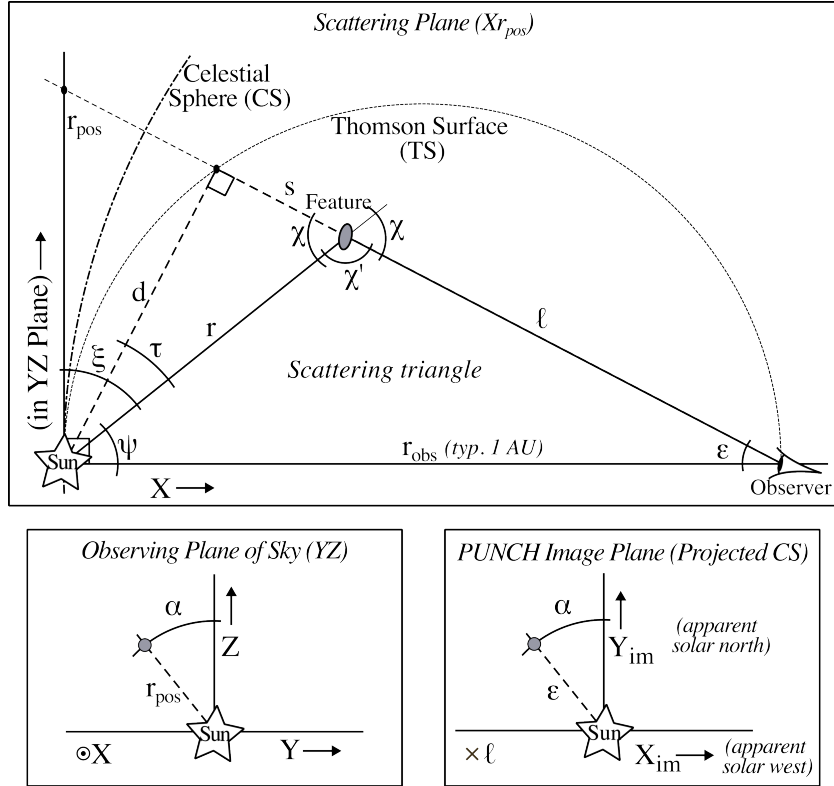


**Figure 18.** Diagrams and standardized symbols for PUNCH observations show many of the relevant quantities and constructions used for PUNCH analysis. PUNCH mosaic images are delivered as azimuthal equidistant (AZP) projections of the celestial sphere (CS), such that the Sun is at the coordinate origin (at the center of the pixel grid), apparent solar north (projected Z) is in the  $Y_{im}$  direction, and coordinate radius in the  $(X_{im}, Y_{im})$  plane is equal to the elongation angle  $\varepsilon$ .

for geometric (Section A.1) and photometric/polarimetric (Section A.2) terms thought to be of interest for all PUNCH analyses. Table 7 is a glossary of these terms.

### A.1. Geometric definitions

Distances, coordinates, and angles relevant to PUNCH observations are drawn in Figure 18.

The lower right panel of Figure 18 shows the image plane used for PUNCH mosaic image products. For normal L2 and higher science data products from PUNCH, the  $X_{im}$  and  $Y_{im}$  axes of the image plane correspond to observer's “solar west” and “solar north” respectively. Mosaic products are in the azimuthal equidistant projection, so that radial distance from the center of the image is directly proportional to the elongation angle  $\varepsilon$ , also called the “apparent distance” between the feature the Sun. Likewise, “azimuth” ( $\alpha$  angle) on the image, measured counterclockwise from solar north (the  $Y_{im}$  direction), corresponds to solar position angle on the sky. (Full-resolution NFI images are delivered in the gnomonic projection, to better match the projection used by prior instruments

such as SOHO/LASCO. For this projection, radius on the image plane is proportional to  $\tan(\varepsilon)$  rather than  $\varepsilon$  itself.)

The top panel of Figure 18 shows a cross-section of the three-dimensional geometry of the system. The “scattering triangle” formed by a particular small feature, the Sun, and PUNCH itself defines a plane, the “scattering plane”, in three dimensions; this plane projects to a radial line in the image plane (the dashed line in the lower right panel of Figure 18).

For analysis in Cartesian coordinates, we adopt the familiar RTN Cartesian system defined by Burlaga (1984). In this system the X axis extends from the Sun to the observer; the Y axis extends in the direction of the cross product of solar north with X (“solar west”); and the Z axis extends in the mutually perpendicular direction (“projected solar north”), to form a right-handed coordinate system. In RTN coordinates the YZ plane, shown in the lower left panel of Figure 18, is the “plane of the sky”, also called the “tangent plane”. Note that, because PUNCH is located at Earth, RTN coordinates applied to PUNCH data match the heliographic-RTN (HGRTN) coordinates defined by Fränz and Harper (2002). In cases where multiple spacecraft or vantage points may be used, we recommend using  $X_{HG}$ , etc. to denote HGRTN coordinates. Also note that RTN is similar to the heliocentric-cartesian (HC) coordinates defined by Thompson (2006), but permuted:  $X_{HC}$  and  $Y_{HC}$  loosely correspond to the image coordinates  $X_{im}$  and  $Y_{im}$  on a rectified solar image, while the corresponding RTN coordinates are Y and Z. We adopt RTN despite the permutation, both to highlight that PUNCH images are different in nature from a narrow-field sky plane projection, and also to enable easier comparison with the large body of existing solar-wind work conducted in RTN coordinates.

L2 and higher image data products from PUNCH are produced in specific projections. Historically, coronagraph images (e.g. from SOHO/LASCO Brueckner *et al.* 1995) have been created in an approximate “gnomonic” (tangent-plane) projection. PUNCH/NFI data products are produced in this projection to match the historical data sets. Gnomonic projection leaves much to be desired when extended to wide fields of view, and therefore PUNCH mosaic images are delivered in the azimuthal equidistant projection shown in the lower right panel of Figure 18. In azimuthal equidistant projection, distance from the center of the image is proportional to the elongation angle  $\varepsilon$  rather than (as in gnomonic projection) its tangent.

The two projections differ slightly but significantly in the inner part of the PUNCH field of view. In particular, the NFI FOV apparent radius (8 degrees from Sun center) is approximately 7 pixels larger in NFI data products than it would be with a comparably scaled azimuthal equidistant projection.

The “Thomson Surface” (TS) is an important figure for analysis of Thomson scattered light (Vourlidas and Howard 2006). In the point-Sun approximation (Howard and DeForest 2012b), the TS is the locus on which the scattering angle  $\chi$  happens to be  $90^\circ$ , and therefore the intersection of a given line of sight with the TS is the location of closest approach of that particular line of sight to the Sun. The TS is the sphere with a diameter extending from the Sun to the observer, following the theorem attributed to Thales of Babylonia (Laërtius c. 50).

Direct 2-D image analyses of the corona and heliosphere have typically treated features as if they’re projected onto the tangent plane: because  $r_{obs}$  is known and  $\varepsilon$  is measured by direct location in the image plane, the related distance  $r_{pos} = r_{obs} \tan \varepsilon$  is simple to calculate. Alternatively, in wide field studies (e.g. with STEREO/SECCHI, Howard *et al.* 2008), features are sometimes considered to be on or near the Thomson surface (e.g. Vourlidas and Howard 2006; DeForest, Howard, and Tappin 2013), placing them at the line-of-sight impact parameter distance  $d = r_{obs} \sin \varepsilon$  from the Sun.

PUNCH is designed for 3-D analysis using polarimetry, which makes use of additional named angles and distances in the scattering plane. The desired measurement for 3-D location is  $\ell$ , the distance from the observer to the feature<sup>7</sup>. Rather than measuring  $\ell$  directly, polarimetry yields an estimate of the scattering angle  $\chi$ ; or equivalently its complement, the Thomson angle  $\tau$  (Appendix B). That angle gives the distance  $s$  of a feature from the Thomson surface via the relation  $s = r_{obs} \sin \varepsilon \sin \tau$ ; this, in turn, yields the feature's distance  $\ell = r_{obs} \cos \varepsilon - s$  from the observer.

Some authors have preferred to use either the solar angle  $\psi$  or its complement, the out-of-sky-plane angle  $\xi$ , for direct comparison to 2-D sky-plane analyses; we observe that  $\xi = \tau + \varepsilon$ . These and other trigonometric relationships may be directly inferred by inspection of Figure 18.

## A.2. Photometric and polarimetric definitions

PUNCH measures distributed objects (features in the corona and solar wind). The fundamental measurement is photon fluence on each pixel in the instrument focal plane, through the filtering and geometry of the optics and the switchable polarizers in the instrument.

Digitizer output number from each exposure is approximately proportional to the number of visible-light photons incident on each CCD pixel during an exposure interval; after background subtraction and spectral calibration this is equivalent to a visible energy  $E_{vis}$  deposited on each pixel during each exposure; dividing by the exposure time yields a power  $P_{vis}$  (in W or, more appropriately, in femtowatts or fW) deposited on each pixel by Thomson-scattered light during data collection. Dividing by the effective area of the instrument yields an absolute intensity  $I_{vis}$  (in  $\text{W m}^{-2}$ ) at that pixel. Dividing by the solid angle subtended by each pixel yields the radiance or “brightness”  $B_{vis}$  (in  $\text{W m}^{-2} \text{ sr}^{-1}$ ), which is a photometric invariant in linear ray optics. The intensity is an extensive property and therefore is summed or integrated across features that include more than a single pixel, while the radiance is an intensive property and therefore is averaged across features that include more than a single pixel. Because PUNCH's primary science target is scattered sunlight, the natural unit for radiance is  $B_{\odot}$ , the mean solar photospheric radiance (i.e. the solar intensity  $I_{\odot}$  divided by the subtended solid angle of the Sun  $\Omega_{\odot}$ <sup>8</sup>). Delivering radiances in  $B_{\odot}$  removes the spectral profile of the instrument and the Sun itself, and the effects of solar limb darkening, from subsequent calculations of polarimetry and feature density.

PUNCH is a polarimetric instrument. Level 3 data products are delivered in dual radiance channels  $tB$  (“total brightness”) and  $pB$  (“polarized brightness”).  $tB$  is preferred nomenclature for an unpolarized total brightness data product, while the more ambiguous  $B$  may be used for generic radiance quantities but is deprecated by PUNCH. PUNCH produces two kinds of  $tB$ : “clear” images, taken with no polarizing filter in the beam, at 8 minute cadence; and “three-polarizer  $tB$ ” images, delivered as part of a  $(tB, pB)$  image pair, at 4 minute cadence.

Polarimetry may be (and has been) described in multiple ways by multiple authors; the fundamentals of the Stokes parameter formulation are covered in standard

<sup>7</sup> $\ell$ , denoted “\ell” in  $\text{\LaTeX}$  math mode, has also been called  $z$  by some authors, a usage we deprecate because it is similar to the name of a standard Cartesian axis.

<sup>8</sup>Note that  $\Omega_{\odot}$  is also used in other contexts to denote the solar average rotation rate; for that reason we typically use instead the expression  $\pi(r/r_{\odot})^2$ , which is valid for features throughout the PUNCH field of view, as well as for the familiar case where  $r = 1\text{AU}$ .

textbooks (e.g. Hecht and Zajac 1974; Born and Wolf 1999). The polarization signal expected from the far-field K corona, and the PUNCH approach to measuring it, are developed in detail by DeForest, Howard, and Tappin (2013) and DeForest, Seaton, and West (2022), respectively, and summarized here.

The Stokes system of polarimetry defines an overall unpolarized parameter  $I$  and three polarization parameters  $Q$ ,  $U$ , and  $V$ . Each parameter name has been used to describe intensity or radiance of a beam of light (or other wave), in different contexts.  $I$  represents the total radiant energy in a beam, while  $Q$ ,  $U$ , and  $V$  represent difference signals between the amount of radiant energy passing through conjugate polarizers (and hence these parameters do not represent actual radiant energy transfer but rather the character of the energy flux represented by  $I$ ).  $Q$  is the difference between brightnesses through a vertical and horizontal polarizer,  $Q \equiv B_{\parallel} - B_{\perp}$ ; and  $U$  is the difference between brightnesses through two diagonal polarizers,  $U \equiv B_{\backslash} - B_{/}$ . By convention, these orientations are defined relative to a fixed laboratory or instrument. Stokes  $V$  is the difference between brightnesses observed through two opposite circular polarizers and is not relevant to linear polarization analyses. The Stokes parameters bear the relationship  $I^2 \geq Q^2 + U^2 + V^2$ , because violating that relationship would require negative brightness values through one or more polarizers. Treated as unit vectors in a 3-space,  $I$ ,  $Q$ , and  $U$  form a complete basis for describing linear polarization.

Thomson scattering polarizes light perpendicular to the scattering plane (Figure 18), by projection of the electric field from the incident ray into the plane perpendicular to the scattered ray. This means that the radiance  $B_R$  viewed through a radially-aligned linear polarizer is less than the radiance  $B_T$  viewed through a tangentially-aligned polarizer (i.e. one oriented  $90^\circ$  to the solar-radial direction). The quantity  $B_T - B_R$  (“tangential polarized brightness”) is similar to the Stokes parameter  $Q$ , with the notable difference that  $Q$  is defined in the fixed reference frame of a laboratory, while the orientation of the polarizers for  $B_T$  and  $B_R$  varies around the image plane. We refer to  $B_T - B_R$  as  $pB$  and identify it with the  ${}^{\perp}pB$  defined by DeForest, Seaton, and West (2022). The appendix to that article, incidentally, includes a discussion of the (confusing) history of  $pB$  nomenclature, including the contrast between  ${}^{\perp}pB$  and the related but distinct quantity  ${}^{\circ}pB \equiv \sqrt{Q^2 + U^2}$  (“total linear polarized brightness”). Both quantities have been called  $pB$  in the historical literature by different (or sometimes even the same) authors; to avoid confusion, we encourage authors to define  $pB$  explicitly in every article that uses the term. The quantity  ${}^{\circ}pB$  has also been called  $L$  (Rachmeler *et al.* 2013), a usage we encourage for its distinctness from  $pB$ .

By analogy to the Stokes parameters, there exists a parameter  $pB'$  that is conjugate to  $pB$  and describes linear polarization diagonal to the radial direction on the image plane.  $pB'$  is both predicted and observed to be zero in coronal Thomson-scattered light (e.g., Filippov, Molodensky, and Koutchmy 1994). It is omitted from PUNCH L3 published data products, although the data reduction pipeline can produce  $pB'$  image products as a check on data quality.

PUNCH does not measure  $B_R$  and  $B_T$  directly. Instead, each instrument measures polarization triplets: sequences of three exposures taken through linear polarizers oriented  $60^\circ$  apart. The theory has been known for some time (Fesenkov 1935; Öhman 1947) and is recapitulated, with an eye toward modern application, by DeForest, Seaton, and West (2022). We refer to the polarization-triplet system as MZP, and to each brightness value in a triplet as  $B_M$ ,  $B_Z$ , or  $B_P$  respectively. PUNCH collects MZP triplets in each instrument’s reference frame on-orbit, then mathematically transforms them to MZP in rectified solar coordinates. This requires accounting not only for spacecraft rotation angle, but also esoterica such as projection effects that change the

effective angle of each polarizer across the image plane (Patel, Seaton, and DeForest 2025).

3-D image analysis makes use of the “degree of [tangential linear] polarization”  $p$ , which we define as  $p \equiv pB/tB$ , and the related “polarization ratio”  $B_R/B_T$ , which provide indicators of the scattering angle  $\chi$  and are described further in Appendix B.

We recommend notating the Stokes-like polarization parameters with a single prefix letter as in  $pB$  or  $tB$ , and notating real or computed radiance values (which are positive-definite) with a subscript, as in  $B_T$ ,  $B_R$ ,  $B_M$ ,  $B_Z$ , or  $B_P$ . Radiances acquired with no polarizer in the beam may be labeled  $B_C$  (for “Clear”) when it is necessary to distinguish them from the (possibly computed)  $tB$ .

## B. Polarization

PUNCH polarimetry is specifically designed to locate objects in three dimensions, via the physics of Thomson scattering. The theory has been developed to varying degrees of detail by many authors, from Minnaert (1930) and van de Hulst (1950), through Billings (1966), to modern works including Mierla *et al.* (2009) and Howard and Tappin (2009). It has been demonstrated by several authors including DeForest, de Koning, and Elliott (2017) and Mierla *et al.* (2022). PUNCH observes features that are quite far from the Sun and therefore polarimetric analysis may be simplified considerably via the point-sun approximation (DeForest, Howard, and Tappin 2013), which is important given the complexity of large distributed objects such as CMEs (Howard *et al.* 2013). In this Appendix we very briefly discuss this elementary theory of polarimetry to locate features, and refer to both prior articles that lay a more comprehensive foundation and other articles in this collection, which explore the details of distributed object polarimetry in the context of PUNCH.

PUNCH observes sunlight that is Thomson scattered by free electrons in coronal features. Thomson scattering polarizes light through projection of the inbound electric field into the perpendicular plane of the outbound rays. The electric field component perpendicular to the scattering plane (Figure 18) remains unchanged by these projection effects, while the electric field component in the scattering plane is reduced by a factor of  $\cos \chi$ . The brightness  $B_R$  from a small feature, observed through a radially-aligned polarizer, is therefore reduced by a factor of  $(\cos \chi)^2$ ; while the brightness  $B_T$ , through a polarizer perpendicular to the radial, is independent of  $\chi$ . Calculating the polarization ratio  $PR \equiv B_R/B_T$  of a small bright feature cancels out any density or geometric considerations, so that  $\chi$  may be determined via

$$\chi = \arccos(\sqrt{PR}) = \arccos\left(\sqrt{\frac{1-p}{1+p}}\right), \quad (3)$$

where  $p \equiv pB/tB$  is the degree of linear polarization from Thomson scattering. Both the  $\arccos$  and the square root have sign ambiguities, but the positive branch of the square root is forced by the geometry of the scattering plane, leaving only the sign ambiguity of the  $\arccos$  function. That ambiguity leads to a split between a “real” and a “ghost” location along the line of sight, for a feature seen in any one observation. The two locations may be distinguished by their behavior over time in multiple image sets: small ejecta from the Sun are known to follow radial trajectories, and the ghost location follows a clearly nonphysical trajectory (DeForest, Howard, and Tappin 2013; Gibson *et al.* 2025).

Figure 19 illustrates simple 3D inversion, applicable to compact features that are well isolated and fully background subtracted. Reading off the polarization ratio yields

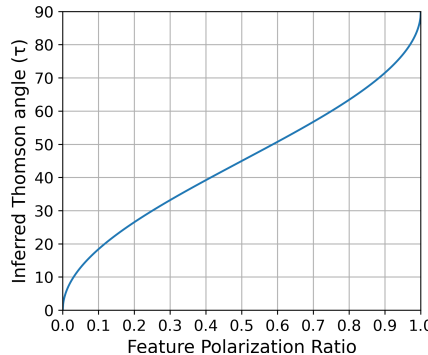


**Figure 19.** The polarization ratio  $PR \equiv B_R/B_T$  (Table 7) determines scattering angle  $\chi$  or, equivalently, its complement  $\tau$  (Figure 18) for isolated, background-subtracted bright features. For features at intermediate  $\tau$  (or  $\chi$ ) angles between roughly  $20^\circ$ - $70^\circ$ , the slope is approximately  $0.6^\circ$  per percent in  $B_R/B_T$ , so although a feature with polarization ratio of 0.3 is at approximately  $\tau = \pm 32^\circ$ , a 5% uncertainty in that feature’s  $PR$  corresponds to a roughly  $3^\circ$  uncertainty in  $\tau$ .

an estimate of the  $\tau$  angle (complement of the scattering angle  $\chi$ ). From that and the elongation  $\varepsilon$  of the feature, one may infer the out-of-sky-plane angle  $\xi$ , as shown in Figure 18. This compact-feature case, for features at least several  $r_\odot$  from the Sun itself, has been developed analytically by several authors including DeForest, Howard, and Tappin (2013). This compact-feature approximation may be used even for portions of large features (whose size is comparable to the distance from the observer or the Sun), because the 2-D leading edge of any large feature must necessarily be spatially compact along the line of sight (Howard *et al.* 2013). However, all coronal features exist against the background of myriad other K corona (or solar wind) features along each line of sight, and that “K background” must be considered and removed in addition to the backgrounds from stray light, F corona, and stellar backgrounds described in Section 6.4 (e.g., van de Hulst 1950; DeForest, de Koning, and Elliott 2017).

Both distributed-object effects and background effects are important to many of the objects observed by PUNCH; polarimetric theory for these measurements is developed in some detail elsewhere in this collection: by Gibson *et al.* (2025) for general solar wind observations, by Malanushenko *et al.* (2025) in the context of coronal mass ejections, and by de Koning *et al.* (2025) in the context of stream interaction regions.

## References

Angarita, Y., Versteeg, M.J.F., Havercorn, M., Rodrigues, C.V., Magalhães, A.M., Santos-Lima, R., Kawabata, K.S.: 2023, Interstellar Polarization Survey. III. Relation between Optical Polarization and Reddening in the General Interstellar Medium. *The Astronomical Journal* **166**(1), 34. DOI. <https://iopscience.iop.org/article/10.3847/1538-3881/acdc1e>.

Angarita, Y., Versteeg, M.J.F., Havercorn, M., Marchal, A., Rodrigues, C.V., Magalhães, A.M., Santos-Lima, R., Kawabata, K.S.: 2024, Interstellar Polarization Survey. IV. Characterizing the Magnetic Field Strength and Turbulent Dispersion Using Optical Starlight Polarization in the Diffuse Interstellar Medium. *The Astronomical Journal* **168**(1), 47. DOI. <https://iopscience.iop.org/article/10.3847/1538-3881/ad4b14>.

Antiochos, S.K., Mikić, Z., Titov, V.S., Lionello, R., Linker, J.A.: 2011, A Model for the Sources of the Slow Solar Wind. *Astrophys. J.* **731**(2), 112. DOI. ADS.

Attié, R., Gibson, S., et al.: 2025, Flow Tracking and Solar Wind Measurement for PUNCH. *Solar Physics* in work.

Bandyopadhyay, R., Matthaeus, W.H., McComas, D.J., Chhiber, R., Usmanov, A.V., Huang, J., Livi, R., Larson, D.E., Kasper, J.C., Case, A.W., Stevens, M., Whittlesey, P., Romeo, O.M., Bale, S.D., Bonnell, J.W., Dudok de Wit, T., Goetz, K., Harvey, P.R., MacDowall, R.J., Malaspina, D.M., Pulupa, M.: 2022, Sub-Alfvénic Solar Wind Observed by the Parker Solar Probe: Characterization of Turbulence, Anisotropy, Intermittency, and Switchback. *Astrophys. J. Lett.* **926**(1), L1. [DOI](#). [ADS](#).

Billings, D.E.: 1966, *A Guide to the Solar Corona*, Academic Press, New York. [ADS](#).

Bisi, M.M., Jackson, B.V., Hick, P.P., Buffington, A., Odstrcil, D., Clover, J.M.: 2008, Three-dimensional reconstructions of the early November 2004 Coordinated Data Analysis Workshop geomagnetic storms: Analyses of STELab IPS speed and SMEI density data. *Journal of Geophysical Research (Space Physics)* **113**(A3), A00A11. [DOI](#). [ADS](#).

Bisi, M.M., Fallows, R.A., Breen, A.R., O'Neill, I.J.: 2010, Interplanetary Scintillation Observations of Stream Interaction Regions in the Solar Wind. *Solar Phys.* **261**(1), 149. [DOI](#). [ADS](#).

Bolin, B.T., Ahumada, T., van Dokkum, P., Fremling, C., Granvik, M., Hardegree-Ullman, K.K., Harikane, Y., Purdum, J.N., Serabyn, E., Southworth, J., Zhai, C.: 2022, The discovery and characterization of (594913) 'Ayló'chaxnim, a kilometre sized asteroid inside the orbit of Venus. *Mon. Not. Roy. Astron. Soc.* **517**(1), L49. [DOI](#). [ADS](#).

Born, M., Wolf, E.: 1999, *Principles of Optics: Electromagnetic Theory of Propagation, Interference and Diffraction of Light*, 7th, expanded edn. Cambridge University Press, Cambridge. ISBN 9780521642224.

Borovsky, J.E.: 2008, Flux tube texture of the solar wind: Strands of the magnetic carpet at 1 AU? *Journal of Geophysical Research (Space Physics)* **113**(A8), A08110. [DOI](#). [ADS](#).

Bottke, W.F., Vokrouhlický, D., Ballouz, R.-L., Barnouin, O.S., Connolly, H.C., Elder, C., Marchi, S., McCoy, T.J., Michel, P., Nolan, M.C., Rizk, B., Scheeres, D.J., Schwartz, S.R., Walsh, K.J., Lauretta, D.S.: 2020, Interpreting the cratering histories of bennu, ryugu, and other spacecraft-explored asteroids. *The Astronomical Journal* **160**(1), 14. [DOI](#). <https://dx.doi.org/10.3847/1538-3881/ab88d3>.

Breen, A.R., Moran, P.J., Varley, C.A., Wilkinson, W.P., Williams, P.J.S., Coles, W.A., Lecinski, A., Markkanen, J.: 1998, Interplanetary scintillation observations of interaction regions in the solar wind. *Annales Geophysicae* **16**(10), 1265. [DOI](#). [ADS](#).

Brueckner, G.E., Howard, R.A., Koomen, M.J., Korendyke, C.M., Michels, D.J., Moses, J.D., Socker, D.G., Dere, K.P., Lamy, P.L., Llebaria, A., Bout, M.V., Schwenn, R., Simnett, G.M., Bedford, D.K., Eyles, C.J.: 1995, The Large Angle Spectroscopic Coronagraph (LASCO). *Solar Phys.* **162**(1-2), 357. [DOI](#). [ADS](#).

Bruno, R., Carbone, V., Veltri, P., Pietropaolo, E., Bavassano, B.: 2001, Identifying intermittency events in the solar wind. *Planetary and Space Science* **49**(12), 1201. [DOI](#). [ADS](#).

Bucik, R., Gomez-Herrero, R., Korth, A., Mall, U., Mason, G.: 2009, Energetic Ions from Corotating Interaction Regions During Small Solar Events in May 2007. In: Király, P., Kudela, K., Stehlík, M., Wolfendale, A.W. (eds.) *21st European Cosmic Ray Symposium*, 322. [ADS](#).

Burlaga, L.: 1984, Mhd processes in the outer heliosphere. *Space science reviews* **39**(3), 255.

Cairns, I.H., Knock, S.A., Robinson, P.A., Kuncic, Z.: 2003, Type II Solar Radio Bursts: Theory and Space Weather Implications. *Space Sci. Rev.* **107**(1), 27. [DOI](#). [ADS](#).

Calabretta, M.R., Greisen, E.W.: 2002, Representations of celestial coordinates in fits. *Astronomy & Astrophysics* **395**(3), 1077.

Chae, J., Schühle, U., Lemaire, P.: 1998, SUMER Measurements of Nonthermal Motions: Constraints on Coronal Heating Mechanisms. *Astrophys. J.* **505**(2), 957. [DOI](#). [ADS](#).

Chen, Y., Li, X., Song, H.Q., Shi, Q.Q., Feng, S.W., Xia, L.D.: 2009, Intrinsic Instability of Coronal Streamers. *Astrophys. J.* **691**(2), 1936. [DOI](#). [ADS](#).

Chhiber, R., Usmanov, A.V., DeForest, C.E., Matthaeus, W.H., Parashar, T.N., Goldstein, M.L.: 2018, Weakened Magnetization and Onset of Large-scale Turbulence in the Young Solar Wind—Comparisons of Remote Sensing Observations with Simulation. *Astrophys. J. Lett.* **856**(2), L39. [DOI](#). [ADS](#).

Chhiber, R., Matthaeus, W.H., Usmanov, A.V., Bandyopadhyay, R., Goldstein, M.L.: 2022, An extended and fragmented Alfvén zone in the Young Solar Wind. *Mon. Not. Roy. Astron. Soc.* **513**(1), 159. [DOI](#). [ADS](#).

Clarke, D.: 2009, *Stellar polarimetry*, John Wiley & Sons, Weinheim. ISBN 978-3-527-40895-5.

Colaninno, R., Thernisien, A., Howard, R., Brechbiel, D., Dennison, H., Hess, P., Koss, S., Noya, M., Simon, W., Thompson, A., McMullin, D., Laut, S., Hunt, T., Gardner, L., Lanagan, A., Hagoor, R., Hohl, B., Uhl, A., Smith, L., Zurcher, D., Stump, E., Newman, M., Ragan, T., Caron, J.: 2025, The Narrow Field Imager (NFI) for the Polarimeter to Unify the Corona and Heliosphere (PUNCH). *Solar Phys.* **300**(8), 104. [DOI](#). [ADS](#).

Coleman, J. Paul J.: 1968, Turbulence, Viscosity, and Dissipation in the Solar-Wind Plasma. *Astrophys. J.* **153**, 371. [DOI](#). [ADS](#).

Coles, W.A., Harmon, J.K.: 1989, Propagation Observations of the Solar Wind near the Sun. *Astrophys. J.* **337**, 1023. [DOI](#). [ADS](#).

Conlon, T.M., Milan, S.E., Davies, J.A., Williams, A.O.: 2015, Corotating Interaction Regions as Seen by the STEREO Heliospheric Imagers 2007 - 2010. *Solar Phys.* **290**(8), 2291. [DOI](#). [ADS](#).

Cranmer, S.R.: 2020, Heating Rates for Protons and Electrons in Polar Coronal Holes: Empirical Constraints from the Ultraviolet Coronagraph Spectrometer. *Astrophys. J.* **900**(2), 105. [DOI](#). [ADS](#).

Cranmer, S.R., Winebarger, A.R.: 2019, The Properties of the Solar Corona and Its Connection to the Solar Wind. *Ann. Rev. Astron. Astrophys.* **57**, 157. [DOI](#). [ADS](#).

Cranmer, S.R., DeForest, C.E., Gibson, S.E.: 2021, Inward-propagating Plasma Parcels in the Solar Corona: Models with Aerodynamic Drag, Ablation, and Snowplow Accretion. *Astrophys. J.* **913**(1), 4. [DOI](#). [ADS](#).

Cranmer, S.R., Gibson, S.E., Riley, P.: 2017, Origins of the Ambient Solar Wind: Implications for Space Weather. *Space Sci. Rev.* **212**(3-4), 1345. [DOI](#). [ADS](#).

Cranmer, S.R., van Ballegooijen, A.A., Edgar, R.J.: 2007, Self-consistent Coronal Heating and Solar Wind Acceleration from Anisotropic Magnetohydrodynamic Turbulence. *Astrophys. J. Suppl.* **171**(2), 520. [DOI](#). [ADS](#).

Cranmer, S.R., Chhiber, R., Gilly, C.R., Cairns, I.H., Colaninno, R.C., McComas, D.J., Raouafi, N.E., Usmanov, A.V., Gibson, S.E., DeForest, C.E.: 2023, The sun's alfvén surface: Recent insights and prospects for the polarimeter to unify the corona and heliosphere (punch). *Solar Physics* **298**(11), 126.

Crighton, D.G., Leppington, F.G.: 1969, Distortion of sonic bangs by atmospheric turbulence. *Journal of Fluid Mechanics* **37**, 529. [DOI](#). [ADS](#).

Davies, J.A., Harrison, R.A., Rouillard, A.P., Sheeley, N.R., Perry, C.H., Bewsher, D., Davis, C.J., Eyles, C.J., Crothers, S.R., Brown, D.S.: 2009, A synoptic view of solar transient evolution in the inner heliosphere using the Heliospheric Imagers on STEREO. *Geophys. Res. Lett.* **36**(2), L02102. [DOI](#). [ADS](#).

Dayeh, M.A., Starkey, M.J., Elliott, H.A., Attie, R., DeForest, C.E., Bučík, R., Desai, M.I.: 2025, Forecasting Shock-Associated Energetic Particle Intensities in the Inner Heliosphere: A Proof-of-Concept Capability for the PUNCH Mission. *Solar Phys.* **300**(1), 1. [DOI](#). [ADS](#).

de Koning, C.A., Pizzo, V., Biesecker, D.: 2009, Geometric localization of cmes in 3d space using stereo beacon data: First results. *Solar Physics* **256**, 167.

de Koning, C.A., DeForest, C.E., Gibson, S.E., Others: 2025, Stream interaction region observations with punch. *Sol. Phys.* **In work**.

DeForest, C.E.: 2004, On Re-sampling of Solar Images. *Solar Phys.* **219**(1), 3. [DOI](#). [ADS](#).

DeForest, C.E.: 2007, On the Size of Structures in the Solar Corona. *Astrophys. J.* **661**(1), 532. [DOI](#). [ADS](#).

DeForest, C.E., de Koning, C.A., Elliott, H.A.: 2017, 3D Polarized Imaging of Coronal Mass Ejections: Chirality of a CME. *Astrophys. J.* **850**(2), 130. [DOI](#). [ADS](#).

DeForest, C.E., Howard, T.A., McComas, D.J.: 2013, Tracking Coronal Features from the Low Corona to Earth: A Quantitative Analysis of the 2008 December 12 Coronal Mass Ejection. *Astrophys. J.* **769**(1), 43. [DOI](#). [ADS](#).

DeForest, C.E., Howard, T.A., McComas, D.J.: 2014, Inbound Waves in the Solar Corona: A Direct Indicator of Alfvén Surface Location. *Astrophys. J.* **787**(2), 124. [DOI](#). [ADS](#).

DeForest, C.E., Howard, T.A., Tappin, S.J.: 2011, Observations of Detailed Structure in the Solar Wind at 1 AU with STEREO/HI-2. *Astrophys. J.* **738**(1), 103. [DOI](#).

DeForest, C.E., Howard, T.A., Tappin, S.J.: 2013, The Thomson Surface. II. Polarization. *Astrophys. J.* **765**(1), 44. [DOI](#). [ADS](#).

DeForest, C.E., Seaton, D.B., West, M.J.: 2022, Three-polarizer treatment of linear polarization in coronagraphs and heliospheric imagers. *The Astrophysical Journal* **927**(1), 98.

DeForest, C.E., Hagenaar, H.J., Lamb, D.A., Parnell, C.E., Welsch, B.T.: 2007, Solar Magnetic Tracking. I. Software Comparison and Recommended Practices. *Astrophys. J.* **666**(1), 576. [DOI](#). [ADS](#).

DeForest, C.E., Matthaeus, W.H., Howard, T.A., Rice, D.R.: 2015, Turbulence in the Solar Wind Measured with Comet Tail Test Particles. *Astrophys. J.* **812**(2), 108. [DOI](#). [ADS](#).

DeForest, C.E., Matthaeus, W.H., Viall, N.M., Cranmer, S.R.: 2016, Fading Coronal Structure and the Onset of Turbulence in the Young Solar Wind. *Astrophys. J.* **828**(2), 66. [DOI](#). [ADS](#).

DeForest, C.E., Howard, R.A., Velli, M., Viall, N., Vourlidas, A.: 2018, The Highly Structured Outer Solar Corona. *Astrophys. J.* **862**(1), 18. [DOI](#). [ADS](#).

DeForest, C.E., Lowder, C., Seaton, D.B., West, M.J.: 2022, Square root compression and noise effects in digitally transformed images. *The Astrophysical Journal* **934**(2), 179.

DeForest, C.E., Erickson, N.F., Beasley, M.N., Osterman, S.N., Smith, T.J., Hanson, M.H.: 2025, A simplified theory of external occulters for solar coronagraphs. *The Astrophysical Journal* **982**(1), 58.

Deienno, R., Denneau, L., Nesvorný, D., Vokrouhlický, D., Bottke, W.F., Jedicke, R., Naidu, S., Chesley, S.R., Farnocchia, D., Chodas, P.W.: 2025, The debiased Near-Earth object population from ATLAS telescopes. *Icarus* **425**, 116316. [DOI](#). [ADS](#).

Dere, K.P., Brueckner, G.E., Howard, R.A., Michels, D.J., Delaboudiniere, J.P.: 1999, LASCO and EIT Observations of Helical Structure in Coronal Mass Ejections. *Astrophys. J.* **516**(1), 465. [DOI](#). [ADS](#).

Di Matteo, S., Villante, U., Viall, N., Kepko, L., Wallace, S.: 2022, On Differentiating Multiple Types of ULF Magnetospheric Waves in Response to Solar Wind Periodic Density Structures. *Journal of Geophysical Research (Space Physics)* **127**(3), e30144. [DOI](#). [ADS](#).

Domingo, V., Fleck, B., Poland, A.I.: 1995, The soho mission: an overview. *Solar Physics* **162**, 1.

Dorrian, G.D., Breen, A.R., Davies, J.A., Rouillard, A.P., Fallows, R.A., Whittaker, I.C., Brown, D.S., Harrison, R.A., Davis, C.J., Grande, M.: 2010, Transient Structures and Stream Interaction Regions in the Solar Wind: Results from EISCAT Interplanetary Scintillation, STEREO HI and Venus Express ASPERA-4 Measurements. *Solar Phys.* **265**(1-2), 207. [DOI](#). [ADS](#).

Dudley, R.P., Krimchansky, A., Tadijkonda, S.K., Thernisien, A.F., Baugh, R.A., Dahya, M., Vassiliadis, D., Korendyke, C.: 2023, Compact coronagraph (ccor) accommodation on goes-u. In: *Proceedings of the European Geosciences Union General Assembly (EGU23)*. <https://ntrs.nasa.gov/citations/20230004075>.

Dumont, R., Sanchez, F.: 1976, Zodiacal light photopolarimetry. III. All-sky survey from Teide 1964 - 1975 with emphasis on off-ecliptic features. *Astron. Astrophys.* **51**, 393. [ADS](#).

Elliott, H.A., McComas, D.J., Matthaeus, W.H., Henney, C.J.: 2010, Solar Wind Speed And Temperature Relationship. In: Maksimovic, M., Issautier, K., Meyer-Vernet, N., Moncuquet, M., Pantellini, F. (eds.) *Twelfth International Solar Wind Conference, American Institute of Physics Conference Series* **1216**, 98. [DOI](#). [ADS](#).

Endeve, E., Holzer, T.E., Leer, E.: 2004, Helmet Streamers Gone Unstable: Two-Fluid Magnetohydrodynamic Models of the Solar Corona. *Astrophys. J.* **603**(1), 307. [DOI](#). [ADS](#).

Eyles, C.J., Simnett, G.M., Cooke, M.P., Jackson, B.V., Buffington, A., Hick, P.P., Waltham, N.R., King, J.M., Anderson, P.A., Holladay, P.E.: 2003, The Solar Mass Ejection Imager (Smei). *Solar Phys.* **217**(2), 319. [DOI](#). [ADS](#).

Eyles, C.J., Harrison, R.A., Davis, C.J., Waltham, N.R., Shaughnessy, B.M., Mapson-Menard, H.C.A., Bewsher, D., Crothers, S.R., Davies, J.A., Simnett, G.M., Howard, R.A., Moses, J.D., Newmark, J.S., Socker, D.G., Halain, J.-P., Defise, J.-M., Mazy, E., Rochus, P.: 2009, The Heliospheric Imagers Onboard the STEREO Mission. *Solar Phys.* **254**(2), 387. [DOI](#).

Feng, L., Inhester, B., Wei, Y., Gan, W.Q., Zhang, T.L., Wang, M.Y.: 2012, Morphological Evolution of a Three-dimensional Coronal Mass Ejection Cloud Reconstructed from Three Viewpoints. *Astrophys. J.* **751**(1), 18. [DOI](#). [ADS](#).

Fesenkov, V.G.: 1935, *Russian Astronomical Journal* **XII**(4), 310.

Filippov, B.P., Molodensky, M.M., Koutchmy, S.: 1994, On the Optical Polarization of the White-Light Coronal Structures. In: Rusin, V., Heinzel, P., Vial, J.-C. (eds.) *IAU Colloq. 144: Solar Coronal Structures*, 601. [ADS](#).

Fisk, L.A., Gloeckler, G., Zurbuchen, T.H., Geiss, J., Schwadron, N.A.: 2003, Acceleration of the Solar Wind as a Result of the Reconnection of Open Magnetic Flux with Coronal Loops. In: Velli, M., Bruno, R., Malara, F., Bucci, B. (eds.) *Solar Wind Ten, American Institute of Physics Conference Series* **679**, 287. [DOI](#). [ADS](#).

Fossati, L., Bagnulo, S., Mason, E., Landi Degl'Innocenti, E.: 2007, Standard Stars for Linear Polarization Observed with FORS1. In: Sterken, C. (ed.) *The Future of Photometric, Spectrophotometric and Polarimetric Standardization, Astronomical Society of the Pacific Conference Series* **364**, 503. [ADS](#).

Fox, N.J., Velli, M.C., Bale, S.D., Decker, R., Driesman, A., Howard, R.A., Kasper, J.C., Kinnison, J., Kusterer, M., Lario, D., Lockwood, M.K., McComas, D.J., Raouafi, N.E., Szabo, A.: 2016, The Solar Probe Plus Mission: Humanity's First Visit to Our Star. *Space Sci. Rev.* **204**(1-4), 7. [DOI](#). [ADS](#).

Fränz, M., Harper, D.: 2002, Heliospheric coordinate systems. *Planetary and Space Science* **50**(2), 217.

Garraffo, C., Drake, J.J., Cohen, O.: 2015, The Dependence of Stellar Mass and Angular Momentum Losses on Latitude and the Interaction of Active Region and Dipolar Magnetic Fields. *Astrophys. J.* **813**(1), 40. [DOI](#). [ADS](#).

Giacalone, J., Jokipii, J.R.: 2007, Magnetic Field Amplification by Shocks in Turbulent Fluids. *Astrophys. J. Lett.* **663**(1), L41. [DOI](#). [ADS](#).

Gibson, S.: 2015, Coronal Cavities: Observations and Implications for the Magnetic Environment of Prominences. In: Vial, J.-C., Engvold, O. (eds.) *Solar Prominences, Astrophysics and Space Science Library* **415**, 323. [DOI](#). [ADS](#).

Gibson, S.E., DeForest, C.E., de Koning, C., et al.: 2025, Polarization diagnostics applied to coronal mass ejections and the background solar wind. *Sol. Phys.* **In work**.

Goelzer, M.L., Schwadron, N.A., Smith, C.W.: 2014, An analysis of Alfvén radius based on sunspot number from 1749 to today. *Journal of Geophysical Research (Space Physics)* **119**(1), 115. [DOI](#). [ADS](#).

Goldstein, M.L., Roberts, D.A.: 1999, Magnetohydrodynamic turbulence in the solar wind. *Physics of Plasmas* **6**(11), 4154. [DOI](#). [ADS](#).

Gopalswamy, N., Yashiro, S., Kaiser, M.L., Howard, R.A., Bougeret, J.-L.: 2001, Radio Signatures of Coronal Mass Ejection Interaction: Coronal Mass Ejection Cannibalism? *Astrophys. J. Lett.* **548**(1), L91. [DOI](#). [ADS](#).

Gosling, J.T., Thomsen, M.F., Bame, S.J., Zwickl, R.D.: 1987, The eastward deflection of fast coronal mass ejecta in interplanetary space. *J. Geophys. Res.* **92**(A11), 12399. [DOI](#). [ADS](#).

Gosling, J.T., Skoug, R.M., McComas, D.J., Smith, C.W.: 2005, Direct evidence for magnetic reconnection in the solar wind near 1 AU. *Journal of Geophysical Research (Space Physics)* **110**(A1), A01107. [DOI](#). [ADS](#).

Hall, J.S.: 1949, Observations of the Polarized Light From Stars. *Science* **109**(2825), 166. [DOI](#). <https://www.science.org/doi/10.1126/science.109.2825.166>.

Hanson, e.a. M.: 2025, The Student Thermal Energetic Activity Monitor (STEAM) for the Polarimeter to UNify the Corona and Heliosphere (PUNCH) mission. *Solar Physics* **in work**.

Hardwick, S.A., Bisi, M.M., Davies, J.A., Breen, A.R., Fallows, R.A., Harrison, R.A., Davis, C.J.: 2013, Observations of Rapid Velocity Variations in the Slow Solar Wind. *Solar Phys.* **285**(1-2), 111. [DOI](#). [ADS](#).

Harrison, R.A., Davies, J.A., Möstl, C., Liu, Y., Temmer, M., Bisi, M.M., Eastwood, J.P., de Koning, C.A., Nitta, N., Rollett, T., Farrugia, C.J., Forsyth, R.J., Jackson, B.V., Jensen, E.A., Kilpua, E.K.J., Odstrcil, D., Webb, D.F.: 2012, An Analysis of the Origin and Propagation of the Multiple Coronal Mass Ejections of 2010 August 1. *Astrophys. J.* **750**(1), 45. [DOI](#). [ADS](#).

Hecht, E., Zajac, A.: 1974, *Optics*, 1st edn. Addison-Wesley, Reading, Massachusetts. First edition.

Heiles, C.: 2000, 9286 Stars: An Agglomeration of Stellar Polarization Catalogs. *Astron. J.* **119**(2), 923. [DOI](#). [ADS](#).

Hill, F., Martens, P., Yoshimura, K., Gurman, J., Hourclé, J., Dimitoglou, G., Suárez-Solá, I., Wampler, S., Reardon, K., Davey, A., et al.: 2009, The virtual solar observatory—a resource for international heliophysics research. *Earth, Moon, and Planets* **104**, 315.

Hiltner, W.A.: 1949, On the Presence of Polarization in the Continuous Radiation of Stars. II. *The Astrophysical Journal* **109**, 471. [DOI](#). <http://adsabs.harvard.edu/doi/10.1086/145151>.

Howard, R.A., Moses, J.D., Vourlidas, A., Newmark, J.S., Socker, D.G., Plunkett, S.P., Korendyke, C.M., Cook, J.W., Hurley, A., Davila, J.M., Thompson, W.T., St Cyr, O.C., Mentzell, E., Mehalick, K., Lemen, J.R., Wuelser, J.P., Duncan, D.W., Tarbell, T.D., Wolfson, C.J., Moore, A., Harrison, R.A., Waltham, N.R., Lang, J., Davis, C.J., Eyles, C.J., Mapson-Menard, H., Simnett, G.M., Halain, J.P., Defise, J.M., Mazy, E., Rochus, P., Mercier, R., Ravet, M.F., Delmotte, F., Auchere, F., Delaboudiniere, J.P., Bothmer, V., Deutsch, W., Wang, D., Rich, N., Cooper, S., Stephens, V., Maahs, G., Baugh, R., McMullin, D., Carter, T.: 2008, Sun Earth Connection Coronal and Heliospheric Investigation (SECCHI). *Space Sci. Rev.* **136**(1-4), 67. [DOI](#).

Howard, R.A., Vourlidas, A., Colaninno, R.C., Korendyke, C.M., Plunkett, S.P., Carter, M.T., Wang, D., Rich, N., Lynch, S., Thurn, A., Socker, D.G., Thernisien, A.F., Chua, D., Linton, M.G., Koss, S., Tun-Beltran, S., Dennison, H., Stenborg, G., McMullin, D.R., Hunt, T., Baugh, R., Clifford, G., Keller, D., Janesick, J.R., Tower, J., Grygon, M., Farkas, R., Hagood, R., Eisenhauer, K., Uhl, A., Yerushalmi, S., Smith, L., Liewer, P.C., Velli, M.C., Linker, J., Bothmer, V., Rochus, P., Halain, J.-P., Lamy, P.L., Auchère, F., Harrison, R.A., Rouillard, A., Patsourakos, S., St. Cyr, O.C., Gilbert, H., Maldonado, H., Mariano, C., Cerullo, J.: 2020, The Solar Orbiter Heliospheric Imager (SoloHI). *Astron. Astrophys.* **642**, A13. [DOI](#).

Howard, T.A., DeForest, C.E.: 2012a, Inner Heliospheric Flux Rope Evolution via Imaging of Coronal Mass Ejections. *Astrophys. J.* **746**(1), 64. [DOI](#). [ADS](#).

Howard, T.A., DeForest, C.E.: 2012b, The Thomson Surface. I. Reality and Myth. *Astrophys. J.* **752**(2), 130. [DOI](#). [ADS](#).

Howard, T.A., Tappin, S.J.: 2009, Interplanetary Coronal Mass Ejections Observed in the Heliosphere: 1. Review of Theory. *Space Sci. Rev.* **147**(1-2), 31. [DOI](#). [ADS](#).

Howard, T.A., Tappin, S.J., Odstrcil, D., DeForest, C.E.: 2013, The Thomson Surface. III. Tracking Features in 3D. *Astrophys. J.* **765**(1), 45. [DOI](#). [ADS](#).

Hsu, J.-C., Breger, M.: 1982, On standard polarized stars. *The Astrophysical Journal* **262**, 732. [DOI](#). <http://adsabs.harvard.edu/doi/10.1086/160467>.

Huang, Z., Velli, M., Shi, C., Zhu, Y., Chandran, B.D.G., Bowen, T., Réville, V., Huang, J., Hou, C., Sioulas, N., Liu, M., Pulupa, M., Huang, S., Bale, S.D.: 2024, Dominance of 2 Minute Oscillations near the Alfvén Surface. *Astrophys. J. Lett.* **977**(1), L12. [DOI](#). [ADS](#).

Hughes, M., one, two, three: 2025, The Science Operations Center (SOC) for the Polarimeter to UNify the Corona and Heliosphere (PUNCH) mission. *Solar Physics* **in work**.

Hundhausen, A.J.: 1972, *Coronal Expansion and Solar Wind*, Springer-Verlag, Berlin. ISBN 978-3-642-65414-5. [ADS](#).

Hundhausen, A.J.: 1985, Some macroscopic properties of shock waves in the heliosphere. *Washington DC American Geophysical Union Geophysical Monograph Series* **34**, 37. [DOI](#). [ADS](#).

Ireland, J., Davey, A., Inglis, A., Mansky, E., Martens, P., Yashiro, S.: 2022, Solar data analysis center initiatives to promote open science. *Third Triennial Earth-Sun Summit (TESS)* **54**(7).

Isavnin, A., Vourlidas, A., Kilpua, E.K.J.: 2014, Three-Dimensional Evolution of Flux-Rope CMEs and Its Relation to the Local Orientation of the Heliospheric Current Sheet. *Solar Phys.* **289**(6), 2141. [DOI](#). [ADS](#).

Jackson, B.V., Leinert, C.: 1985, Helios images of solar mass ejections. *Journal of Geophysical Research: Space Physics* **90**(A11), 10759. [DOI](#). <http://onlinelibrary.wiley.com/doi/10.1029/JA090iA11p10759/abstract>.

Jackson, B.V., Buffington, A., Hick, P.P., Altrock, R.C., Figueira, S., Holladay, P.E., Johnston, J.C., Kahler, S.W., Mozer, J.B., Price, S., Radick, R.R., Sagalyn, R., Sinclair, D., Simnett, G.M., Eyles, C.J., Cooke, M.P., Tappin, S.J., Kuchar, T., Mizuno, D., Webb, D.F., Anderson, P.A., Keil, S.L., Gold, R.E., Waltham, N.R.: 2004, The Solar Mass-Ejection Imager (SMEI) Mission. *Solar Phys.* **225**(1), 177. [DOI](#).

Jackson, B.V., Buffington, A., Hick, P.P., Wang, X., Webb, D.: 2006, Preliminary three-dimensional analysis of the heliospheric response to the 28 October 2003 CME using SMEI white-light observations. *Journal of Geophysical Research (Space Physics)* **111**(A4), A04S91. [DOI](#). [ADS](#).

Jackson, B.V., Hick, P.P., Buffington, A., Bisi, M.M., Clover, J.M.: 2009, SMEI direct, 3-D-reconstruction sky maps, and volumetric analyses, and their comparison with SOHO and STEREO observations. *Annales Geophysicae* **27**(11), 4097. [DOI](#). [ADS](#).

Jackson, B.V., Hick, P.P., Buffington, A., Bisi, M.M., Clover, J.M., Tokumaru, M., Kojima, M., Fujiki, K.: 2011, Three-dimensional reconstruction of heliospheric structure using iterative tomography: A review. *Journal of Atmospheric and Solar-Terrestrial Physics* **73**(10), 1214. [DOI](#). [ADS](#).

Jones, M.H., Bewsher, D., Brown, D.S.: 2017, Mapping the circumsolar dust ring near the orbit of Venus. *Icarus* **288**, 172. [DOI](#). [ADS](#).

Kaila, K.U.: 1989, Determination of the energy of auroral electrons by the measurements of the emission ratio and altitude of aurorae. *Planetary and Space Science* **37**(3), 341. [DOI](#). [ADS](#).

Kasper, J.C., Lazarus, A.J., Szabo, A., Ogilvie, K.W., Skoug, R., Steinberg, J.T., Smith, C.: 2005, Survey of interplanetary shock characteristics. In: *AGU Fall Meeting Abstracts* **2005**, SH52A. [ADS](#).

Kasper, J.C., Klein, K.G., Lichko, E., Huang, J., Chen, C.H.K., Badman, S.T., Bonnell, J., Whittlesey, P.L., Livi, R., Larson, D., Pulupa, M., Rahmati, A., Stansby, D., Korreck, K.E., Stevens, M., Case, A.W., Bale, S.D., Maksimovic, M., Moncuquet, M., Goetz, K., Halekas, J.S., Malaspina, D., Raouafi, N.E., Szabo, A., MacDowall, R., Velli, M., Dudok de Wit, T., Zank, G.P.: 2021, Parker Solar Probe Enters the Magnetically Dominated Solar Corona. *Phys. Rev. Lett.* **127**(25), 255101. [DOI](#). [ADS](#).

Katsavriias, C., Di Matteo, S., Kepko, L., Viall, N.M.: 2025, The dependence of periodic density structures' amplitude and length scale on solar wind density within stream interaction regions. *Astron. Astrophys.* **696**, L20. [DOI](#). [ADS](#).

Kepko, L., Viall, N.M.: 2019, The Source, Significance, and Magnetospheric Impact of Periodic Density Structures Within Stream Interaction Regions. *Journal of Geophysical Research (Space Physics)* **124**(10), 7722. [DOI](#). [ADS](#).

Kepko, L., Viall, N.M., DiMatteo, S.: 2024, Periodic Mesoscale Density Structures Comprise a Significant Fraction of the Solar Wind and Are Formed at the Sun. *Journal of Geophysical Research (Space Physics)* **129**(1), e2023JA031403. [DOI](#). [ADS](#).

Kepko, L., Viall, N.M., Antiochos, S.K., Lepri, S.T., Kasper, J.C., Weberg, M.: 2016, Implications of L1 observations for slow solar wind formation by solar reconnection. *Geophys. Res. Lett.* **43**(9), 4089. [DOI](#). [ADS](#).

Khabarova, O.V., Zank, G.P., Li, G., Malandraki, O.E., le Roux, J.A., Webb, G.M.: 2016, Small-scale Magnetic Islands in the Solar Wind and Their Role in Particle Acceleration. II. Particle Energization inside Magnetically Confined Cavities. *Astrophys. J.* **827**(2), 122. [DOI](#). [ADS](#).

Kilpua, E.K.J., Hietala, H., Turner, D.L., Koskinen, H.E.J., Pulkkinen, T.I., Rodriguez, J.V., Reeves, G.D., Claudepierre, S.G., Spence, H.E.: 2015, Unraveling the drivers of the storm time radiation belt response. *Geophys. Res. Lett.* **42**(9), 3076. [DOI](#). [ADS](#).

Knight, M.M., A'Hearn, M.F., Biesecker, D.A., Faury, G., Hamilton, D.P., Lamy, P., Llebaria, A.: 2010, Photometric Study of the Kreutz Comets Observed by SOHO from 1996 to 2005. *Astron. J.* **139**(3), 926. [DOI](#). [ADS](#).

Knock, S.A., Cairns, I.H., Robinson, P.A., Kuncic, Z.: 2003, Theoretically predicted properties of type II radio emission from an interplanetary foreshock. *Journal of Geophysical Research (Space Physics)* **108**(A3), 1126. [DOI](#). [ADS](#).

Kohl, J.L., Noci, G., Cranmer, S.R., Raymond, J.C.: 2006, Ultraviolet spectroscopy of the extended solar corona. *Astron. Astrophys. Rev.* **13**(1-2), 31. [DOI](#). [ADS](#).

Koomen, M.J., Detwiler, C.R., Brueckner, G.E., Cooper, H.W., Tousey, R.: 1975, White light coronagraph in OSO 7. *Applied Optics* **14**(3), 743. [DOI](#).

Korendyke, C.M.: 1993, Measured performance and description of the Naval Research Laboratory solar coronagraph optical test chamber and instrument clean room. In: Huffman, R.E. (ed.) *Ultraviolet Technology IV* **1764**, SPIE, ???, 289. International Society for Optics and Photonics. [DOI](#). <https://doi.org/10.1117/12.140858>.

Koutchmy, S., Lamy, P.L.: 1985, The F-Corona and the Circum-Solar Dust Evidences and Properties (ir). In: Giese, R.H., Lamy, P. (eds.) *IAU Colloquium 85: Properties and Interactions of Interplanetary Dust, Astrophysics and Space Science Library* **119**, 63. [DOI](#). [ADS](#).

Kurien, L.V., Kanekal, S.G., Di Matteo, S., Greeley, A.D., Schiller, Q., Shumko, M., Viall, N.M., Kepko, E.L.: 2024, Outer Zone Relativistic Electron Response to Mesoscale Periodic Density Structures in the Solar Wind: Van Allen Probes Measurements. *Journal of Geophysical Research (Space Physics)* **129**(10), e2024JA032614. [DOI](#). [ADS](#).

Laërtius, D.: c. 50, *The lives and opinions of eminent philosophères*.

Laurent, G., DeForest, C.E., Beasley, M., Smith, K.B., Wilson, A.J., Smith, T., Nolan, R., Erickson, N., Lamb, D., Hanson, M., Veach, T., Osterman, S., Rickerson, R., Peterson, T., Shoffner, M., Niclas, E., Fernandez, A., Hughes, M., Seaton, D.B., Wells, W., Henry, A.M., Uhl, D., Colaninno, R.C., McMullin, D., Ragan, T., Graham, R.: 2025, The Wide Field Imager (WFI) for the Polarimeter to UNify the Corona and Heliosphere (PUNCH) mission. *Solar Physics* **in work**.

Leamon, R.J., Smith, C.W., Ness, N.F., Matthaeus, W.H., Wong, H.K.: 1998, Observational constraints on the dynamics of the interplanetary magnetic field dissipation range. *J. Geophys. Res.* **103**(A3), 4775. [DOI](#). [ADS](#).

Lepping, R.P., Jones, J.A., Burlaga, L.F.: 1990, Magnetic field structure of interplanetary magnetic clouds at 1 AU. *J. Geophys. Res.* **95**(A8), 11957. [DOI](#). [ADS](#).

Li, J., Jewitt, D.: 2013, Recurrent Perihelion Activity in (3200) Phaethon. *Astron. J.* **145**(6), 154. [DOI](#). [ADS](#).

Liu, J., McIntosh, S.W., De Moortel, I., Threlfall, J., Bethge, C.: 2014, Statistical Evidence for the Existence of Alfvénic Turbulence in Solar Coronal Loops. *Astrophys. J.* **797**(1), 7. [DOI](#). [ADS](#).

Liu, Y.D., Luhmann, J.G., Möstl, C., Martinez-Oliveros, J.C., Bale, S.D., Lin, R.P., Harrison, R.A., Temmer, M., Webb, D.F., Odstrcil, D.: 2012, Interactions between Coronal Mass Ejections Viewed in Coordinated Imaging and in situ Observations. *Astrophys. J. Lett.* **746**(2), L15. [DOI](#). [ADS](#).

Lopez, R.E.: 1987, Solar cycle invariance in solar wind proton temperature relationships. *J. Geophys. Res.* **92**(A10), 11189. [DOI](#). [ADS](#).

Lugaz, N., Farrugia, C.J., Davies, J.A., Möstl, C., Davis, C.J., Rousset, I.I., Temmer, M.: 2012, The Deflection of the Two Interacting Coronal Mass Ejections of 2010 May 23-24 as Revealed by Combined in Situ Measurements and Heliospheric Imaging. *Astrophys. J.* **759**(1), 68. [DOI](#). [ADS](#).

Lyot, B.: 1930, La couronne solaire étudiée en dehors des éclipses. *Bulletin Astronomique* **6**, 305.

MacQueen, R.M., Gosling, J.T., Hildner, E., Munro, R.H., Poland, A.I., Ross, C.L.: 1974, The High Altitude Observatory white light coronagraph. In: Menzel, D.H., Larmore, L., Crawford, D. (eds.) *Instrumentation in Astronomy II, Society of Photo-Optical Instrumentation Engineers (SPIE) Conference Series* **44**, 207. [DOI](#). [ADS](#).

Malanushenko, A., one, two, three: 2025, Cme tracking with punch. *Sol. Phys.* **In work**.

Marsch, E., Tu, C.Y.: 1993, Correlations between the fluctuations of pressure, density, temperature and magnetic field in the solar wind. *Annales Geophysicae* **11**(8), 659. [ADS](#).

Mathewson, D.S., Ford, V.L.: 1970, Polarization Observations of 1800 Stars. *Memoirs of the Royal Astronomical Society* **74**, 139. ADS Bibcode: 1970MmRAS..74..139M. <https://ui.adsabs.harvard.edu/abs/1970MmRAS..74..139M>.

Matthaeus, W.H., Velli, M.: 2011, Who Needs Turbulence?. A Review of Turbulence Effects in the Heliosphere and on the Fundamental Process of Reconnection. *Space Sci. Rev.* **160**(1-4), 145. [DOI](#). [ADS](#).

McComas, D.J., Gosling, J.T., Skoug, R.M.: 2000, Ulysses observations of the irregularly structured mid-latitude solar wind during the approach to solar maximum. *Geophys. Res. Lett.* **27**(16), 2437. [DOI](#). [ADS](#).

McComas, D.J., Elliott, H.A., Gosling, J.T., Reisenfeld, D.B., Skoug, R.M., Goldstein, B.E., Neugebauer, M., Balogh, A.: 2002, Ulysses' second fast-latitude scan: Complexity near solar maximum and the reformation of polar coronal holes. *Geophys. Res. Lett.* **29**(9), 1290. [DOI](#). [ADS](#).

McIlwain, C.E.: 1960, Direct Measurement of Particles Producing Visible Auroras. *J. Geophys. Res.* **65**, 2727. [DOI](#). [ADS](#).

Metcalfe, T.S., Egeland, R., van Saders, J.: 2016, Stellar Evidence That the Solar Dynamo May Be in Transition. *Astrophys. J. Lett.* **826**(1), L2. [DOI](#). [ADS](#).

Mierla, M., Inhester, B., Marqué, C., Rodriguez, L., Gissot, S., Zhukov, A., Berghmans, D., Davila, J.: 2009, On 3d reconstruction of coronal mass ejections: I. method description and application to seccchi-cor data. *Solar Physics* **259**, 123.

Mierla, M., Inhester, B., Antunes, A., Boursier, Y., Byrne, J.P., Colaninno, R., Davila, J., de Koning, C.A., Gallagher, P.T., Gissot, S., Howard, R.A., Howard, T.A., Kramar, M., Lamy, P., Liewer, P.C., Maloney, S., Marqué, C., McAteer, R.T.J., Moran, T., Rodriguez, L., Srivastava, N., Cyr, O.C.S., Stenborg, G., Temmer, M., Thernisien, A., Vourlidas, A., West, M.J., Wood, B.E., Zhukov, A.N.: 2010, On the 3-d reconstruction of coronal mass ejections using coronagraph data. *Annales Geophysicae* **28**(1), 203. [DOI](#). <https://angeo.copernicus.org/articles/28/203/2010/>.

Mierla, M., Inhester, B., Zhukov, A.N., Shestov, S.V., Bemporad, A., Lamy, P., Koutchmy, S.: 2022, Polarimetric Studies of a Fast Coronal Mass Ejection. *Solar Phys.* **297**(7), 78. [DOI](#). [ADS](#).

Minnaert, M.: 1930, On the continuous spectrum of the corona and its polarisation. With 3 figures. (Received July 30, 1930). *Zeitschrift für Astrophysik* **1**, 209. [ADS](#).

Miyoshi, Y., Kataoka, R.: 2005, Ring current ions and radiation belt electrons during geomagnetic storms driven by coronal mass ejections and corotating interaction regions. *Geophys. Res. Lett.* **32**(21), L21105. [DOI](#). [ADS](#).

Mizuno, D.R., Buffington, A., Cooke, M.P., Eyles, C.J., Hick, P.P., Holladay, P.E., Jackson, B.V., Johnston, J.C., Kuchar, T.A., Mozer, J.B., Price, S.D., Radick, R.R., Simnett, G.M., Sinclair, D., Tappin, S.J., Webb, D.F.: 2005, Very high altitude aurora observations with

the Solar Mass Ejection Imager. *Journal of Geophysical Research (Space Physics)* **110**(A7), A07230. [DOI](#). [ADS](#).

Möbius, E., Morris, D., Popecki, M.A., Klecker, B., Kistler, L.M., Galvin, A.B.: 2002, Charge states of energetic (~0.5 MeV/n) ions in corotating interaction regions at 1 AU and implications on source populations. *Geophys. Res. Lett.* **29**(2), 1016. [DOI](#). [ADS](#).

Morgan, H.: 2015, An Atlas of Coronal Electron Density at 5R<sub>⊕</sub>. I. Data Processing and Calibration. *Astrophys. Journ. Supp.* **219**(2), 23. [DOI](#). [ADS](#).

Möstl, C., Farrugia, C.J., Kilpua, E.K.J., Jian, L.K., Liu, Y., Eastwood, J.P., Harrison, R.A., Webb, D.F., Temmer, M., Odstrcil, D., Davies, J.A., Rollett, T., Luhmann, J.G., Nitta, N., Mulligan, T., Jensen, E.A., Forsyth, R., Lavraud, B., de Koning, C.A., Veronig, A.M., Galvin, A.B., Zhang, T.L., Anderson, B.J.: 2012, Multi-point Shock and Flux Rope Analysis of Multiple Interplanetary Coronal Mass Ejections around 2010 August 1 in the Inner Heliosphere. *Astrophys. J.* **758**(1), 10. [DOI](#). [ADS](#).

Müller, D., Cyr, O.S., Zouganis, I., Gilbert, H.R., Marsden, R., Nieves-Chinchilla, T., Antonucci, E., Auchère, F., Berghmans, D., Horbury, T., *et al.*: 2020, The solar orbiter mission-science overview. *Astronomy & Astrophysics* **642**, A1.

Nesvorný, D., Deienno, R., Bottke, W.F., Jedicke, R., Naidu, S., Chesley, S.R., Chodas, P.W., Granvik, M., Vokrouhlický, D., Brož, M., Morbidelli, A., Christensen, E., Shelly, F.C., Bolin, B.T.: 2023, NEOMOD: A New Orbital Distribution Model for Near-Earth Objects. *Astron. J.* **166**(2), 55. [DOI](#). [ADS](#).

Neugebauer, M.: 2012, Evidence for Polar X-Ray Jets as Sources of Microstream Peaks in the Solar Wind. *Astrophys. J.* **750**(1), 50. [DOI](#). [ADS](#).

Neugebauer, M., Snyder, C.W.: 1966, Mariner 2 Observations of the Solar Wind, 1, Average Properties. *J. Geophys. Res.* **71**, 4469. [DOI](#). [ADS](#).

Odstrcil, D., Pizzo, V.J.: 2009, Numerical Heliospheric Simulations as Assisting Tool for Interpretation of Observations by STEREO Heliospheric Imagers. *Solar Phys.* **259**(1-2), 297. [DOI](#). [ADS](#).

Odstrcil, D., Pulkkinen, A., Taktakishvili, A., MacNeice, P.J., Luhmann, J.G.: 2011, Numerical simulation of CMEs and SEPs in the inner heliosphere in August 2010. In: *AGU Fall Meeting Abstracts* **2011**, SH51B. [ADS](#).

Öhman, Y.: 1947, Results from observations of the total solar eclipse of 1945 July 9: I. The polarization of the corona. *Stockholms Observatoriums Annaler* **15**, 2.1. [ADS](#).

Ontiveros, V., Vourlidas, J.A.G.-E.A.: 2009, CME-driven Shocks: Comparison Between Imaging Data and in-situ Observations. In: *Solar Heliospheric and INterplanetary Environment (SHINE 2009)*, 121. [ADS](#).

Palmerio, E., Carcaboso, F., Khoo, L.Y., Salman, T.M., Sánchez-Cano, B., Lynch, B.J., Rivera, Y.J., Pal, S., Nieves-Chinchilla, T., Weiss, A.J., Lario, D., Mieth, J.Z.D., Heyner, D., Stevens, M.L., Romeo, O.M., Zhukov, A.N., Rodriguez, L., Lee, C.O., Cohen, C.M.S., Rodríguez-García, L., Whittlesey, P.L., Dresing, N., Oleynik, P., Jebaraj, I.C., Fischer, D., Schmid, D., Richter, I., Auster, H.-U., Fraschetti, F., Mierla, M.: 2024, On the Mesoscale Structure of Coronal Mass Ejections at Mercury's Orbit: BepiColombo and Parker Solar Probe Observations. *Astrophys. J.* **963**(2), 108. [DOI](#). [ADS](#).

Parker, E.N.: 1958, Dynamics of the Interplanetary Gas and Magnetic Fields. *Astrophys. J.* **128**, 664. [DOI](#). [ADS](#).

Patel, R., Seaton, D.B., DeForest, C.E.: 2025, *Sol. Phys.* **In work**.

Pecora, F., Yang, Y., Gibson, S., Viall, N.M., Chhiber, R., DeForest, C., Matthaeus, W.H.: 2024, Magnetohydrodynamic Turbulence Simulations as a Testing Ground for PUNCH. *Solar Phys.* **299**(10), 137. [DOI](#). [ADS](#).

Pizzo, V.: 1978, A three-dimensional model of corotating streams in the solar wind 1. Theoretical foundations. *J. Geophys. Res.* **83**(A12), 5563. [DOI](#). [ADS](#).

Pizzo, V.J.: 1980, A three-dimensional model of corotating streams in the solar wind 2. Hydrodynamic streams. *J. Geophys. Res.* **85**(A2), 727. [DOI](#). [ADS](#).

Pizzo, V.J.: 1982, A three-dimensional model of corotating streams in the solar wind 3. Magnetohydrodynamic streams. *J. Geophys. Res.* **87**(A6), 4374. [DOI](#). [ADS](#).

Pizzo, V.J., Gosling, J.T.: 1994, 3-D Simulation of high-latitude interaction regions: Comparison with Ulysses results. *Geophys. Res. Lett.* **21**(18), 2063. [DOI](#). [ADS](#).

Pizzo, V.J., Biesecker, D.A., Millward, G.H., Odstrcil, D.: 2011, Heliospheric remote imaging and its relation to CME input to solar wind propagation models. In: *AGU Fall Meeting Abstracts* **2011**, SH24A. [ADS](#).

Plotkin, K.J., George, A.R.: 1972, Propagation of weak shock waves through turbulence. *Journal of Fluid Mechanics* **54**, 449. [DOI](#). [ADS](#).

Poeckert, R., Bastien, P., Landstreet, J.D.: 1979, Intrinsic polarization of Be stars. *The Astronomical Journal* **84**, 812. ADS Bibcode: 1979AJ.....84..812P. [DOI](#). <https://ui.adsabs.harvard.edu/abs/1979AJ.....84..812P>.

Provornikova, E., Merkin, V.G., Vourlidas, A., Malanushenko, A., Gibson, S.E., Winter, E., Arge, C.N.: 2024, MHD Modeling of a Geoeffective Interplanetary Coronal Mass Ejection with the Magnetic Topology Informed by In Situ Observations. *Astrophys. J.* **977**(1), 106. [DOI](#). [ADS](#).

Pulkkinen, T.: 2007, Space Weather: Terrestrial Perspective. *Living Reviews in Solar Physics* **4**(1), 1. [DOI](#). [ADS](#).

Rachmeler, L.A., Gibson, S.E., Dove, J.B., DeVore, C.R., Fan, Y.: 2013, Polarimetric Properties of Flux Ropes and Sheared Arcades in Coronal Prominence Cavities. *Solar Phys.* **288**(2), 617. [DOI](#). [ADS](#).

Ran, H., Liu, Y.D., Chen, C., Mostafavi, P.: 2024, The Alpha-proton Differential Flow in the Alfvénic Young Solar Wind: from Sub-Alfvénic to Super-Alfvénic. *Astrophys. J.* **963**(2), 82. [DOI](#). [ADS](#).

Raouafi, N.E., Stenborg, G., Seaton, D.B., Wang, H., Wang, J., DeForest, C.E., Bale, S.D., Drake, J.F., Uritsky, V.M., Karpen, J.T., DeVore, C.R., Sterling, A.C., Horbury, T.S., Harra, L.K., Bourouaine, S., Kasper, J.C., Kumar, P., Phan, T.D., Velli, M.: 2023, Magnetic Reconnection as the Driver of the Solar Wind. *Astrophys. J.* **945**(1), 28. [DOI](#). [ADS](#).

Rappazzo, A.F., Velli, M., Einaudi, G., Dahlburg, R.B.: 2005, Diamagnetic and Expansion Effects on the Observable Properties of the Slow Solar Wind in a Coronal Streamer. *Astrophys. J.* **633**(1), 474. [DOI](#). [ADS](#).

Raymond, J.C., McCauley, P.I., Cranmer, S.R., Downs, C.: 2014, The Solar Corona as Probed by Comet Lovejoy (C/2011 W3). *Astrophys. J.* **788**(2), 152. [DOI](#). [ADS](#).

Rees, M.H.: 1963, Auroral ionization and excitation by incident energetic electrons. *Planetary and Space Science* **11**(10), 1209. [DOI](#). [ADS](#).

Ribner, H.S.: 1953, Convection of a pattern of Vorticity through a Shock Wave. *NACA Technical Note* **2864**.

Ribner, H.S.: 1986, *Spectra of noise and amplified turbulence emanating from shock-turbulence interaction: Two scenarios*, Unknown. [ADS](#).

Robbrecht, E., Berghmans, D., Van der Linden, R.A.M.: 2009, Automated LASCO CME Catalog for Solar Cycle 23: Are CMEs Scale Invariant? *Astrophys. J.* **691**(2), 1222. [DOI](#). [ADS](#).

Rouillard, A.P., Savani, N.P., Davies, J.A., Lavraud, B., Forsyth, R.J., Morley, S.K., Opitz, A., Sheeley, N.R., Burlaga, L.F., Sauvaud, J.-A., Simunac, K.D.C., Luhmann, J.G., Galvin, A.B., Crothers, S.R., Davis, C.J., Harrison, R.A., Lockwood, M., Eyles, C.J., Bewsher, D., Brown, D.S.: 2009, A Multispacecraft Analysis of a Small-Scale Transient Entrained by Solar Wind Streams. *Solar Phys.* **256**(1-2), 307. [DOI](#). [ADS](#).

Rouillard, A.P., Davies, J.A., Lavraud, B., Forsyth, R.J., Savani, N.P., Bewsher, D., Brown, D.S., Sheeley, N.R., Davis, C.J., Harrison, R.A., Howard, R.A., Vourlidas, A., Lockwood, M., Crothers, S.R., Eyles, C.J.: 2010, Intermittent release of transients in the slow solar wind: 1. Remote sensing observations. *Journal of Geophysical Research (Space Physics)* **115**(A4), A04103. [DOI](#). [ADS](#).

Ruffenach, A., Lavraud, B., Farrugia, C.J., Démoulin, P., Dasso, S., Owens, M.J., Sauvaud, J.-A., Rouillard, A.P., Lynnyk, A., Foullon, C., Savani, N.P., Luhmann, J.G., Galvin, A.B.: 2015, Statistical study of magnetic cloud erosion by magnetic reconnection. *Journal of Geophysical Research (Space Physics)* **120**(1), 43. [DOI](#). [ADS](#).

Schuerman, D.W., Weinberg, J.L.: 1983, Zodiacal light: a probe of the properties and evolution of interplanetary dust. *Highlights of Astronomy* **6**, 421. [ADS](#).

Schwenn, R.: 2006, Space Weather: The Solar Perspective. *Living Reviews in Solar Physics* **3**(1), 2. [DOI](#). [ADS](#).

Seaton, D.B., one, two, three: 2025, Punch data for space weather forecasting. *Sol. Phys. In work*.

Sheeley, J. N. R., Herbst, A.D., Palatchi, C.A., Wang, Y.-M., Howard, R.A., Moses, J.D., Vourlidas, A., Newmark, J.S., Socker, D.G., Plunkett, S.P., Korendyke, C.M., Burlaga, L.F., Davila, J.M., Thompson, W.T., St. Cyr, O.C., Harrison, R.A., Davis, C.J., Eyles, C.J., Halain, J.P., Wang, D., Rich, N.B., Battams, K., Esfandiari, E., Stenborg, G.: 2008, Heliospheric Images of the Solar Wind at Earth. *Astrophys. J.* **675**(1), 853. [DOI](#).

Sheeley, J. N. R., Lee, D.D.-H., Casto, K.P., Wang, Y.-M., Rich, N.B.: 2009, The Structure of Streamer Blobs. *Astrophys. J.* **694**(2), 1471. [DOI](#). [ADS](#).

Sheeley, N.R. Jr., Michels, D.J., Howard, R.A., Koomen, M.J.: 1980, Initial observations with the SOLWIND coronagraph. *Astrophys. J. Lett.* **237**, L99. [DOI](#). [ADS](#).

Sheeley, N.R. Jr., Howard, R.A., Michels, D.J., Koomen, M.J., Schwenn, R., Muehlhaeuser, K.H., Rosenbauer, H.: 1985, Coronal mass ejections and interplanetary shocks. *J. Geophys. Res.* **90**(A1), 163. [DOI](#). [ADS](#).

Sheeley, N.R., Wang, Y.-M., Hawley, S.H., Brueckner, G.E., Dere, K.P., Howard, R.A., Koomen, M.J., Korendyke, C.M., Michels, D.J., Paswaters, S.E., Socker, D.G., St. Cyr, O.C., Wang, D., Lamy, P.L., Llebaria, A., Schwenn, R., Simnett, G.M., Plunkett, S., Biesecker, D.A.: 1997a, Measurements of Flow Speeds in the Corona Between 2 and 30  $R_{\odot}$ . *Astrophys. J.* **484**(1), 472. [DOI](#). [ADS](#).

Sheeley, N.R., Wang, Y.-M., Hawley, S.H., Brueckner, G.E., Dere, K.P., Howard, R.A., Koomen, M.J., Korendyke, C.M., Michels, D.J., Paswaters, S.E., Socker, D.G., St. Cyr, O.C., Wang, D., Lamy, P.L., Llebaria, A., Schwenn, R., Simnett, G.M., Plunkett, S., Biesecker, D.A.: 1997b, Measurements of Flow Speeds in the Corona Between 2 and 30  $R_{\odot}$ . *Astrophys. J.* **484**(1), 472. [DOI](#). [ADS](#).

Sheppard, S.S., Tholen, D.J., Pokorný, P., Micheli, M., Dell'Antonio, I., Fu, S., Trujillo, C.A., Beaton, R., Carlsten, S., Drlica-Wagner, A., Martínez-Vázquez, C., Mau, S., Santana-Ros, T., Santana-Silva, L., Sifón, C., Simha, S., Thirouin, A., Trilling, D., Vivas, A.K., Zenteno, A.: 2022, A Deep and Wide Twilight Survey for Asteroids Interior to Earth and Venus. *Astron. J.* **164**(4), 168. [DOI](#). [ADS](#).

Silverman, S.M.: 1970, Night Airglow Phenomenology. *Space Sci. Rev.* **11**(2-3), 341. [DOI](#). [ADS](#).

Smith, E.J., Wolfe, J.H.: 1976, Observations of interaction regions and corotating shocks between one and five AU: Pioneers 10 and 11. *Geophys. Res. Lett.* **3**(3), 137. [DOI](#). [ADS](#).

Stenborg, G., Gallagher, B., Howard, R.A., Hess, P., Raouafi, N.E.: 2021a, Pristine PSP/WISPR Observations of the Circumsolar Dust Ring near Venus's Orbit. *Astrophys. J.* **910**(2), 157. [DOI](#). [ADS](#).

Stenborg, G., Howard, R.A., Hess, P., Gallagher, B.: 2021b, PSP/WISPR observations of dust density depletion near the Sun. I. Remote observations to 8  $R_{\odot}$  from an observer between 0.13 and 0.35 AU. *Astron. Astrophys.* **650**, A28. [DOI](#). [ADS](#).

Stenborg, G., Paouris, E., Howard, R.A., Vourlidas, A., Hess, P.: 2023, Investigating Coronal Holes and CMEs as Sources of Brightness Depletion Detected in PSP/WISPR Images. *Astrophys. J.* **949**(2), 61. [DOI](#). [ADS](#).

Stenborg, G., Vourlidas, A., Paouris, E., Howard, R.A.: 2024, Novel Insights on the Dust Distribution in the Zodiacal Dust Cloud from PSP/WISPR Observations at Large Elongations. *Astrophys. J.* **972**(1), 24. [DOI](#). [ADS](#).

Suess, S.T., Wang, A.-H., Wu, S.T.: 1996, Volumetric heating in coronal streamers. *J. Geophys. Res.* **101**(A9), 19957. [DOI](#). [ADS](#).

Suess, S.T., Poletto, G., Wang, A.-H., Wu, S.T., Cuseri, I.: 1998, The Geometric Spreading of Coronal Plumes and Coronal Holes. *Solar Phys.* **180**, 231. [DOI](#). [ADS](#).

Suess, S.T., Ko, Y.-K., von Steiger, R., Moore, R.L.: 2009, Quiescent current sheets in the solar wind and origins of slow wind. *Journal of Geophysical Research (Space Physics)* **114**(A4), A04103. [DOI](#). [ADS](#).

Szabo, A., Lepping, R.P.: 1995, Neptune inbound bow shock. *J. Geophys. Res.* **100**(A2), 1723. [DOI](#). [ADS](#).

Talpeanu, D.-C., Chané, E., Poedts, S., D'Huys, E., Mierla, M., Roussev, I., Hosteaux, S.: 2020, Numerical simulations of shear-induced consecutive coronal mass ejections. *Astron. Astrophys.* **637**, A77. [DOI](#). [ADS](#).

Tappin, S.J., Howard, T.A.: 2009, Interplanetary Coronal Mass Ejections Observed in the Heliosphere: 2. Model and Data Comparison. *Space Science Reviews* **147**(1-2), 55. <http://link.springer.com/10.1007/s11214-009-9550-5>.

Tappin, S.J., Simnett, G.M.: 1997, The Acceleration of CMEs in the Outer Corona as Revealed by LASCO. In: Wilson, A. (ed.) *Correlated Phenomena at the Sun, in the Heliosphere and in Geospace, ESA Special Publication* **415**, 117. [ADS](#).

Tappin, S.J., Hewish, A., Gapper, G.R.: 1984, Tracking a high-latitude corotating stream for more than half a solar rotation. *Planetary and Space Sciences* **32**(10), 1273. [DOI](#). [ADS](#).

Tasnim, S., Cairns, I.H.: 2016, An equatorial solar wind model with angular momentum conservation and nonradial magnetic fields and flow velocities at an inner boundary. *Journal of Geophysical Research (Space Physics)* **121**(6), 4966. [DOI](#). [ADS](#).

Temmer, M., Vršnak, B., Rollett, T., Bein, B., de Koning, C.A., Liu, Y., Bosman, E., Davies, J.A., Möstl, C., Žic, T., Veronig, A.M., Bothmer, V., Harrison, R., Nitta, N., Bisi, M.,

Flor, O., Eastwood, J., Odstrcil, D., Forsyth, R.: 2012, Characteristics of Kinematics of a Coronal Mass Ejection during the 2010 August 1 CME-CME Interaction Event. *Astrophys. J.* **749**(1), 57. [DOI](#). [ADS](#).

Tenerani, A., Velli, M., DeForest, C.: 2016, Inward Motions in the Outer Solar Corona between 7 and 12 R<sub>⊕</sub>: Evidence for Waves or Magnetic Reconnection Jets? *Astrophys. J. Lett.* **825**(1), L3. [DOI](#). [ADS](#).

Thernisien, A., Carter, M., Chua, D., Korendyke, C., Socker, D., Babich, T., Baugh, R., Bonafede, J., Boyer, D., Brown, S., Corsi, K., Cremerius, L., Crippa, C., Davis, J., Gardner, L., Clifford, G., Hohl, B., Haggard, R., Koehler, M., Hunt, T., Kuroda, N., Lanagan, A., Lynch, B., Ogando, M., Noya, M., Pellak, K., Podgurski, R., Bordemay-Padilla, Y., Rich, N., Silver, D., Simmons, J., Smith, L., Spitzak, J., Tanner, S., Uhl, A., Verzosa, J., Wiggins, G., Wilson, C., Zurich, D.: 2021, The CCOR-1 Compact Coronagraph: Description and Ground Calibration Results. In: *AGU Fall Meeting Abstracts* **2021**, SH43B. [ADS](#).

Thompson, W.: 2006, Coordinate systems for solar image data. *Astronomy & Astrophysics* **449**(2), 791.

Thomson, J.J.: 1903, *The conduction of electricity through gases*, 1st edn. Cambridge University Press, Cambridge. First edition.

Tomczyk, S., McIntosh, S.W.: 2009, Time-Distance Seismology of the Solar Corona with CoMP. *Astrophys. J.* **697**(2), 1384. [DOI](#). [ADS](#).

Trippé, S.: 2014, *Polarization and Polarimetry: A Review*. arXiv:1401.1911 [astro-ph]. [DOI](#). <http://arxiv.org/abs/1401.1911>.

Turner, D.L., Kilpua, E.K.J., Hietala, H., Claudepierre, S.G., O'Brien, T.P., Fennell, J.F., Blake, J.B., Jaynes, A.N., Kanekal, S., Baker, D.N., Spence, H.E., Ripoll, J.-F., Reeves, G.D.: 2019, The Response of Earth's Electron Radiation Belts to Geomagnetic Storms: Statistics From the Van Allen Probes Era Including Effects From Different Storm Drivers. *Journal of Geophysical Research (Space Physics)* **124**(2), 1013. [DOI](#). [ADS](#).

Uritsky, V.M., DeForest, C.E., Karpen, J.T., DeVore, C.R., Kumar, P., Raouafi, N.E., Wyper, P.F.: 2021, Plumelets: Dynamic Filamentary Structures in Solar Coronal Plumes. *Astrophys. J.* **907**(1), 1. [DOI](#). [ADS](#).

van de Hulst, H.C.: 1950, The electron density of the solar corona. *Bulletin of the Astronomical Institutes of the Netherlands* **11**, 135. [ADS](#).

Vásquez, A.M., van Ballegooijen, A.A., Raymond, J.C.: 2003, The Effect of Proton Temperature Anisotropy on the Solar Minimum Corona and Wind. *Astrophys. J.* **598**(2), 1361. [DOI](#). [ADS](#).

Verdini, A., Velli, M., Buchlin, E.: 2009, Turbulence in the Sub-Alfvénic Solar Wind Driven by Reflection of Low-Frequency Alfvén Waves. *Astrophys. J. Lett.* **700**(1), L39. [DOI](#). [ADS](#).

Versteeg, M.J.F., Magalhães, A.M., Havercorn, M., Angarita, Y., Rodrigues, C.V., Santos-Lima, R., Kawabata, K.S.: 2023, Interstellar Polarization Survey. II. General Interstellar Medium. *The Astronomical Journal* **165**(3), 87. [DOI](#). <https://iopscience.iop.org/article/10.3847/1538-3881/aca8fd>.

Viall, N.M., Borovsky, J.E.: 2020, Nine Outstanding Questions of Solar Wind Physics. *Journal of Geophysical Research (Space Physics)* **125**(7), e26005. [DOI](#). [ADS](#).

Viall, N.M., Vourlidas, A.: 2015, Periodic Density Structures and the Origin of the Slow Solar Wind. *Astrophys. J.* **807**(2), 176. [DOI](#). [ADS](#).

Viall, N.M., DeForest, C.E., Kepko, L.: 2021, Mesoscale Structure in the Solar Wind. *Frontiers in Astronomy and Space Sciences* **8**, 139. [DOI](#). [ADS](#).

Viall, N.M., Kepko, L., Spence, H.E.: 2008, Inherent length-scales of periodic solar wind number density structures. *Journal of Geophysical Research (Space Physics)* **113**(A7), A07101. [DOI](#). [ADS](#).

Viall, N.M., Kepko, L., Spence, H.E.: 2009, Relative occurrence rates and connection of discrete frequency oscillations in the solar wind density and dayside magnetosphere. *Journal of Geophysical Research (Space Physics)* **114**(A1), A01201. [DOI](#). [ADS](#).

Viall, N.M., Spence, H.E., Vourlidas, A., Howard, R.: 2010, Examining Periodic Solar-Wind Density Structures Observed in the SECCHI Heliospheric Imagers. *Solar Phys.* **267**(1), 175. [DOI](#).

von Steiger, R., Schwadron, N.A., Fisk, L.A., Geiss, J., Gloeckler, G., Hefti, S., Wilken, B., Wimmer-Schweingruber, R.F., Zurbuchen, T.H.: 2000, Composition of quasi-stationary solar wind flows from Ulysses/Solar Wind Ion Composition Spectrometer. *J. Geophys. Res.* **105**(A12), 27217. [DOI](#). [ADS](#).

Vourlidas, A., Howard, R.A.: 2006, The Proper Treatment of Coronal Mass Ejection Brightness: A New Methodology and Implications for Observations. *Astrophys. J.* **642**(2), 1216. [DOI](#). [ADS](#).

Vourlidas, A., Lynch, B.J., Howard, R.A., Li, Y.: 2013, How Many CMEs Have Flux Ropes? Deciphering the Signatures of Shocks, Flux Ropes, and Prominences in Coronagraph Observations of CMEs. *Solar Phys.* **284**(1), 179. [DOI](#). [ADS](#).

Vourlidas, A., Howard, R.A., Plunkett, S.P., Korendyke, C.M., Thernisien, A.F.R., Wang, D., Rich, N., Carter, M.T., Chua, D.H., Socker, D.G., Linton, M.G., Morrill, J.S., Lynch, S., Thurn, A., Van Duyne, P., Hagoor, R., Clifford, G., Grey, P.J., Velli, M., Liewer, P.C., Hall, J.R., DeJong, E.M., Mikic, Z., Rochus, P., Mazy, E., Bothmer, V., Rodmann, J.: 2016, The Wide-Field Imager for Solar Probe Plus (WISPR). *Space Sci. Rev.* **204**(1-4), 83. [DOI](#). [ADS](#).

Vourlidas, A., Howard, R.A., Plunkett, S.P., Korendyke, C.M., Thernisien, A.F., Wang, D., Rich, N., Carter, M.T., Chua, D.H., Socker, D.G., *et al.*: 2016, The wide-field imager for solar probe plus (wisp). *Space Science Reviews* **204**, 83.

Wang, J., Matthaeus, W.H., Chhiber, R., Roy, S., Pradada, R.A., Pecora, F., Yang, Y.: 2024, 1/f Noise in the Heliosphere: A Target for PUNCH Science. *Solar Phys.* **299**(12), 169. [DOI](#). [ADS](#).

Wang, Y.-M., Sheeley, N.R., Socker, D.G., Howard, R.A., Rich, N.B.: 2000, The dynamical nature of coronal streamers. *J. Geophys. Res.* **105**(A11), 25133. [DOI](#). [ADS](#).

Wang, Y.-M., Biersteker, J.B., Sheeley, J. N. R., Koutchmy, S., Mouette, J., Druckmüller, M.: 2007, The Solar Eclipse of 2006 and the Origin of Raylike Features in the White-Light Corona. *Astrophys. J.* **660**(1), 882. [DOI](#). [ADS](#).

Weber, E.J., Davis, J., Leverett: 1967, The Angular Momentum of the Solar Wind. *Astrophys. J.* **148**, 217. [DOI](#). [ADS](#).

Wells, D.C., Greisen, E.W., Harten, R.H.: 1981, FITS - a Flexible Image Transport System. *Astron. Astrophys. Suppl.* **44**, 363. [ADS](#).

West, M.J., Seaton, D.B., Wexler, D.B., Raymond, J.C., Del Zanna, G., Rivera, Y.J., Kobelski, A.R., Chen, B., DeForest, C., Golub, L., *et al.*: 2023, Defining the middle corona. *Solar Physics* **298**(6), 78.

Williams, A.O., Edberg, N.J.T., Milan, S.E., Lester, M., Fränz, M., Davies, J.A.: 2011, Tracking corotating interaction regions from the Sun through to the orbit of Mars using ACE, MEX, VEX, and STEREO. *Journal of Geophysical Research (Space Physics)* **116**(A8), A08103. [DOI](#). [ADS](#).

Williams, J.E.F., Howe, M.S.: 1973, On the possibility of turbulent thickening of weak shock waves. *Journal of Fluid Mechanics* **58**(3), 461. [DOI](#). [ADS](#).

Wood, B.E., Howard, R.A., Socker, D.G.: 2010, Reconstructing the Morphology of an Evolving Coronal Mass Ejection. *Astrophys. J.* **715**(2), 1524. [DOI](#). [ADS](#).

Wood, B.E., Howard, R.A., Thernisien, A., Plunkett, S.P., Socker, D.G.: 2009, Reconstructing the 3D Morphology of the 17 May 2008 CME. *Solar Phys.* **259**(1-2), 163. [DOI](#). [ADS](#).

Wood, B.E., Howard, R.A., Thernisien, A., Socker, D.G.: 2010, The Three-Dimensional Morphology of a Corotating Interaction Region in the Inner Heliosphere. *Astrophys. J. Lett.* **708**(2), L89. [DOI](#). [ADS](#).

Wood, B.E., Wu, C.-C., Rouillard, A.P., Howard, R.A., Socker, D.G.: 2012, A Coronal Hole's Effects on Coronal Mass Ejection Shock Morphology in the Inner Heliosphere. *Astrophys. J.* **755**(1), 43. [DOI](#). [ADS](#).

Zank, G.P., Matthaeus, W.H.: 1992, Waves and turbulence in the solar wind. *J. Geophys. Res.* **97**(A11), 17189. [DOI](#). [ADS](#).

Zank, G.P., Zhou, Y., Matthaeus, W.H., Rice, W.K.M.: 2003, The interaction of turbulence with shock waves. In: Velli, M., Bruno, R., Malara, F., Bucci, B. (eds.) *Solar Wind Ten, American Institute of Physics Conference Series* **679**, 417. [DOI](#). [ADS](#).

Zank, G.P., Zhao, L.-L., Adhikari, L., Telloni, D., Kasper, J.C., Stevens, M., Rahmati, A., Bale, S.D.: 2022, Turbulence in the Sub-Alfvénic Solar Wind. *Astrophys. J. Lett.* **926**(2), L16. [DOI](#). [ADS](#).

Zhao, L.-L., Zank, G.P., Telloni, D., Stevens, M., Kasper, J.C., Bale, S.D.: 2022, The Turbulent Properties of the Sub-Alfvénic Solar Wind Measured by the Parker Solar Probe. *Astrophys. J. Lett.* **928**(2), L15. [DOI](#). [ADS](#).

Zhao, X.P., Hoeksema, J.T.: 2010, The Magnetic Field at the Inner Boundary of the Heliosphere Around Solar Minimum. *Solar Phys.* **266**(2), 379. [DOI](#). [ADS](#).

Zirker, J.B.: 1977, Coronal holes and high-speed wind streams. *Reviews of Geophysics* **15**(3), 257.

Zurbuchen, T.H., Fisk, L.A., Gloeckler, G., Schwadron, N.A.: 1998, Element and Isotopic Fractionation in Closed Magnetic Structures. *Space Sci. Rev.* **85**(1-2), 397. [DOI](#). [ADS](#).